ulm university universität
uulm

The Effects of Casimir Interactions in Experiments on Gravitationally-induced Entanglement

Bachelor Thesis

Submitted by:
Jan Bulling
jan.bulling@uni-ulm.de
1109395

Supervised by:
Marit O. E. Steiner, Julen S. Pedernales, Martin B. Plenio

In this work it was shown by calculating the relative dynamical phase build-up, that Casimir interactions between a conducting Faraday shield and macroscopic Schrödinger-cat states can destroy measurable entanglement due to stochastic variations in the initial setup and due to the thermal motion of the shield.

Contents

<div align="center">Contents</div>

<div align="center">4</div>

1 Introduction

Newton (1687)

Keplers law are inverse square of gravitational force

Maskelyne (1774) Gravitational force of a mountain [1, 2]

Cavendish (1798) Gravitational force via torsion pendulum

1.1 Feynman's Gedankenexperiment

2 A first look

Testing the quantum nature of gravity is no easy task and many proposals seek to detect gravitationally induced entanglement between two masses [3–6] as a form of proof. For all these proposals, gravity is assumed to be mediated by a gravitational field - either classical, described by the metric tensor in general relativity or by a quantum entity. During a time evolution, this field (like any other external field) can only perform local operations (LO) on the states of the test masses. This has repeatedly been seen in different experiments like in the observation of the gravitational Aharonov-Bohm effect [7] or in gravitationally induced quantum interference with neutron influenced by earth's gravitational field [8]. If gravity is now assumed to behave classically, it's propagation between masses can be described by a classical communication (CC) channel [9]. These LOCC operations however cannot turn an initially unentangled state into an entangled one [10, 11]. It immediately follows, that if one measures the involved masses to be entangled after a mutual gravitational interaction, gravity necessarily has to be non-LOCC in some way. Whether this directly implies the *quantum nature of gravity* is a hot topic of debate [12]. It is important to note, that the opposite of this statement is not true. Measuring unentangled masses does not directly imply the classicality of the gravitational field. This can be seen by considering operations that are non-LOCC and also produce unentangled states like for example the swap operation $|\psi\rangle_A |\phi\rangle_B \rightarrow |\phi\rangle_A |\psi\rangle_B$. This operations obviously can't induce entanglement to initially unentangled states, but requires the exchange of quantum information between them - which is not possible using classical communication alone. In other words: If one prepares masses initially in a pure product state and measures *any* state which cannot be obtained by LOCC-operations after some final time evolution, it is impossible for gravity to be classical. One can even go so far and define the term ***quantum gravity*** as any interaction mediated by gravity that cannot be described by LOCC operations alone [9].

A plausible and logical idea for an experiment to test for gravitational induced entanglement was suggested by Feynman during a discussion session at the 1957 "Conference on the Role of Gravitation in Physics" at Chapel Hill, North Carolina [13, p. 247-260] and is described in this chapter. It requires the generation of coherent quantum superpositions of the center-of-mass degree of freedom for two massive objects either in so-called Schrödinger-cat states or squeezed gaussian states [6, 14]. Both masses are brought close enough together such as gravity has a notable effect after a set time. Ignoring non-gravitational couplings, the mutual gravitational interaction should entangle the masses - of course only *if gravity behaves quantum*. There exists criticizing arguments,

that entanglement generation does not strictly require a quantum nature of gravity and other classical mechanisms could induce entanglement as well [15]. In the low energy limit $E \lesssim m_p c^2 \sim 10^{19}\,\text{GeV}$ and for close separations, the gravitational interaction can be described by an instantaneous Newtonian $1/r$ potential acting on the center-of-mass positions [14, 16, 17]. Spatial superpositions lead to superpositions of the metric and consequently - in the non-relativistic limit - to a superposed Newtonian potential. The interaction Hamiltonian $\hat{H}_G$ is described by

$$\hat{H}_G = -\frac{Gm^2}{|L - (\hat{x}_A - \hat{x}_B)|}, \tag{2.1}$$

where $G = 6.6743 \times 10^{-11}\,\text{m}^3\text{kg}^{-1}\text{s}^{-2}$ is the gravitational constant. The positions x_A and x_B of the both masses A and B have been canonically quantized and if they are delocalized in cat-states $|\psi\rangle = 1/\sqrt{2}\left(\left|\psi^{(1)}\right\rangle + \left|\psi^{(2)}\right\rangle\right)$, both states are eigenstates of $\hat{x}$. If $L \gg |\hat{x}_A - \hat{x}_B|$, the denominator of $\hat{H}_G$ can be expanded up to second order in $\hat{x}_A - \hat{x}_B$. In this thesis, L will be in the μm and the spatial extension Δx is around $500\,\text{nm}$ [18], which is why this expansion will always be justified. The zeroth order term is just a overall energy offset, the first order term $\propto (\hat{x}_A - \hat{x}_B)$ as well as the terms $\hat{x}_i^2$ result only in a local interaction for each mass separately. The coupling term $-(\hat{x}_A\hat{x}_B + \hat{x}_B\hat{x}_A) = -2\hat{x}_A\hat{x}_B$ however couples both masses and thus can mediate entanglement. An exemplary calculation of this is shown in appendix A.1.

The observable entanglement is however very weak as it depends on the gravitational coupling strength and quantum states of the masses typically need to have coherence times of order of $100\,\text{ms}$ to $10\,\text{s}$, imposing a huge experimental challenge. As will be shown in the next section the entanglement rate between two massive particles increases with the spatial width of the wave functions Δx and their mass M. To contextualize: The most massive object ever put into a spatial superposition in matter-wave interferometry is in the order of $4 \times 10^{-23}\,\text{kg}$ [18] whereas the smallest object whose gravitational field has been measured was just below $100\,\text{mg}$ [19] - a difference of 19 orders of magnitude. Levitated particles pose a promising platform for bridging this gap: As the name suggests, the test masses are levitated and are therefore well decoupled from their environment in ultra high vacuums, where even collisions with single air molecules can be prevented. Furthermore, there are multiple proposals on how to prepare the needed spatial superpositions needed experimentally [3, 6, 20]. One way is us use internal or external non-linearities such as spin degree of freedoms. Diamonds prepared with nitrogen-vacancies can be used in a Stern-Gerlach apparatus where an applied magnetic field gradient creates delocalized states [6]. Alternatively, a 1D harmonic potential [3] or a double-well potential can be used for trapping levitated particles and ground-state cooling can create spatially delocalized states. In this thesis, it is assumed that all required states and superpositions can be prepared experimentally.

One of most prominent proposals to test gravity for quantum features is described in Ref. [6] and is depicted in fig. 2.1. Two massive bodies with masses M_A and M_B are initially separated by a center-to-center distance $2L$. The masses are prepared in a coherent delocalized quantum superposition Schrödinger-cat-like state in, for now, an
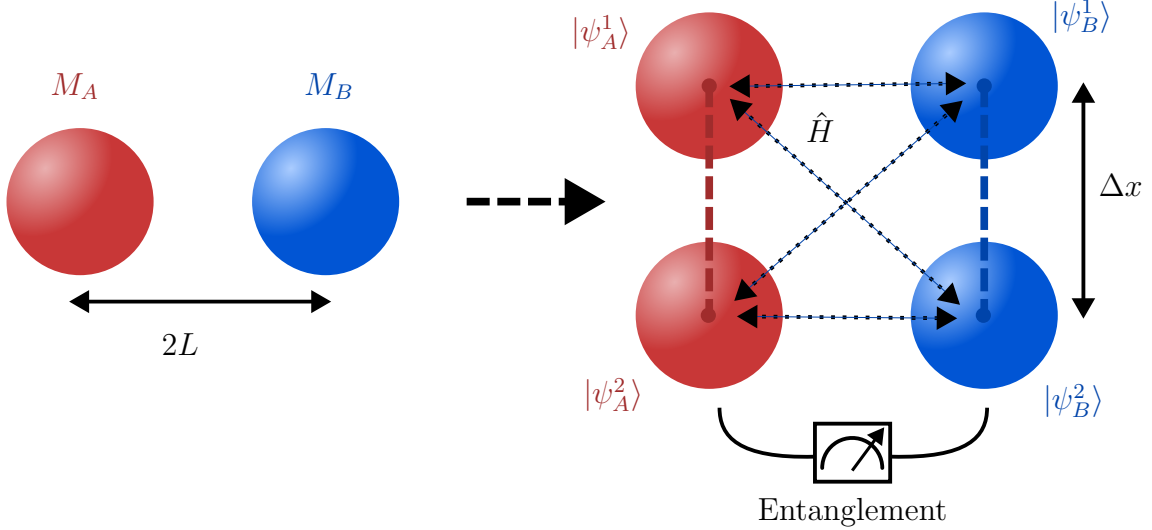
Figure 2.1: Schematic figure of the proposed experiment with two masses prepared in a spatial superposition state. The gravitational interaction $\hat{H}$ induces different phases to each of the superpositions due to the different distances between all masses. This results in measurable entanglement after some time evolution.

orientation, where they are perfectly parallel to each other fig. 2.1. The spatial extension size of the superposition is denoted by Δx. With the notation introduced in fig. 2.1, the initial state at $t = 0$ is given by

$$|\psi(t = 0)\rangle = \frac{1}{2} \left(\left| \psi_A^1 \right\rangle + \left| \psi_A^2 \right\rangle \right) \otimes \left(\left| \psi_B^1 \right\rangle + \left| \psi_B^2 \right\rangle \right). \tag{2.2}$$

The state evolves under a Hamiltonian $\hat{H}_G$ and after some time the position of each mass is measured and checked for entanglement. For now it is assume that all other interactions except gravity are negligible. In reality, electromagnetic forces and Casimir-Polder interactions [21, 22] need to be considered. In the time scales of the experiment, the acceleration of the masses due to the mutual gravitational attraction can be neglected [1]. Therefore, the gravitational potential can be assumed to be static and $|L - (\hat{x}_A - \hat{x}_B)|$ can be replaced by the distance operator $\hat{L}$

$$\hat{V} = -\frac{GM_A M_B}{\left| \hat{L} \right|}. \tag{2.3}$$

$\hat{L}$ represents the separation between two states $\left| \psi_A^{(i)} \right\rangle$ and $\left| \psi_B^{(j)} \right\rangle$ $(i = 1, 2)$ and acts on the state $\left| \psi_A^{(i)} \right\rangle \otimes \left| \psi_B^{(i)} \right\rangle$ like $\hat{L} \left| \psi_A^{(i)} \psi_B^{(i)} \right\rangle = 2L^{(ij)} \left| \psi_A^{(i)} \psi_B^{(i)} \right\rangle$ with $2L^{(ij)}$ being the distance

---

[1]Take for example a silica sphere ($\rho = 2648 \, \text{kg/m}^3$) with $R = 10^{-5} \, \text{m}$ separated by $2L = 4R$. The mutual gravitational acceleration for each sphere is around $a = GM/(2L)^2 = 5 \times 10^{-13} \, \text{m/s}^2$ which results for $t \sim 1 \, \text{s}$ in a displacement of $\sim 10^{-13} \, \text{m}$ which is much smaller than typical variances of the ground state $\Delta x \sim 100 \, \text{nm}$ [18].

between the associated cat-states. During time evolution, the different parts of the superpositions built up different local phases according to their separation distance. In the following section, the time evolution of a state as in eq. (2.2) under this Newtonian potential will be analyzed.

2.1 Time evolution under a gravitational potential

The time evolution of a quantum system is governed by the Schrödinger-equation

$$i\hbar \frac{\partial}{\partial t} |\psi(t)\rangle = \hat{H} |\psi(t)\rangle \tag{2.4}$$

where in this case the interaction Hamiltonian responsible for the entanglement dynamics is given by $\hat{H} = \hat{V}$ eq. (2.3). The eigenbasis of $\hat{V}$ is given by $\left\{ \left| \psi_A^{(1)} \right\rangle, \left| \psi_A^{(2)} \right\rangle \right\} \otimes \left\{ \left| \psi_B^{(1)} \right\rangle, \left| \psi_B^{(2)} \right\rangle \right\}$, as all these states are eigenstates of the distance operator $\hat{L}$

$$\hat{V} \left| \psi_A^{(i)} \right\rangle \otimes \left| \psi_B^{(j)} \right\rangle = -\frac{GM_A M_B}{2L^{(ij)}} \left| \psi_A^{(i)} \right\rangle \otimes \left| \psi_B^{(j)} \right\rangle. \tag{2.5}$$

The Schrödinger equation for the diagonal Hamiltonian $\hat{H}$ can be directly solved for the initial state eq. (2.2) with the solution given by

$$|\psi(t)\rangle = \frac{1}{2} \sum_{i,j \in \{1,2\}} \exp\left\{ \frac{i}{\hbar} \frac{GM_A M_B}{2L^{(ij)}} t \right\} \left| \psi_A^{(i)} \psi_B^{(j)} \right\rangle \tag{2.6}$$

where the tensor product $\otimes$ was omitted. It is possible to express the state using the dynamically accumulated phases $\phi^{(ij)}$ which build-up after a mutual interaction as

$$|\psi(t)\rangle = \frac{1}{2} \left(e^{i\phi^{(11)}} \left| \psi_A^{(1)} \psi_B^{(1)} \right\rangle + e^{i\phi^{(12)}} \left| \psi_A^{(1)} \psi_B^{(2)} \right\rangle + e^{i\phi^{(21)}} \left| \psi_A^{(2)} \psi_B^{(1)} \right\rangle + e^{i\phi^{(22)}} \left| \psi_A^{(2)} \psi_B^{(2)} \right\rangle \right), \tag{2.7}$$

The phases $\phi^{(ij)}$ in the specific setup shown in fig. 2.1 are given by

$$\phi \equiv \phi^{(11)} = \phi^{(22)} = \frac{GM_A M_B}{2\hbar L} t \qquad \text{and} \qquad \phi^{(12)} = \phi^{(21)} = \frac{GM_A M_B}{\hbar \sqrt{4L^2 + (\Delta x)^2}} t. \tag{2.8}$$

By expanding the phases for small superposition sizes $\Delta x \ll L$, the global phase ϕ can be factored out of the evolved state

$$\phi^{(12)} = \phi^{(21)} \approx \frac{GM_A M_B}{\hbar} \left[\frac{1}{2L} - \frac{(\Delta x)^2}{16L^3} \right] t \equiv \phi - \Delta\phi. \tag{2.9}$$

which ultimately can be written in the form

$$|\psi(t)\rangle = e^{i\phi} \frac{1}{\sqrt{2}} \left[\left| \psi_A^{(1)} \right\rangle \otimes \frac{\left| \psi_B^{(1)} \right\rangle + e^{-i\Delta\phi} \left| \psi_B^{(2)} \right\rangle}{\sqrt{2}} + \left| \psi_A^{(2)} \right\rangle \otimes \frac{e^{-i\Delta\phi} \left| \psi_B^{(1)} \right\rangle + \left| \psi_B^{(2)} \right\rangle}{\sqrt{2}} \right]. \tag{2.10}$$

One can see immediately that in general, the resulting state cannot be written as a product state, hence it is entangled. This is of course only the case, if $\Delta\phi \neq k\pi$ with integer $k \in \mathbb{N}$.

In order In order to assess quantitatively how entangled the state $|\psi(t)\rangle$ after time t is, a more sophisticated measure is required. One possible measure is the "logarithmic negativity", which is used in the rest of this work.

2.2 Entanglement measures

Checking whether an arbitrary state ρ is entangled or not is no easy task. In fact, this problem is known to be NP-hard [23]. A state $\rho_{AB} \in \mathcal{H}_A \otimes \mathcal{H}_B$ is called entangled, if it is ***non-separable***, that is, it cannot be expressed as a tensor product of two subsystems $\rho_A \in \mathcal{H}_A$ and $\rho_B \in \mathcal{H}_B$. Only for specific cases - like the case of two qubits or qubit-qutrit - a simple sufficient criterion for determining the separability of a general mixed state is known: The positive partial transpose (PPT) criterion states, that if the partial transpose of the density matrix is positive ($\rho^{\Gamma_A} > 0$ [2]), the state ρ is separable [10, 11]. In other words, if ρ^{Γ_A} has negative eigenvalues, ρ is guaranteed to describe an entangled state. The inverse is true, if and only if the dimension of $\rho_A \otimes \rho_B$ is 2×2 or 3×2 [10] - otherwise, only having non-negative eigenvalues doesn't necessarily result in an unentangled system. The partial transpose with respect to a subsystem i can be understood in the same way as the partial trace, where the operation (in this case the transform) is performed only on indices corresponding the subsystem ρ_i. It is defined for an arbitrary density operator $\rho = \sum_{ijkl} p_{kl}^{ij} |i\rangle\langle j| \otimes |k\rangle\langle l|$ as $\rho^{\Gamma_A} = \sum_{ijkl} p_{kl}^{ji} |i\rangle\langle j| \otimes |k\rangle\langle l|$. To see the necessity of the PPT criterion, consider a separable mixed state ρ, which can be generally expressed as

$$\rho = \sum p_i \rho_A^i \otimes \rho_B^i. \tag{2.11}$$

The partial transpose is in this case trivial:

$$\rho^{\Gamma_A} = \sum p_i (\rho_A^i)^T \otimes \rho_B^i. \tag{2.12}$$

Since the transpose preserves eigenvalues, the transposed subsystem A is still positive $(\rho_A^i)^T > 0$ and describes again a valid quantum state. It follows, that ρ^{Γ_A} is positive as well. If somehow ρ^{Γ_A} has any negative eigenvalues, this can only mean that the initial state ρ is not separable and cannot be expressed in the form of eq. (2.11) and the necessity of the criterion is shown.

For quantifying entanglement in a more precise way, a mathematical quantity called ***entanglement measure*** can be used. A good measure should be able to capture the essential features of entanglement. One can axiomatically state what properties such a measure $E(\rho)$ should have [10, 11]:

---

[2]A matrix is defined as positive ("positive definite"), if all eigenvalues are positive.

Normalization An entanglement measure should be a map from a state to a positive real number:

$$\rho \rightarrow E(\rho) \in \mathbb{R}^+ \tag{2.13}$$

where usually the maximally entangled state has $E = 1$.

Monotonicity under LOCC E should not increase under local operations and classical communications. This is the most important postulate for an entanglement measure and often cited as the *only* required postulate.

Vanishing on separable states $E(\rho) = 0$ if ρ is separable

Often one finds additional properties useful like *convexity* $E(\sum p_i \rho_i) \leq \sum p_i E(\rho_i)$ or (full) *additivity* $E(\rho \otimes \sigma) = E(\rho) + E(\sigma)$.

A function that satisfies these conditions is often called an *entanglement monotone.*

The **negativity** $\mathcal{N}$ is such an entanglement monotone [11, 24] that used the PPT criterion to determine if a state is entangled or not. It is defined as

$$\mathcal{N} = \frac{\left\|\rho^{\Gamma_A}\right\|_1 - 1}{2} \tag{2.14}$$

where $\|A\|_1 = \operatorname{tr}|A| = \operatorname{tr}\sqrt{A^\dagger A}$ is the trace norm. The negativity however is not additive and a more universally applicable and widely used entanglement measure is the **logarithmic negativity** [25]

$$E_N(\rho) = \log_2 \left\|\rho^{\Gamma_A}\right\|_1. \tag{2.15}$$

The monotonicity of the logarithm implies, that E_N is an entanglement monotone as well. Furthermore it is noteworthy, that $\left\|\rho^{\Gamma_A}\right\| = \left\|\rho^{\Gamma_B}\right\|$ as will be shown below. Therefore, the logarithmic negativity is symmetric under exchange of to the subsystem.

Proposition 2.1. *a) The partial transpose w.r.t. subsystem A is equal to the transposed partial transpose w.r.t. subsystem B: $\rho^{\Gamma_A} = (\rho^{\Gamma_B})^T$. b) The trace norms of partially transposed density operators w.r.t. any subsystem are equal: $\left\|\rho^{\Gamma_A}\right\|_1 = \left\|\rho^{\Gamma_B}\right\|_1$.*

Proof. a) A general density matrix ρ can be expressed as

$$\rho = \sum_{i,j,k,l} \rho_{ij,kl} \left|i\rangle\langle j\right|_A \otimes \left|k\rangle\langle l\right|_B$$

The partial transpose with respect to subsystem B is then defined as

$$\rho^{\Gamma_B} \equiv \sum_{i,j,k,l} \rho_{ij,kl} \left|i\rangle\langle j\right|_A \otimes \left(\left|k\rangle\langle l\right|_B\right)^T = \sum_{i,j,k,l} c_{ij,kl} \left|i\rangle\langle j\right|_A \otimes \left|l\rangle\langle k\right|_B$$

The complete transpose of this is

$$(\rho^{\Gamma_B})^T = \sum_{i,j,k,l} \rho_{ij,kl} \left(\left|i\rangle\langle j\right|_A\right)^T \otimes \left(\left|l\rangle\langle k\right|_B\right)^T = \sum_{i,j,k,l} c_{ij,kl} \left|j\rangle\langle i\right|_A \otimes \left|k\rangle\langle l\right|_B \equiv \rho^{\Gamma_A}$$

b) Clear by a) and by using lemma 2.1 and the fact that the eigenvalues of a square matrix A and A^T are equal. □

The logarithmic negativity is very easy to calculate compared to other entanglement measures. If the eigenvalues of ρ are known, the logarithmic negativity can be directly computed, as will be demonstrated below. Since this thesis focuses on low-dimensional 4×4 systems, single eigenvalues can be determined with low effort analytically as well as numerically with great stability.

Lemma 2.1. *The trace norm $\|A\|_1 \equiv \operatorname{tr} \sqrt{A^\dagger A}$ of a hermitian matrix A is equal to the sum of the absolute eigenvalues of A.*

Proof. This can be immediately seen by the spectral decomposition $\lambda(A) = \{\lambda_1, ...\}$:

$$\operatorname{tr} \sqrt{A^\dagger A} = \operatorname{tr} \sqrt{A^2} = \operatorname{tr}\left\{ U \sqrt{\operatorname{diag}(\lambda_1, \dots)^2} U^\dagger \right\} = \sum_i \sqrt{\lambda_i^2} = \sum_i |\lambda_i| \, .$$

□

Proposition 2.2. *The negativity eq.* (2.14) *is given as the absolute sum of all negative eigenvalues of ρ^Γ:*

$$\mathscr{N}(\rho) \equiv \frac{\|\rho^\Gamma\|_1 - 1}{2} = \left| \sum_{\lambda_i < 0} \lambda_i \right| . \tag{2.16}$$

Proof. The proof is in parts given by Vidal and Werner [24]. It is known that the density matrix is hermitian: $\rho = \rho^\dagger$. Using lemma 2.1, the trace norm of the density matrix is is given as $\|\rho\|_1 = \sum \lambda_i = \operatorname{tr} \rho = 1$. The partial transpose ρ^Γ obviously also satisfies $\operatorname{tr} \rho^\Gamma = 1$ but might have negative eigenvalues. Since ρ^Γ is still hermitian, the trace norm is given by

$$\left\|\rho^\Gamma\right\|_1 = \sum_i |\lambda_i| = \sum_{\lambda_i \geq 0} \lambda_i + \sum_{\lambda_i < 0} |\lambda_i| = \sum_i \lambda_i + 2 \sum_{\lambda_i < 0} |\lambda_i| = 1 + 2 \sum_{\lambda_i < 0} |\lambda_i| \, ,$$

where in the last step $\sum \lambda_i = \operatorname{tr} \rho^\Gamma = 1$ was used. □

Remark. The PPT criterion states, that if ρ^Γ has negative eigenvalues, the state ρ is entangled. The negativity uses this criterion for a quantification of entanglement. This motivates the name *negativity*.

Calculating the logarithmic negativity of the evolved state eq. (2.7), it is possible to quantify how the entanglement behaves in time. A straight forward computation following the calculation methods established above yields (for detailed calculations see appendix A.2)

$$E_N(|\psi(t)\rangle\langle\psi(t)|) = \log_2 \left(1 + |\sin \Delta\phi|\right) . \tag{2.17}$$

As expected, the states are not entangled for $\Delta\phi = k\pi\ k \in \mathbb{Z}$ and maximum entanglement $E_N = 1$ is reached for $\Delta\phi = 2\pi k \pm \pi/2$. This result aligns with the previous observations by demanding that the evolved state eq. (2.10) is separable. The complete entanglement dynamics are shown in fig. 2.2. Additionally, this figure depicts the en-
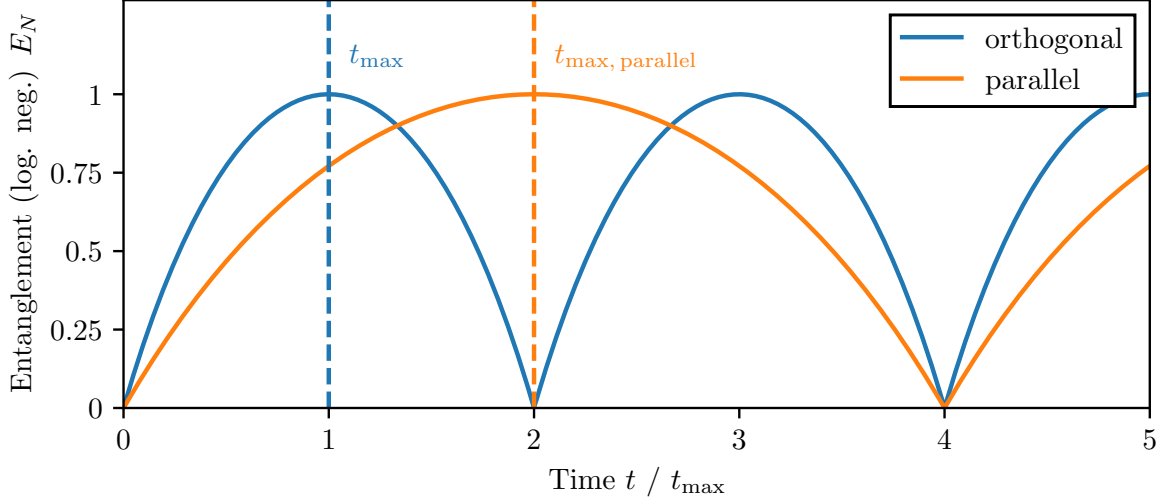

Figure 2.2: Entanglement dynamics quantified by the logarithmic negativity E_N for two different orientations of the spatial superpositions. The parallel orientation (**orange**) is shown in fig. 2.1 and the orthogonal orientation (**blue**) was taken from Ref. [14], where the cat-states are right-angled compared to the parallel configuration. The maximal amount of entanglement is reached after a time given by eq. (2.18) and for reasonable parameters this equates to $t_{\max,\,\mathrm{orthogonal}} \equiv t_{\max} \approx 129\,\mathrm{ms}$.

tanglement generation in the "orthogonal orientation", where both superpositions are aligned in a straight line right-angled to the previously used setup in fig. 2.1.

The time $t_{\max,\,\mathrm{parallel}}$ at which the states are maximally entangled for the first time, can be calculated by using the definition of $\Delta\phi$ from eq. (2.9) as

$$t_{\max,\,\mathrm{parallel}} = \frac{8\pi L^3 \hbar}{G M_A M_B (\Delta x)^2}. \tag{2.18}$$

In the orthogonal orientation, this point in time is reached twice as fast [14]. This is because in this orientation, the difference in distances between the cat-states is maximized and consequently the relative dynamical phase build-up is faster compared to the parallel orientation resulting in a faster entanglement rate.

This suggests, that the orthogonal orientation might be beneficial as it requires shorter coherence times. This effect is studied in more detail in section 4.2. To give an estimation of the coherence times needed, consider two identical silica nano-sphere with density $\rho = 2648\,\mathrm{kg/m^3}$ and radius $R = 10^{-5}\,\mathrm{m} = 10\,\mu\mathrm{m}$ separated by a distance $2L = 4R$.

The superposition size is in the order of $100\,\mathrm{nm}$. The maximum entanglement in the parallel configuration is reached after a time $t_{\mathrm{max,\,parallel}} \approx 258\,\mathrm{ms}$ which is a quite long and challenging experimentally considering that usual in the order of nano-seconds [26].

2.3 Issues with the idealized experimental procedure

For the practical realization of an experiment on measuring gravitationally induced entanglement of masses, other forms of direct or indirect interaction between the particles must be suppressed such that the measured entanglement ultimately arises only due to their gravitational interaction. In particular, the short-range *Casimir interactions* [21] discussed in chapter 3 have to be shielded as they exert a much grater attraction force on the particles at small separations than gravity. It is still a hot topic of discussions whether Casimir interactions can even entangle macroscopic bodies at all, as it is not even clear if it is a conservative force in the first place - although most researchers believe it is [27, 28]. To estimate the minimal particle-particle separation $2L$ requiring that the gravitational interaction V_{Gravity} is stronger than the Casimir interactions V_{Casimir} by a factor $\chi > 1$, the following inequality can be stated:

$$\chi \left| V_{\mathrm{Casimir}} \right| \leq \left| V_{\mathrm{Gravity}} \right| \tag{2.19}$$

$$\Longleftrightarrow \quad \chi \frac{23\hbar c}{4\pi (2L)^7} \left(\frac{\varepsilon_r - 1}{\varepsilon_r + 2} \right)^2 R^6 \leq \frac{GM^2}{2L}. \tag{2.20}$$

Using $M = 4/3\pi R^3 \rho_{\mathrm{Silica}}$, the minimum separation distance is independent of the size of the particle and is given by

$$L \geq \left(\frac{207}{4096} \frac{\hbar c}{\pi^3 G \rho_{\mathrm{Silica}}^2} \right)^{1/6} \sqrt[6]{\chi} \approx 69\,\mu\mathrm{m} \sqrt[6]{\chi}. \tag{2.21}$$

For the same particle as used before, the time for a single measurement, i.e. the coherence time $t_{\mathrm{max}} \approx 30\,\mathrm{s}\sqrt{\chi}$ is very large. The field of levitated particles is promising for these experiments as it offers an isolated, noise-reduced environment while still allowing for exceptional force sensitivity as well as precise quantum control and thus long coherence times [29, 30]. Nevertheless, it would be beneficial to reduce the separation distance between the particles for shorter measurement time. For this, usually a conducting *Faraday shield* between the particles is proposed [31]. Such a shield would simultaneously suppress all other forms of electromagnetic interactions such as Coulomb forced, if the particles are happened to be charged. Coulomb forces have the ability to entangle the particles as well[3] and due to the similar distance behavior for Coulomb and gravitational interactions as well as the stronger coupling, these interactions could potentially be problematic.

---

[3]In fact, the Aspelmeyer group is currently working on an experiment trying to measure entanglement due to Coulomb interactions [32].

This thesis is focused around the problems which arise in the generation of entanglement in the presence of the Faraday shield. Reconstructing the position states of the masses requires many experimental runs and small variations in the initial setup between measurements introduce effective decoherence. Casimir interactions between the particles and the newly placed Faraday shield can degrade entanglement in the final averaged measurement. In chapter 4 this effect is analyzed in depth, narrowing the range of viable parameters for particle-shield separation, superposition size, and particle mass. Additionally, thermal vibrations and shield-induced noise are explored in chapter 5.

3 Casimir effect

Casimir forces can be viewed in a very similar way to the *van der Waals forces*. In fact, both phenomena describe just two different sides of the same coin. They define the so-called dispersion forces between neutral atoms or bodies. The quantum theory of van der Waals forces between two neutral atoms was developed by London in 1930 who found the attractive potential $\propto 1/r^6$ for small separations [33]. Casimir and Polder showed in 1948, that for separations larger than the resonance wavelength of the atoms, retardation effects need to be taken into account and the potential decays by a power law of $1/r^7$ [22]. Additionally, they calculated the interaction with an atom or molecule and a perfectly conducting plate, showing that macroscopic objects could experience these ***Casimir-Polder interactions*** as well. It becomes evident, that a full description of dispersion forces cannot be given by classical electrodynamics alone. Additional considerations regarding relativistic effects and quantum electrodynamics have to be made [34–36]. Casimir, following a suggestion by Bohr [37], found a derivation using the zero-point energy of the vacuum to calculate the attraction between two conducting plates, which works as follows: In quantum electrodynamics the electromagnetic field is described by quantized harmonic oscillators with ground state energy $E_0 = \hbar\omega/2$, where each harmonic oscillator is called a mode. The total *zero-point energy* of the ground state (the vacuum) of the field is therefore given by summing over the energies E_0 for each possible mode n

$$E_{\text{vacuum}} = \frac{\hbar}{2} \sum_n \omega_n. \tag{3.1}$$

These sums are clearly divergent since there exist infinitely many possible modes. While in free space, there are uncountably infinite modes, electrostatic boundary conditions require the field to be zero at the surface of conductors restricting the possible modes between two parallel plates to countably infinite many. Since the difference between two infinite quantities is not well defined, the divergences is often simply dropped, motivated by the fact that energy is usually only defined up to a constant [34]. Precisely the finite difference between the infinite vacuum energy with and without the plates plates give rise to the macroscopic ***Casimir forces***. Using renormalization techniques, Casimir arrived at his famous formula [21]

$$E_{\text{Casimir}} = -\frac{\hbar c \pi^2}{720 L^3} A \tag{3.2}$$

for the attractive Casimir-potential between two conducting plates with surface area A and separation L. The attractive force $F = -\nabla E = -\mathrm{d}E_{\text{Casimir}}/\mathrm{d}L$ between the plates

can be simply expressed as

$$F_{\text{Casimir}} = -\frac{\hbar c \pi^2}{240 L^4} A, \tag{3.3}$$

where $c = 2.9979 \times 10^8$ m/s is the speed of light. It is remarkable, that such a simple relation arises out of the infinities of the vacuum. To this day, these Casimir forces are a major topic of modern scientific research. They are generally very difficult to calculate for geometries other than two plates or for physical materials with dielectric properties. For simple geometries, even the sign of the force is not always intuitively clear [35]: As an example, the Casimir force for an ideal conducting spherical shell leads to an expansion of the sphere [38]. Between other rather simple and important geometries like a sphere-plane or sphere-sphere configuration, no closed and universally applicable expression for the Casimir force exists. In the following section, the different possible approximation methods for large and small separations will be discussed.

Almost ten years after the discovery of Casimir and Polder, Lifshitz was the first to find an expression for the Casimir force between two dielectric plates with arbitrary relative permittivity $\varepsilon_{r,1}$ and $\varepsilon_{r,2}$ for separations larger than the resonant wavelength [4] [40]. The expression he found facilitates the general complexity of the Casimir interactions and can only be expressed in form of an integral [40]

$$F/A = -\frac{\hbar c}{32 \pi^2 L^4} \int_0^\infty \mathrm{d}x \int_1^\infty \mathrm{d}p \, \frac{x^3}{p^2} \left\{ \left[\frac{(s_1 + p)(s_2 + p)}{(s_1 - p)(s_2 - p)} e^x - 1 \right]^{-1} + \right.$$

$$\left. \left[\frac{(s_1 + \varepsilon_{r,1} p)(s_2 + \varepsilon_{r,2} p)}{(s_1 - \varepsilon_{r,1} p)(s_2 - \varepsilon_{r,2} p)} e^x - 1 \right]^{-1} \right\} \tag{3.4}$$

with

$$s_{1(2)} = \sqrt{\varepsilon_{r,1(2)} - 1 + p^2}.$$

In the limit of two perfectly conducting plates ($\varepsilon_{r,1} = \varepsilon_{r,2} \to \infty$), the integral can be solved analytically resulting in the same expression already obtained by Casimir

$$F_{\text{cond.}}/A = -\frac{\hbar c}{16 \pi^2 L^4} \int_0^\infty \mathrm{d}x \int_1^\infty \mathrm{d}p \, \frac{x^3}{p^2 (e^x - 1)} = -\frac{\hbar c \pi^2}{240 L^4}. \tag{3.5}$$

From eq. (3.4) one can also derive the attraction force between two dielectric plates with the same dielectric constant ε_r (DD) as well as the force between a conducting metal

---

[4]The "resonance wavelength" for a macroscopic body is the typical wavelength that induces electric excitations in the body. For example, it might be understood as the plasma frequency in the Drude model [39]. Different models for light-matter interaction result in slightly different resonant wavelength. The Lifshitz formula however holds true for the cases of separations in the micro-meter regime for all practical materials [31].

plate and a dielectric plate (DM). The forces are given by

$$F_{\text{DM}} = -\frac{\hbar c \pi^2}{240 L^4} \frac{\varepsilon_r - 1}{\varepsilon_r + 1} \varphi(\varepsilon_r) \tag{3.6}$$

$$F_{\text{DD}} = -\frac{\hbar c \pi^2}{240 L^4} \left(\frac{\varepsilon_r - 1}{\varepsilon_r + 1}\right)^2 \varphi(\varepsilon_r) \tag{3.7}$$

where $\varphi(\varepsilon_r)$ is a tabulated function [40]. For superconducting plates, $\varphi(\varepsilon_r \to \infty)$ approaches 1 whereas for a perfect dielectric ($\varepsilon_r = 1$) and a metal plate, the function approaches a constant value $\varphi \approx 0.46$. $\varphi(\varepsilon_r)$ is shown for the two cases of DD and DM in fig. 3.1. Since both $(\varepsilon_r - 1)/(\varepsilon_r + 1) < 1$ as well as $\varphi(\varepsilon_r) < 1$ are bounded by 1, the
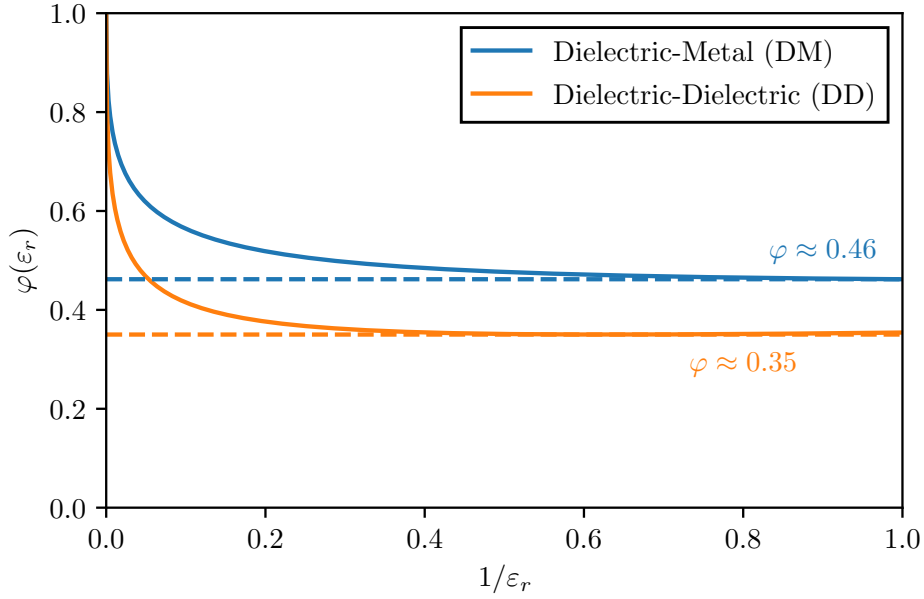

Figure 3.1: Numeric calculations of the function $\varphi(\varepsilon)$ used in the Lifshitz formulas eq. (3.6) and (3.7). The function was calculated for a dielectric and a metal (DM) plate **(blue)** and two dielectric (DD) plates **(orange)**. It approaches unity for $\varepsilon_r \to \infty$ and a finite value for $\varepsilon_r \to 1$.

Casimir force between dielectrics differs from the force between conducting metals by only a constant. The latter therefore form an upper bound for the Casimir interaction.

3.1 Proximity force approximation

While the macroscopic Casimir force has an analytical description for two plates, it is not possible to find such an expression for arbitrary geometries. There even exists no analytic expression for the simple (and for this thesis relevant) plate-sphere geometry for all separations of the bodies. Fortunately, approximation methods exist and in particular

the ***proximity-force-approximation (PFA)*** can, in many cases, be calculated easily as long as the involved surfaces are smooth [41–43]. The PFA is only valid for small separations ($L/R \approx 1$) where R is the typical length scale of the bodes and L die distance between the surfaces. In the sphere-plate geometry, R would be the radius of the sphere and L the center-to-plate distance. In the PFA, the surfaces of the two bodies are divided into infinitesimal small parallel segments with area $\mathrm{d}A$ as depicted in fig. 3.2. Finally, one sums over the forces each of the surface elements experiences to estimate the force on the whole body. This is given by

$$E_{\mathrm{PFA}} = \iint_A \mathrm{d}A \, \frac{E_{\mathrm{plate-plate}}}{A} \tag{3.8}$$

where for the Casimir energy per unit area $E_{\mathrm{plate-plate}}/A$ either eq. (3.2) or alternatively any of the Lifshitz equations eq. (3.7) or eq. (3.6) can be used. For the following
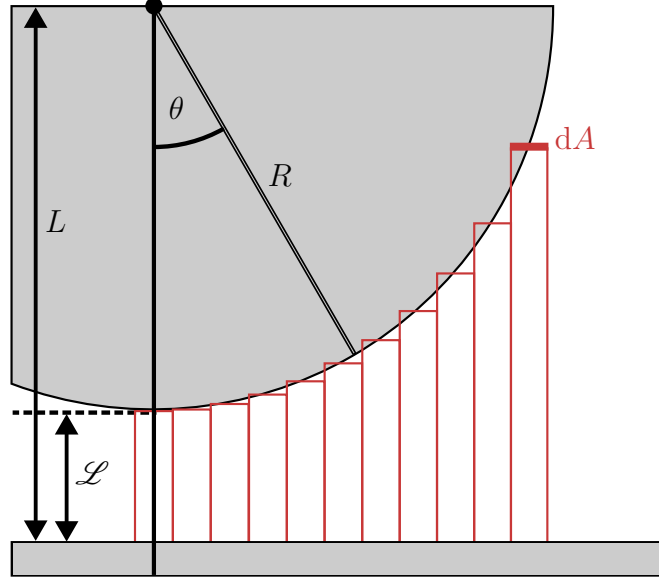

Figure 3.2: In the proximity force approximation the sphere is divided into infinitesimal plane areas $\mathrm{d}A$ which all exert a force $\mathrm{d}F$ according to eq. (3.3). All the contributions are added up together.

calculations, it is important to distinguish the distance between the plate and the spheres center of mass donated by L and the edge-to-edge separation $\mathscr{L} = L - R$.

The problem with this approximation is, that it is ambiguous what surface the area element $\mathrm{d}A$ represents. For the plate-sphere geometry, $\mathrm{d}A$ can be either chosen either tangential to the sphere or parallel to the plate (or in theory any other fictitious surface somewhere in between) [43]. In the limit of the validity of the PFA $\mathscr{L} \ll R$ all methods usually yield the same result. For the following calculations, $\mathrm{d}A$ is chosen parallel to the plate and the area can be parametrized with $r \in [0, R]$ and $\varphi \in [0, 2\pi]$ resulting in

a distance L between the infinitesimal area elements $L(r) = \mathscr{L} + R - \sqrt{R^2 - r^2}$ [5]. The PFA eq. (3.8) yields for a dielectric sphere abd a perfectly conducting plate

$$E_{\mathrm{PFA}} = -\frac{\hbar c \pi^2}{720} \left(\frac{\varepsilon_r - 1}{\varepsilon_r + 1} \right) \varphi(\varepsilon_r) \int_0^R \mathrm{d}r \int_0^{2\pi} r \mathrm{d}\varphi \frac{1}{L(r)^3} \tag{3.9}$$

$$= -\frac{\hbar c \pi^3}{360} \left(\frac{\varepsilon_r - 1}{\varepsilon_r + 1} \right) \varphi(\varepsilon_r) \frac{R^2}{2\mathscr{L}^2(R + \mathscr{L})} \tag{3.10}$$

$$\approx -\frac{\hbar c \pi^3}{720} \left(\frac{\varepsilon_r - 1}{\varepsilon_r + 1} \right) \varphi(\varepsilon_r) \frac{R}{\mathscr{L}^2} \tag{3.11}$$

3.2 Casimir forces between a conducting plate and a dielectric sphere

There does not exist a closed form expression for the Casimir energy between a dielectric sphere with radius R an dielectric constant ε_r in front of a conducting plate, that is applicable at all sphere-plate separations L/R. In the limit of small separations, the proximity force approximation from section 3.1 is valid and yields for dielectric or conducting spheres

$$E_{\mathrm{PFA}} = -\frac{\hbar c \pi^3}{720} \left(\frac{\varepsilon_r - 1}{\varepsilon_r + 1} \right) \varphi(\varepsilon_r) \frac{R}{\mathscr{L}^2} \sim \frac{1}{(L - R)^2} \qquad \text{for } L/R \approx 1 \tag{3.12}$$

$$E_{\mathrm{PFA,\,cond.}} = E_{\mathrm{PFA}}(\varepsilon_r \to \infty) = -\frac{\hbar c \pi^3}{720} \frac{R}{\mathscr{L}^2}. \tag{3.13}$$

For arbitrary separations, the Casimir energy can only be expressed as an infinite series [42, 44] or in terms of an integral [39] The integral form reads

$$F = -\frac{\hbar c}{4\pi L^4} \int_0^\infty \mathrm{d}\omega \, \alpha(\omega) \left[3 \sin 2\omega L - 6L\omega \cos 2\omega L \right.$$
$$\left. - 6L^2\omega^2 \sin 2\omega L + 4L^3\omega^3 \cos 2\omega L \right]. \tag{3.14}$$

where α is the electric polarizability of the sphere and the integration is performed over all possible interaction frequencies ω of the electromagnetic field with the materials.

In the ***large-separation-limit (LSL)***, where the sphere-plate separation are much larger the the resonant wavelength of the material, the polarizability can be taken as a static constant [31, 39]. In this case, the integral eq. (3.14) can be solved analytically by using an exponential convergence factor

$$F = -\frac{6\hbar c}{4\pi L^5} \alpha. \tag{3.15}$$

---

[5]Taking $\mathrm{d}A$ tangential to the sphere, it can be parametrized with $\theta \in [0, \pi/2]$ and $\varphi \in [0, 2\pi]$ resulting in $z(\theta) = \mathscr{L} + R - R\cos\theta$. The PFA eq. (3.8) yields with $\mathrm{d}A = R^2 \sin\theta \mathrm{d}\theta \mathrm{d}\varphi$ the result $\propto \frac{\pi R^2(R+2\mathscr{L})}{\mathscr{L}^2(R+\mathscr{L})^2}$ which in the limit of $\mathscr{L} \ll R$ results in the same expression as eq. (3.11).

The polarizability of a uniform dielectric sphere with a dielectric constant ε_r is calculated in appendix A.3 and is given by

$$\alpha_{\text{sphere}} \propto \left(\frac{\varepsilon_r - 1}{\varepsilon_r + 2} \right) R^3 \tag{3.16}$$

resulting in a Casimir energy of

$$E_{\text{LSL}} = -\frac{3}{8} \frac{\hbar c}{\pi L^4} \left(\frac{\varepsilon_r - 1}{\varepsilon_r + 2} \right) R^3 \sim \frac{1}{L^4} \qquad \text{for } L/R \gg 1 \tag{3.17}$$

$$E_{\text{LSL, cond.}} = E_{\text{LSL}}(\varepsilon_r \to \infty) = -\frac{3}{8} \frac{\hbar c R^3}{\pi L^4}. \tag{3.18}$$

This matches precisely the leading-order term in the series expansion from Ref. [42] and Ref. [45]. A comparison of the PFA and LSL approximations across all separations is shown in fig. 3.3, alongside numerical results from Ref [42].
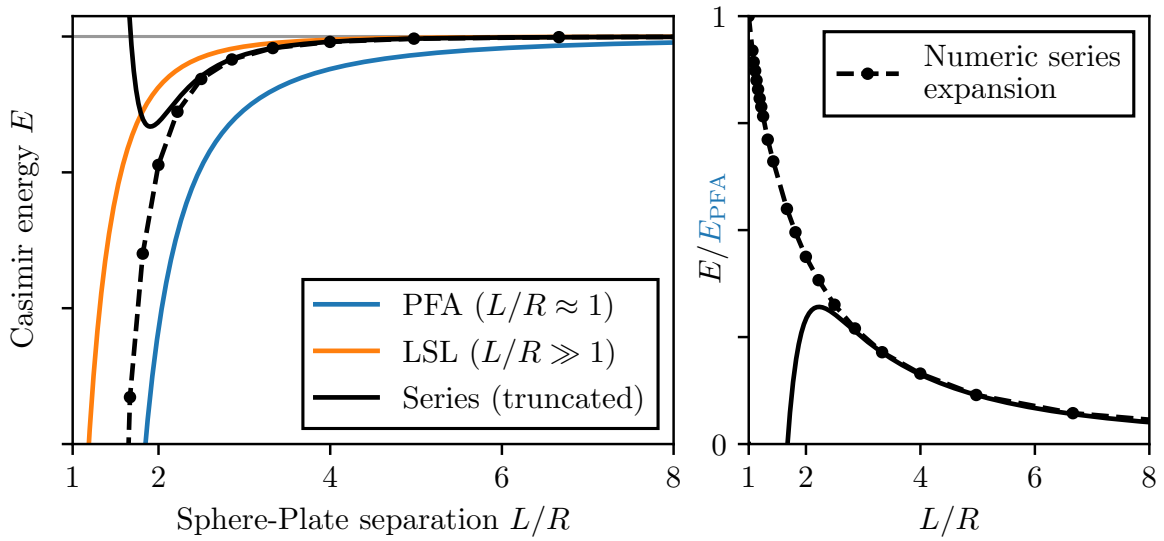

Figure 3.3: Behavior of the Casimir energy for different sphere-plate separations L/R. For close separations ($L/R \approx 1$), the PFA eq. (3.12) is valid whereas for large separations ($L/R \gg 1$) the LSL eq. (3.17) can be used. Additionally the numeric series expansion from Ref. [42] is shown, which converges to the PFA and LSL in each limit.

The scaling of $1/L^4$ for large separations can be motivated empirically. Casimir and Polder calculated the potential between two atoms separated by a distance L with polarizability α_i as [22] [6]

$$E = -\frac{23 \hbar c \alpha_1 \alpha_2}{4 \pi L^7}. \tag{3.19}$$

---

[6] For two macroscopic spheres, the casimir potential looks identical to eq. (3.19). The polarizability α is given by eq. (3.16), resulting in a Casimir potential between two identical dielectric spheres in the large separation limit of $-\frac{23 \hbar c}{4 \pi L^7} \left(\frac{\varepsilon_r - 1}{\varepsilon_r + 2} \right)^2 R^6$ [44].

If both atoms are approximated as spheres with $\alpha \sim R^3$, and one of them is increased to the size of $R \sim L$, the total Casimir-Polder potential between them effectively scales with $\sim R^3/L^4$. This approximation corresponds to the limit $L/R \gg 1$ and aligns with the actual scaling of the macroscopic Casimir potential for large separations in eq. (3.17).

The series expansion in fig. 3.3 suggests, that the proximity-force-approximation is an upper bound for the actual Casimir interaction at all separations. In fact, it can be proven, that the PFA for a superconducting sphere and a plate always predicts a stronger force $|\nabla E|$ than the LSL.

Theorem 3.1. *The Casimir force in the PFA-model eq.* (3.12) *between a superconducting sphere* ($\varepsilon_r \to \infty$) *and a perfectly conducting plate is an upper bound for the LSL eq.* (3.17).

Proof. The proof is given in the following steps: **(a)** first it is shown that $|\nabla E_{\mathrm{PFA}}| > |\nabla E_{\mathrm{LSL}}|$ for arbitrary dielectric spheres, then it will be shown **(b)** that $|\nabla E_{\mathrm{PFA, cond.}}| \geq |\nabla E_{\mathrm{PFA, diel.}}|$.

(a) By directly comparing the gradients of eq. (3.12) (PFA) and eq. (3.12) (LSL), one can find the inequality

$$|\nabla E_{\mathrm{PFA}}| > |\nabla E_{\mathrm{LSL}}|$$

$$\Longleftrightarrow \quad \frac{2\hbar c \pi^3}{720} \left(\frac{\varepsilon_r - 1}{\varepsilon_r + 1}\right) \varphi(\varepsilon_r) \frac{R}{\mathscr{L}^3} > \frac{12\hbar c}{8\pi L^5} \left(\frac{\varepsilon_r - 1}{\varepsilon_r + 2}\right) R^3$$

$$\Longleftrightarrow \quad \frac{\pi^4}{540} \left(\frac{\varepsilon_r + 2}{\varepsilon_r + 1}\right) \varphi(\varepsilon_r) > \frac{(L-R)^3 R^2}{L^5} = \left(\frac{R}{L}\right)^2 - 3\left(\frac{R}{L}\right)^3 + 3\left(\frac{R}{L}\right)^4 - \left(\frac{R}{L}\right)^5$$

One can easily convince oneself that the right-hand side (for $R/L \leq 1$) is upperbounded by ≈ 0.0346 (at $R/L = 0.4$). By remembering that $(\varepsilon_r + 2)/(\varepsilon_r + 1) > 1$ and $\varphi(\varepsilon_r) \gtrsim 0.46$ one can put a lower bound on the left-hand side by $0.0830 > 0.0346$. Therefore, $|\nabla E_{\mathrm{PFA}}| > |\nabla E_{\mathrm{LSL}}|$.

(b) By using eq. (3.12) and eq. (3.13) for the PFA of a dielectric and conducting sphere, it follows quickly that $|\nabla E_{\mathrm{PFA, cond.}}| \geq |\nabla E_{\mathrm{PFA}}(\varepsilon_r)|$, because $\varphi(\varepsilon_r)$ as well as $(\varepsilon_r - 1)/(\varepsilon_r + 1)$ are monotonically increasing with ε_r.

Combining steps **(a)** and **(b)** results in

$$|\nabla E_{\mathrm{PFA, cond.}}| \geq |\nabla E_{\mathrm{PFA, diel.}}| > |\nabla E_{\mathrm{LSL}}|. \tag{3.20}$$

Thus, the PFA provides an upper bound for the Casimir force at all separations. Considering the numerical series expansion, it appears as if the argument would apply to all distances L/R - although this is not mathematically proven here. □

Remark. For later calculations, only the difference in the Casimir energy for slightly different separations L and thus effectively the gradient $\nabla E = \mathrm{d}E/\mathrm{d}L$ is required. Thus, the proof was given in terms of the Casimir force.

For subsequent calculations, the PFA is therefore used as a worst-case approximation of the Casimir energy. Whenever possible, results are cross-verified anc compared with the LSL model.

3.3 Imperfect plate and spheres

In practice, the surfaces of the sphere and plate are not perfectly flat and contain imperfections, leading to small, localized variations in the sphere-plate separation and, consequently to slight changes in the Casimir energy. While, in reality, both the sphere and the plate have rough surfaces, we limit ourselves to the case where the plate is rough and the sphere is smooth, as we do not expect any fundamental changes. Under the PFA, the Casimir interaction solely depends on the surface-to-surface separation $\mathscr{L}$ and thus, all irregularities on the sphere's surface effectively be modeled as an equivalent roughness on the plate. To quantify and estimate the impact of uneven surfaces on the Casimir energy, several representative types of plate imperfections with characteristic amplitude $\Delta\mathscr{L}$ shown in fig. 3.4 have been studied with numerical methods.
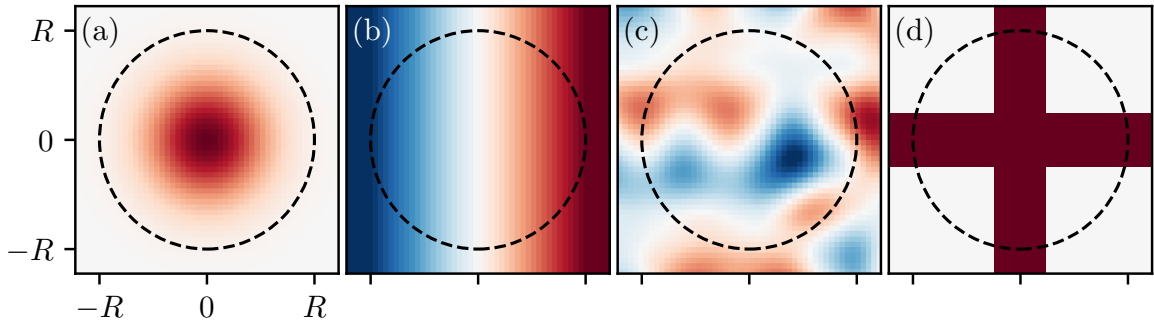

Figure 3.4: A selection of imperfect plates. **(a)** A simple gaussian deformation in the same size as the sphere. **(b)** Linearly inclining plate or a tilted flat plate. **(c)** Uneven and noisy but uniformly random surface realized using *Perlin noise* [46]. **(d)** A cross-shape in the center of the plate.

(a) A *gaussian shaped bump or dip* in the plate can be used to describe a range of possible local deformations comparable in size to the sphere. For a small shield ($r_s \approx R$), thermal vibrations resemble these deformations, as discussed in chapter 5. Displacements with positive or negative amplitudes $\pm\Delta\mathscr{L}$ following a Gaussian profile were studied.

(b) If the characteristic length scale of imperfections is much larger than the sphere's radius and the sphere is sufficiently close to the plate, it experiences a nearly linear gradient in the plate's surface height, effectively behaving as though the plate was tilted. These *linear deflection* can describe thermal vibrations for larger shields $r_s \ll R$. At small gradients, variations in the Casimir potential cancel out in first

order since the potential in the PFA $1/(\mathscr{L} \pm \Delta\mathscr{L})^2 \sim 1/\mathscr{L}^2 \mp 2\Delta\mathscr{L}/\mathscr{L}^3$ depends linearly on the deflection. As a result, no significant change in the total attraction force is expected.

(c) Similarly negligible are *random noisy but uniformly distributed deformations*, provided the typical length scale of the noise is smaller than the sphere's radius. Here, the noise was modeled using *Perlin noise* [46], which produces smooth pseudo-random surface textures commonly used in computer science to imitate surface roughness. Equidistant grid-points are defined, each of which is assigned with a pseudo-random gradient. The noise function follows this gradient in the vicinity of a grid-point and the interpolation between points generates smooth transitions. Due to the uniformness, no large deviations from an ideal flat plate are expected.

(d) Structural features on the plate, such as a *centered cross*, may enhance the stability and rigidity of the shield, potentially reducing thermal vibrations. However, the effects of such features, including amplification of the Casimir interaction, must be investigated further.

The resulting Casimir potentials between a macroscopic sphere and the imperfect surfaces were numerically calculated in the PFA and are shown in fig. 3.5. All imperfections are bounded by the potential between a sphere and a perfectly flat ideal plate moved by a distance $\Delta\mathscr{L}$ closer or farther. This is symbolized by the gray region in fig. 3.5. For the gaussian distributions, this overestimation is not particularly large and especially for large structures, like the cross, this bound is practically reached. As expected, the uniformly distributed noise as well as a slightly tilted plane do not increase the Casimir potential substantially even at small separations. For small imperfections or large separations, plate imperfections are negligible as the relative effect decreases with $\Delta\mathscr{L}/\mathscr{L} \to 0$. However, the considerations made in this section are particularly important for small shields the size of the particles and close distances.
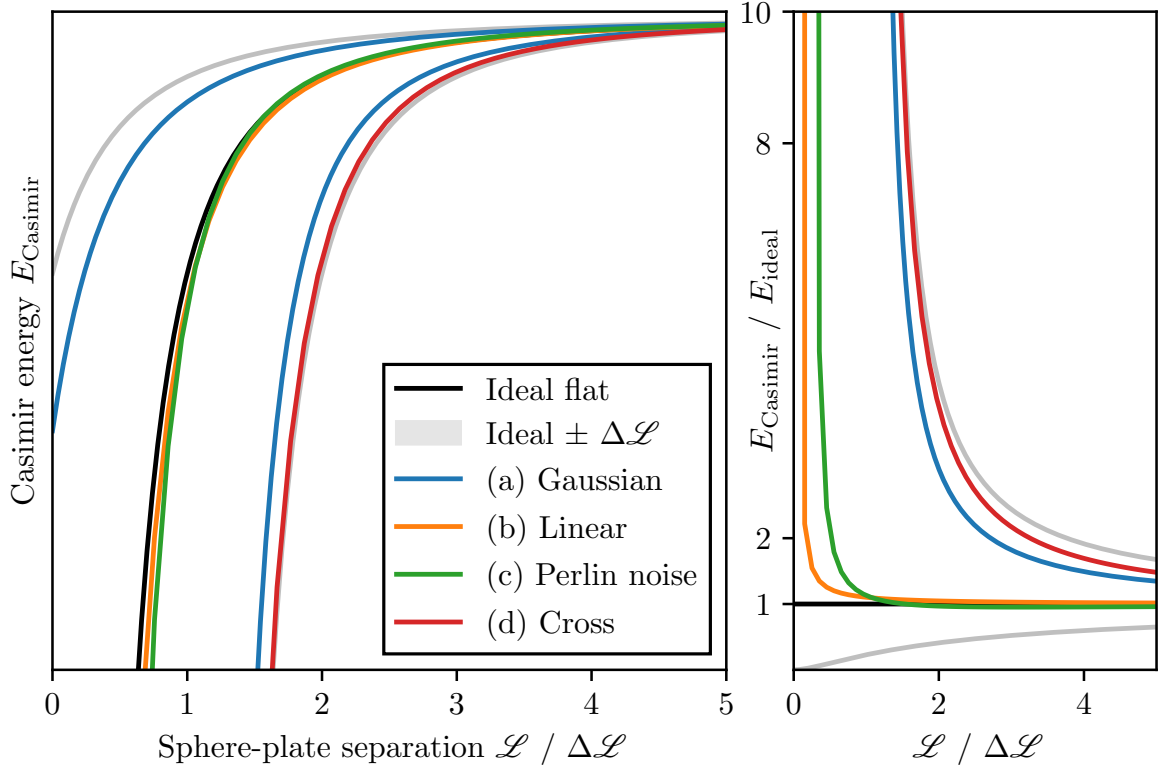
Figure 3.5: Casimir energy between a sphere and plates with surface imperfections shown in fig. 3.4. The gaussian deformation (blue) was calculated for displacements with amplitude $\pm\Delta\mathscr{L}$. The shaded region bounds all imperfections and represents the Casimir energy between a flat plate moved $\pm\Delta\mathscr{L}$ closer or farther to the sphere. In the limit $\Delta\mathscr{L} \ll \mathscr{L}$, all imperfections are negligible.

4 The particle in front of a static shield

The generalized setup of the system described in chapter 2 with the addition of a conducting Faraday shield is shown in fig. 4.1. As before, the particles A and B are delocalized in cat-states with superposition sizes Δx_A and Δx_B respectively. The particles are
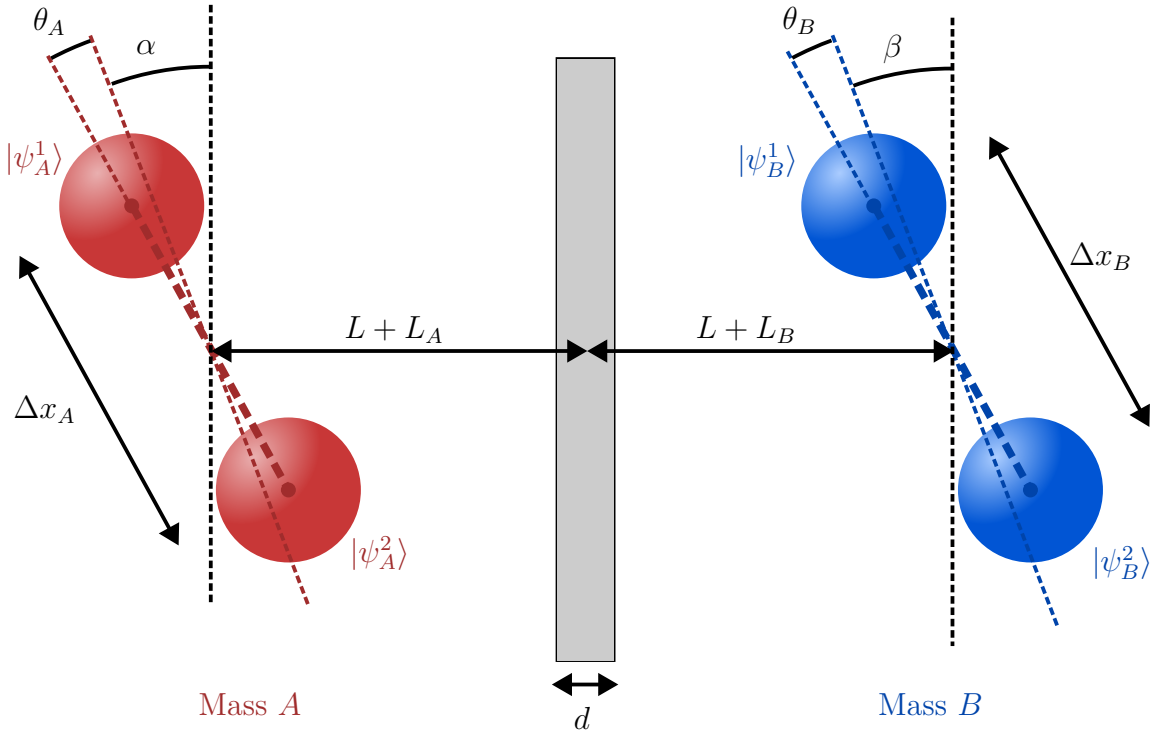

Figure 4.1: Schematic experimental setup for detecting gravitationally induced entanglement between particles A and B with radius R, separated by a distance $2L + L_A + L_B$. Their orientations are defined by angles α and β, with small variations $\theta_{A(B)}$. All variations are assumed to be normally distributed around zero with standard deviation $\Delta L_{A(B)}$ and $\Delta \theta_{A(B)}$. The particles are delocalized in cat-states with size $\Delta x_{A(B)}$ between states $\left| \psi_{A(B)}^1 \right\rangle$ and $\left| \psi_{A(B)}^2 \right\rangle$. A conducting Faraday shield of thickness d is centrally placed.

positioned at a distance L from the shield with the cat-state superpositions oriented at

angles $\alpha, \beta \in [0, \pi)$ relative to the shield. We define the configuration with $\alpha = \beta = 0$ as the "parallel orientation" and $\alpha = \beta = \pi/2$ as the "orthogonal orientation".

If gravity is assumed to be able to mediate entanglement, particles A and B can get entangled. Placing a Faraday shield in the center between the masses should not substantially influence the gravitational entanglement generation. However, Casimir interactions between the shield and particles, especially at small separations, must be accounted for. These interactions contribute only phase shifts to individual cat-states, but do not couple the particles and thus cannot generate additional entanglement - assuming a static shield e.g. at zero temperature.

For a complete picture, experimental challenges and limitations have to be considered. The question remains open on how to verify gravitational entanglement between the two particles. One possibility is to find a suitable entanglement witness [4, 6], which requires knowledge about the specific implementation of the experiment. In this thesis it is assumed, that each cat-state is confined in a truncated two-dimensional Hilbert space, as only the dynamic relative phase differences between two such states are of interest. Consequently, the density matrix has 16 entries, of which only 9 are independent, making reconstruction possible using known matrix properties (e.g., hermiticity $\rho^\dagger = \rho$ and tr $\rho = 1$). Accurate tomography requires numerous measurements due to quantum probabilistic behavior. From run to run, the initial angle $\theta_{A(B)}$ and separation distance $L_{A(B)}$ in the setup will vary, resulting in a mixed initial state ρ_0. Other experimental noise sources, such as variations in the measurement timing, have been considered previously in Ref. [47]. Even if it was possible to place the particles at the exact same position for each measurement, thermal vibrations of the shield induce noisy variations in the particle-shield separation, analyzed in chapter 5. If the random variable $X \in \{\theta_A, \theta_B, L_A, L_B\}$ is subject to statistical variations, the resulting mixed state can be described by

$$\rho = \int\limits_{-\infty}^{\infty} \mathrm{d}X \frac{1}{\sqrt{2\pi}\Delta X} e^{-X^2/2(\Delta X)^2} |\psi_X\rangle\langle\psi_X| , \tag{4.1}$$

where $|\psi_X\rangle$ is the pure state of a single measurement dependent on the random variable X. These variations are assumed to be normally distributed with mean $\langle X \rangle = 0$ and standard deviation ΔX on the basis of the central limit theorem [48, p. 1195]. While correlations between $\theta_{A(B)}$ and $L_{A(B)}$ are possible, they are assumed uncorrelated here as a worst-case estimation. In chapter 5 during the analysis of thermal vibrations of the Faraday shield, cases involving correlated variables due to thermal shield vibrations are analyzed.

Convergence for a finite number of measurements

Experimentally, it would be very interesting to know how fast the averaged density matrix $\bar{\rho}$ after a finite number of N measurements converges to the idealized asymptotic mean $\langle\rho\rangle$ given by eq. (4.5), which is calculated and analyzed in depth in the next two

sections. After N measurements, the sample average is given by

$$\bar{\rho} = \frac{1}{N} \sum_{k=1}^{N} \rho(X_k) \tag{4.2}$$

where $\rho(X)$ depends on the random variable $X \in \{\theta_{A(B)}, L_{A(B)}\}$ and X_k is the k-th sample drawn from the normal distribution $\mathcal{N}(0, (\Delta X)^2)$ [7]. As $N \to \infty$, the law of large numbers and in particular the central limit theorem (CLT) ensures that $\bar{\rho} \to \langle \rho \rangle$ [48, p. 1195]. According to the CLT, the sample average $\bar{\rho}(X)$ fluctuates around $\langle \rho \rangle$ with a standard deviation given by the Berry-Esseen theorem for independent and identically distributed random variables X_k by $\sigma \sim N^{-1/2}$ [49]. Thus, if the placements of the particles in each measurement are completely independent from each other, the rate of convergence to the ideal mean $\langle \rho \rangle$ is governed similar to the shot-noise limit by $\mathcal{O}(1/\sqrt{N})$.

It is however very likely that measurements are mostly performed consecutively in the same trap so that the placements in successive measurements are correlated. The correlations $\text{Cov}[\rho(X_i), \rho(X_j)] = c_{|i-j|}$ between the i-th and j-th measurement should therefore decrease with increasing $|i-j|$. The variance of $\bar{\rho}$ is now dependent of these correlations in the form [48, p. 1227]

$$\text{Var}[\bar{\rho}] = \frac{1}{N^2} \sum_{i,j=1}^{N} \text{Cov}[\rho(X_i), \rho(X_j)] = \frac{1}{N}\text{Var}[\rho] + \frac{2}{N^2} \sum_{n=1}^{N-1} (N - n)c_n \tag{4.3}$$

where $\text{Cov}[\rho, \rho] = \text{Var}[\rho]$ was used for the variance of the mean density matrix $\langle \rho \rangle$. For correlations $c_n \sim n^{-\alpha}$ ($\alpha < 1$) the sum in eq. (4.3) can by asymptotically calculated by the Euler-Maclaurin formula and scales like

$$\sum_{n=1}^{N-1} (N - n)n^{-\alpha} \xrightarrow{N \to \infty} \int_1^N \mathrm{d}n\, (N - n)n^{-\alpha} \sim N^{2-\alpha} \tag{4.4}$$

which results in $\text{Var}[\bar{\rho}] \sim N^{-\alpha}$. In the asymptotic limit the standard deviation of the sample average $\sqrt{\text{Var}[\bar{\rho}]}$ and thus the convergence rate to the mean $\langle \rho \rangle$ scales with $\mathcal{O}(1/\sqrt{N^\alpha})$. This convergence is arbitrary slow for small α (if the setup does not change a lot between individual measurements) and thus the calculations in the next sections are just a worst-case estimation of the actual experimental results. If a weaker correlation in the form of $c_n \sim e^{-\alpha n}$ is assumed, the convergence rate is again asymptotically governed by $\mathcal{O}(1/\sqrt{N})$.

---

[7]Here it isn't strictly required that X_k are normally distributed. As long as they are i.i.d. random variables, any distribution is sufficient for the following argumentation [48, p. 1195].

4.1 Entanglement generation

The averaged state $\langle \rho \rangle$ after multiple measurements is given by

$$\langle \rho \rangle = \int_{-\infty}^{\infty} \mathrm{d}\theta_A p(\theta_A) \int_{-\infty}^{\infty} \mathrm{d}\theta_B p(\theta_B) \int_{-\infty}^{\infty} \mathrm{d}L_A p(L_A) \int_{-\infty}^{\infty} \mathrm{d}L_B p(L_B) \; \rho(\theta_A, \theta_B, L_A, L_B)$$

(4.5)

where $p(\,\cdot\,)$ represents the Gaussian distributions of the random variables $\theta_{A(B)}$ and $L_{A(B)}$ with standard deviations $\Delta\theta$ or ΔL respectively. $\rho(\theta_A, \theta_B, L_A, L_B)$ denotes the state of a single measurement, dependent on the initial setup of the system. The state ρ_0 at $t = 0$ is given similarly as in eq. (2.2). Additionally to mutual gravitational coupling, the Casimir interactions of the state $\left|\psi_{A(B)}^{(i)}\right\rangle$ $(i = 1, 2)$ with the Faraday shield induce the phase $\phi_{A(B),\,\mathrm{Cas}}^{(i)}(t)$. Using the two different models for the Casimir attraction for large and small separations given by eq. (3.12) and eq. (3.12), it follows

$$\phi_{A(B),\,\mathrm{Cas}}^{(i)}(t) = \frac{t}{\hbar} \begin{cases} \frac{3\hbar c}{8\pi} \left(\frac{\varepsilon_r - 1}{\varepsilon_r + 2} \right) \frac{R^3}{(L_{A(B)}^{(i)})^4} & \text{for large separations (LSL)} \\[3mm] \frac{\hbar c \pi^3}{720} \varphi(\varepsilon_r) \left(\frac{\varepsilon_r - 1}{\varepsilon_r + 1} \right) \frac{R}{(\mathscr{L}_{A(B)}^{(i)})^2} & \text{for small separations (PFA)} \end{cases}$$

(4.6)

Here, $L_{A(B)}^{(i)}$ and $\mathscr{L}_{A(B)}^{(i)} = L_{A(B)}^{(i)} - R$ are the distances between the particles and the shield's surface given by

$$L_A^{(i)} = L + L_A - \frac{d}{2} \pm_i \frac{\Delta x_A}{2} \sin(\alpha + \theta_A) \tag{4.7}$$

$$L_B^{(i)} = L + L_B - \frac{d}{2} \mp_i \frac{\Delta x_B}{2} \sin(\beta + \theta_B) \tag{4.8}$$

where $\pm_i$ distinct between the two cat-states of a single particle. The phase imprinted by the mutual gravitational interactions between states $\left|\psi_A^{(i)}\right\rangle \otimes \left|\psi_B^{(j)}\right\rangle$ is given analogue to the previous calculations in chapter 2 as

$$\phi_{\mathrm{Grav}}^{(ij)}(t) = \frac{t}{\hbar} \frac{G M_A M_B}{L^{(ij)}}. \tag{4.9}$$

The distance $L^{(ij)}$ between the states $A^{(i)}$ and $B^{(j)}$ is given by

$$L^{(ij)} = \sqrt{ \left(2L + L_A + L_B \pm \frac{\Delta x_A}{2} \sin(\alpha + \theta_A) \mp \frac{\Delta x_B}{2} \sin(\beta + \theta_B) \right)^2 + }$$
$$\overline{ \left(\frac{\Delta x_A}{2} \cos(\alpha + \theta_A) \pm \frac{\Delta x_B}{2} \cos(\beta + \theta_B) \right)^2 }. \quad (4.10)$$

Expanding to first order in $\Delta x_{A(B)} \ll L$, $\theta_{A(B)} \ll 1$ and $L_{A(B)} \ll 1$ (which is justified as seen in the following), the averaged evolved state $\langle \rho \rangle$ in eq. (4.5) is analytically solvable,

Orientation	Particle size		L	Δx	Shield size [b]	
	Radius R	Mass M [a]			d	r_s
Parallel	$10\,\mu\text{m}$	$\approx 10^{-11}\,\text{kg}$	$2R = 20\,\mu\text{m}$	$100\,\text{nm}$	$100\,\text{nm}$	$1\,\text{cm}$
$(\alpha = \beta = 0)$	$= 10^{-5}\,\text{m}$	$= 5 \times 10^{-4}\,m_p$				

[a] Here $m_p = \sqrt{c\hbar/G} \approx 2.17 \times 10^{-8}\,\text{kg}$ is the Planck mass. [b] The required size of the shield is later estimated in section 5.1.

Table 4.1: Default parameters for the setup in fig. 4.1. Maximum entanglement is reached after $t_{\max} = 259\,\text{mn}$ for these parameters. They were chosen in accordance with multiple proposals [29, 50]. Both particles are assumed to be identical. The thickness d and radius r_s of the shield is estimated in section 5.1.

as shown in appendix B.2. Assuming $\Delta\theta_A = \Delta\theta_B \equiv \Delta\theta$ and $\Delta L_A = \Delta L_B \equiv \Delta L$, the off-diagonal elements (the so-called *coherences*) decay as

$$\langle \rho_{kl} \rangle = \frac{1}{4} e^{i\Delta\phi_{kl}(t)} \exp\left\{ -\frac{(\xi_{kl})^2}{2} (\Delta\theta)^2 t^2 \right\} \exp\left\{ -\frac{(\zeta_{kl})^2}{2} (\Delta L)^2 t^2 \right\} \tag{4.11}$$

where $\Delta\phi$, ξ and ζ are substitutes for lengthy expressions given by eq. (B.2), eq. (B.15) and eq. (B.18), which are dependent on system parameters. For $\Delta\theta, \Delta L \to \infty$ or $t \to \infty$, coherences vanish, resulting in a maximally mixed state with $\operatorname{tr}\rho^2 = 1/4$ - which is not entangled. For large variations in the initial placement of the particles, one therefore expects the loss of entanglement.

In special cases of two identical particles and $\alpha = \pm\beta$, the logarithmic negativity is approximated by

$$E_N(\langle\rho\rangle) = \max\left\{ 0,\ \log_2\left(e^{-\gamma}\left(\cosh\gamma + |\sin\phi|\right) \right) \right\} \tag{4.12}$$

where the decoherences $\gamma = \left(\xi^2(\Delta\theta)^2/2 + \zeta^2(\Delta L)^2/2 \right) t^2$ due to variations in the initial placement is derived in eq. (B.21) and the phase ϕ is given by eq. (4.15) in the next section. Numeric results confirm the first order approximation and are shown in fig. 4.2 for different values of $\Delta\theta$ and ΔL in the parallel orientation. For small placement variations, entanglement is virtually unaffected but at the critical thresholds $\Delta\theta_{\text{crit}}$ and ΔL_{crit} entanglement is completely lost. The critical decoherence γ_{crit} is given by

$$\gamma_{\text{crit}} = \log\left(1 + \sqrt{2}\right) = \text{const.} \tag{4.13}$$

resulting in $\Delta\theta_{\text{crit}} \propto 1/(\xi t)$ and $\Delta L_{\text{crit}} \propto 1/(\zeta t)$. For the used parameters shown in table 4.1, the threshold is around $\Delta\theta_{\text{crit}} \approx 6 \times 10^{-10}\,\text{rad}$ and $\Delta L_{\text{crit}} \approx 1.4 \times 10^{-10}\,\text{m}$, which seems quite challenging experimentally. For all these calculations, the radius of the particles was set to $R = 10^{-5}\,\text{m} = 10\,\mu\text{m}$ with corresponding masses $M = 4/3\pi R^3 \rho_{\text{Silica}} \approx$
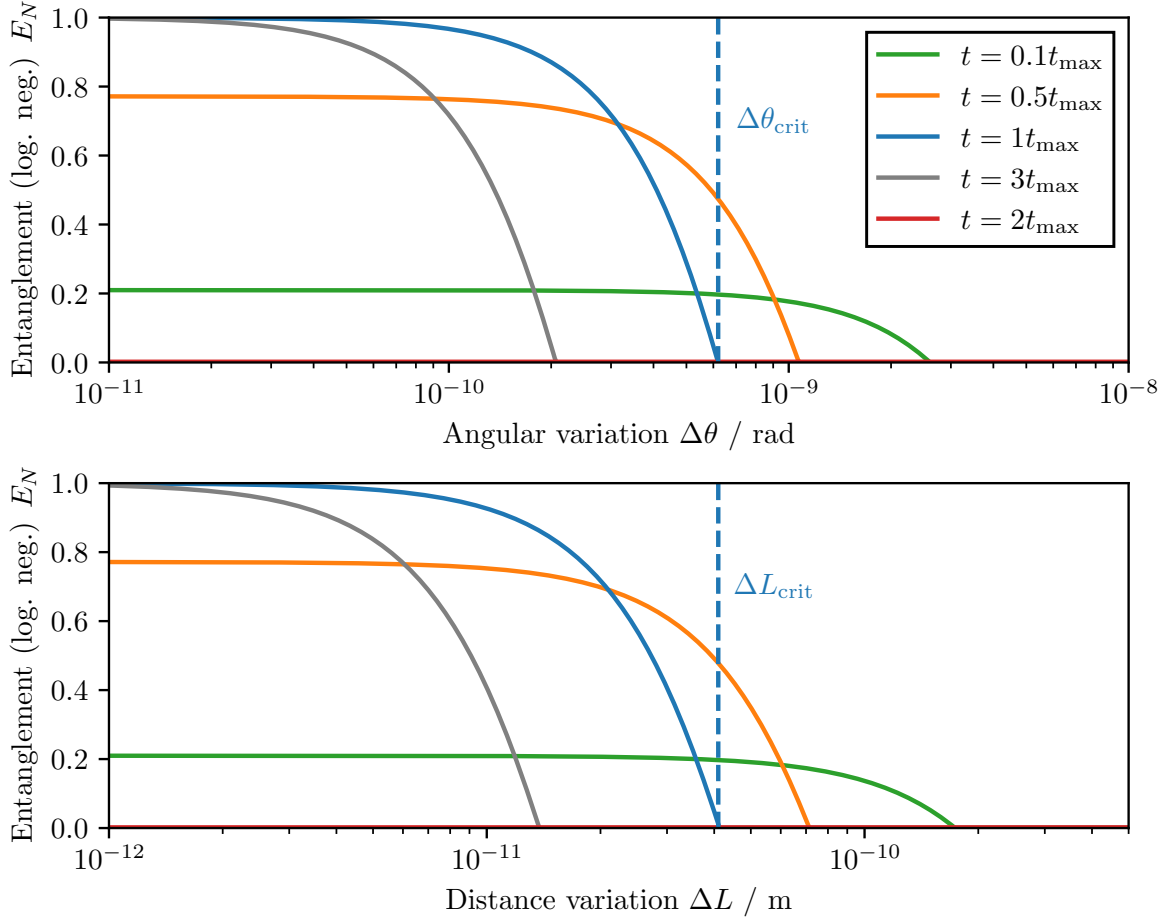
Figure 4.2: Entanglement quantified by the logarithmic negativity (eq. (2.15)) dependent on the angular variation $\Delta\theta$ and the distance variation ΔL in the parallel configuration. The entanglement is shown at different times, where $t_{\max} \approx 258\,\mathrm{ms}$ is the time of maximal entanglement from eq. (2.18). At the critical point $\Delta\theta_{\mathrm{crit}}$ or ΔL_{crit} all entanglement is lost.

$1.1 \times 10^{-11}\,\mathrm{kg}$. A particle-shield separation of $L = 2R$ and a superposition site of $\Delta x = 100\,\mathrm{nm}$ were chosen. In the rest of this thesis, if not otherwise specified, these parameters are used as a default. For convenient retrieval, they are collectively displayed in table 4.1.

These values agree with the parameter regime typically considered for such experiments [29, Timestamp: 51:00], as they result in a low one-run duration of $t_{\max} \approx 258\,\mathrm{ms}$. Other proposals suggest a similar parameter set generally differing only by single orders of magnitude (see e.g. the Tab. 1 in Ref. [50]). It is important however to note, that these parameters are orders of magnitude beyond current experimental capabilities: The largest mass studied in matter-wave interferometry is about $4 \times 10^{-23}\,\mathrm{kg}$ [18] with an superposition size of $\Delta x \gtrsim 500\,\mathrm{nm}$. In solid-state mechanical systems, quantum con-

trol and ground-state cooling have been demonstrated with masses of 10^{-13} kg [26] and 10^{-8} kg [51] for mechanical oscillators coupled to superconducting qubits, or 10^{-11} kg [52] for entangled diamonds, although with very short coherence times $\lesssim 1\,\mu$s. Also very impressive and notable is the cooling of the ~ 40 kg LIGO mirrors close to their quantum ground state [53]. In contrast, the smallest mass with a measurable gravitational coupling is around 92 mg [19]. The field of levitated nano-particles bridge molecular superposition and mechanical systems, offering exceptional quantum control, high force sensitivity and long coherence times up to seconds [29]. Thus many proposals aim to measure quantum entanglement due to gravity between trapped particles [3].

Nonetheless, the required accuracy in the placement of the particles appears very challenging experimentally. However, looking at fig. 4.2, for shorter times $t < t_{\max}$, greater variations in particle placement can be tolerated at the cost of reduced entanglement. At these shorter times, the gravitational interaction has not fully entangled the particles, and decoherence (which scales as $\gamma \propto t^2$) has not yet significantly developed. If achieving full entanglement is not required and *any* amount of entanglement $E_N > 0$ suffices, it may be advantageous to perform measurements at $t < t_{\max}$. This, of course, requires ensuring that other entanglement mechanisms, such as direct or indirect coupling, contribute smaller entanglement rates (see chapter 5 for further discussion). Additionally, decoherence effects from collisions with air molecules and thermal black-body radiation should be taken into account. The optimal measurement time for a required level of entanglement is depicted in fig. 4.3. The figure also provides the corresponding maximum allowable variation for a given time. Conversely, for fixed variations, the optimal measurement time and maximum attainable entanglement can be determined. It also can be seen that at times $2kt_{\max}$, $k \in \mathbb{N}$ no entanglement is measurable, coinciding with the findings for the ideal scenario in chapter 2.
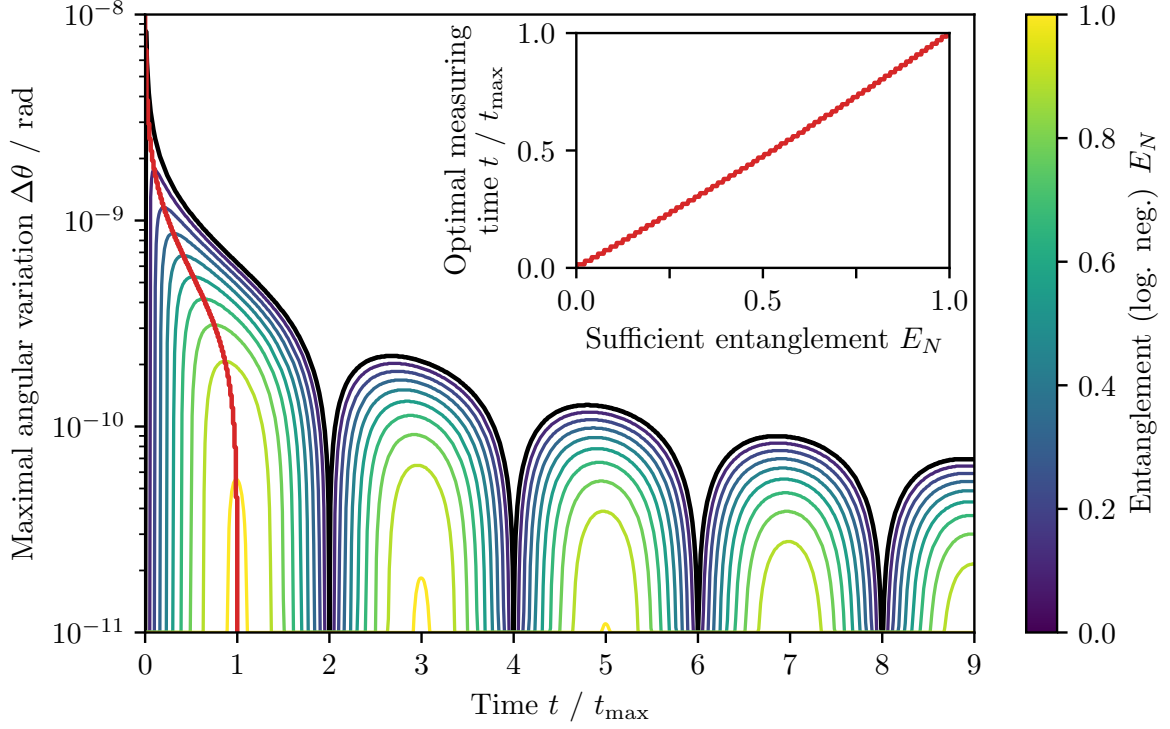
Figure 4.3: Maximal angular variation for given times after which a specific amount of entanglement E_N is still measurable. The setup parameters are taken from table 4.1. The outer most black line corresponds to the time dependence of $\Delta\theta_{\mathrm{crit}}$. A fully entangled state with $E_N = 1$ is only measurable at $t = t_{\mathrm{max}}$ with a maximally possible angular variation of around $10^{-11}\,\mathrm{rad}$. The red curve on the top left shows the optimal measuring time for a specific amount of entanglement. Correspondingly, the red curve in the main figure shows the maximal angular variation for which this goal is reachable. At times $2kt_{\mathrm{max}}$, $k \in \mathbb{N}$ no entanglement can be measured.

4.2 The optimal setup

With the general framework in hand, the next logical question to ask is, whether the stability against placement-variations can be improved. The rule of thumb for these optimizations is the following: Increase the gravitational interaction by either having heavier and larger particles or by reducing the separation distance L without substantial sacrifices of experimental realization. As an example, the stability increases intuitively by increasing the separation distance L. However, this does also increase the time $t_{\max} \propto L^3$ until the maximum amount of entanglement can be measured which would increase the total time $\sim N t_{\max}$ of the experiment with N individual measurements. It is not immediately obvious, how the stability and the maximum possible variations $\Delta\theta_{\mathrm{crit}}$ and ΔL_{crit} behave for the change in parameters. In the following section, precisely the dependence of this stability is discussed for altering the orientation α, β, the particle-shield separation L, the mass $M_A = M_B \equiv M$ and the superposition size $\Delta x_A = \Delta x_B \equiv \Delta x$ for two identical particles.

4.2.1 Orientation

One of the arguably easiest parameter to change experimentally is the orientation of the superpositions, which is quantified by α and β in fig. 4.1. As already seen in fig. 2.2, the entanglement dynamics are dependent on the orientation. In the parallel orientation, the states take twice as long as in the orthogonal orientation to become maximally entangled. In general, it is advantageous to aim for the highest entanglement rate and thus the smallest $t_{\max}(\alpha, \beta)$, as this requires a shorter coherence time and thus reduces the total time of the experiment. The previous results from chapter 2 can be further generalized for an arbitrary orientation α, β. The logarithmic negativity is given by (derived in appendix B.1)

$$E_N = \log_2\left(1 + |\sin\phi|\right) \tag{4.14}$$

where ϕ is now dependent on the orientation and is defined as (for $\Delta x \ll L$)

$$\phi = \frac{GM_A M_B t \Delta x_A \Delta x_B}{8\hbar L^3}\left(\sin\alpha \sin\beta - \frac{1}{2}\cos\alpha \cos\beta\right). \tag{4.15}$$

The maximum entanglement $E_N = 1$ is reached for $\Delta\phi = \pm\pi/2$ and thus after a time

$$t_{\max}(\alpha, \beta) = \frac{4\pi\hbar L^3}{GM_A M_B \Delta x_A \Delta x_B}\left|\sin\alpha \sin\beta - \frac{1}{2}\cos\alpha \cos\beta\right|^{-1}. \tag{4.16}$$

For some specific symmetric cases, the resulting times for different orientations are shown in fig. 4.4. The global minima of $t_{\max}(\alpha, \beta)$ is attained in the orthogonal orientation. This is not surprising considering that this orientation maximizes the *differences in separation distances* between all superposition states. Much more interesting and surprising are the unanticipated singularities in fig. 4.4 which appear for

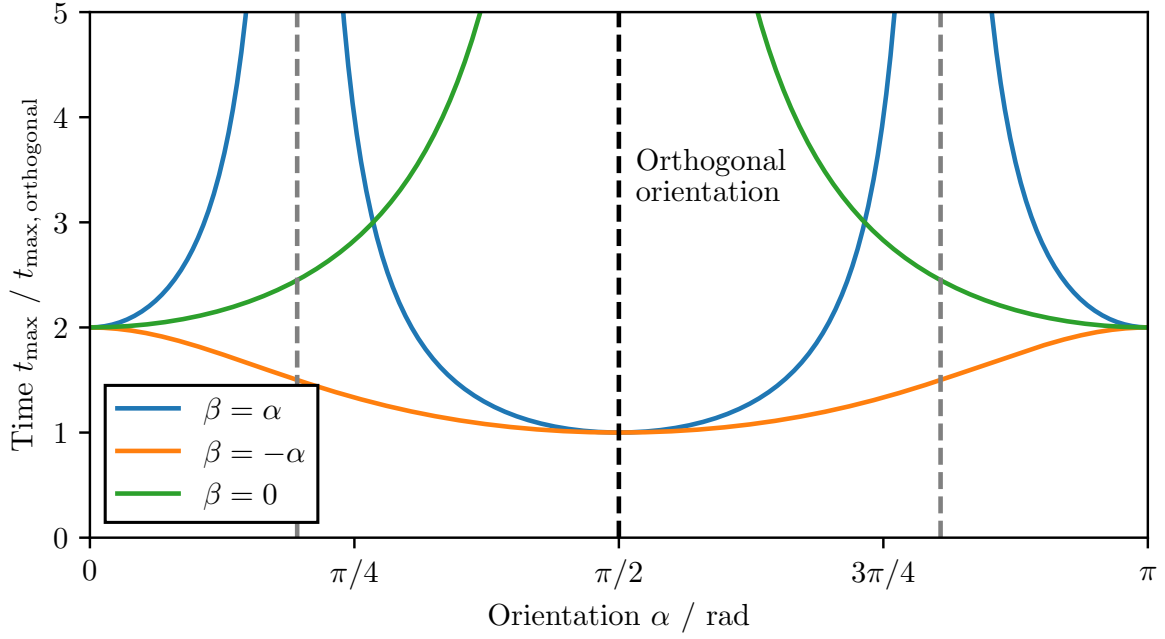$$\sin\alpha \sin\beta = \frac{1}{2}\cos\alpha \cos\beta. \tag{4.17}$$

Figure 4.4: Time $t_{\max}$ after which maximum entanglement ($E_N = 1$) is reached for different orientations. Only the most interesting and highly symmetric cases $\alpha = \pm\beta$ and $\beta = 0$ are shown. The singularity $t_{\max} \to \infty$ for $\beta = 0$ and $\alpha = \pi/2$ is expected. The two other singularities at $\alpha = \beta = 2\arctan\left(\sqrt{3} \pm \sqrt{2}\right)$ are explainable by the "harmonic mean" in fig. 4.5.

For $\beta = 0$ the singularity at $\alpha = \pi/2$ is not surprising. In this configuration, the distances $|\psi_A^1\rangle \leftrightarrow |\psi_B^{1,2}\rangle$ and $|\psi_A^2\rangle \leftrightarrow |\psi_B^{1,2}\rangle$ are identical and thus these states accumulate the same phases, resulting in a factorable global phase. In the case of $\alpha = \beta$, the two singularities are precisely given in the orientation

$$\alpha = \beta = 2\arctan\left(\sqrt{3} \pm \sqrt{2}\right) \approx 90° \pm 54.74°. \tag{4.18}$$

There does exist a non-obvious geometric interpretation why no entanglement is generated exactly in this configuration, however all 4 separation distances between the states form the "harmonic mean" visualized in fig. 4.5. Here, in the limit $\Delta x \ll L$ every local
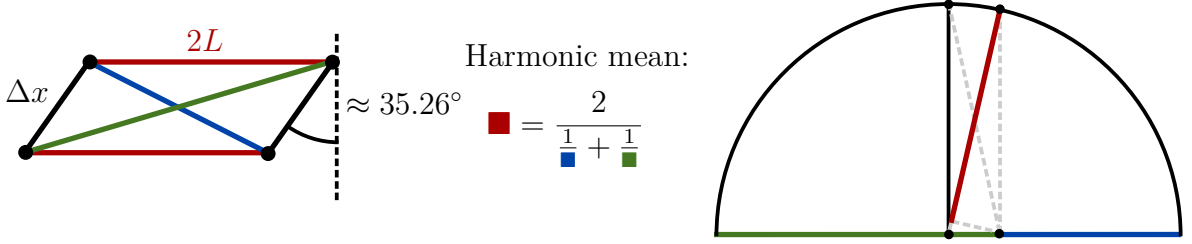

Figure 4.5: left: The system in the orientation $\alpha = \beta = 2\arctan\left(\sqrt{3} - \sqrt{2}\right)$. For $\Delta x \ll L$, all separation distances exactly form the *harmonic mean*. Here, the phases due to the mutual gravitational interaction precisely cancel out resulting in no entanglement. **right:** Geometric visualization of the harmonic mean.

phase precisely cancels out resulting in a loss of entanglement. To avoid all these singularities, it is advisable to always take $\alpha = -\beta$, where all orientations result in roughly similar entanglement times $t_{\max}$, at most only differing by a factor of 2.

It should come as no surprise that the different orientations exhibit different stabilities. Naturally, one would expect the orthogonal configuration to be much more sensitive to angular variations than the parallel one. In contrast, the parallel configuration should be much more stable against variations L, as no phase difference is induced between the two superposition states $|\psi_{A(B)}^1\rangle$ and $|\psi_{A(B)}^2\rangle$ of the particle A (B).

The effect of different orientations on the stability against angular variations and the behavior of the critical angular variation $\Delta\theta_{\mathrm{crit}}$ is shown in fig. 4.6. As expected, the orthogonal configuration is the most stable against these kind of variations. This is, because the dephasing ultimately depends on the distance between the state and the shield $L \pm \Delta x/2\cos\theta \approx L \pm \Delta x/2(1 - \theta^2/2)$, which is a only second order effect of the angular variations θ. This explains the apparent "infinitely" good stability in the figure, as the analytical solution only uses first order approximations in θ. Exact numerical results however cap the stability at $\Delta\theta_{\mathrm{crit, orthogonal}} \approx 7.3 \times 10^{-5}\,\mathrm{rad}$.

Respectively, the stability against distance variations ΔL_{crit} for different orientations is shown in fig. 4.7. Again aligning with expectations, the parallel configuration is (in theory) exhibits an infinite stability. One however could argue, that a for this to hold,
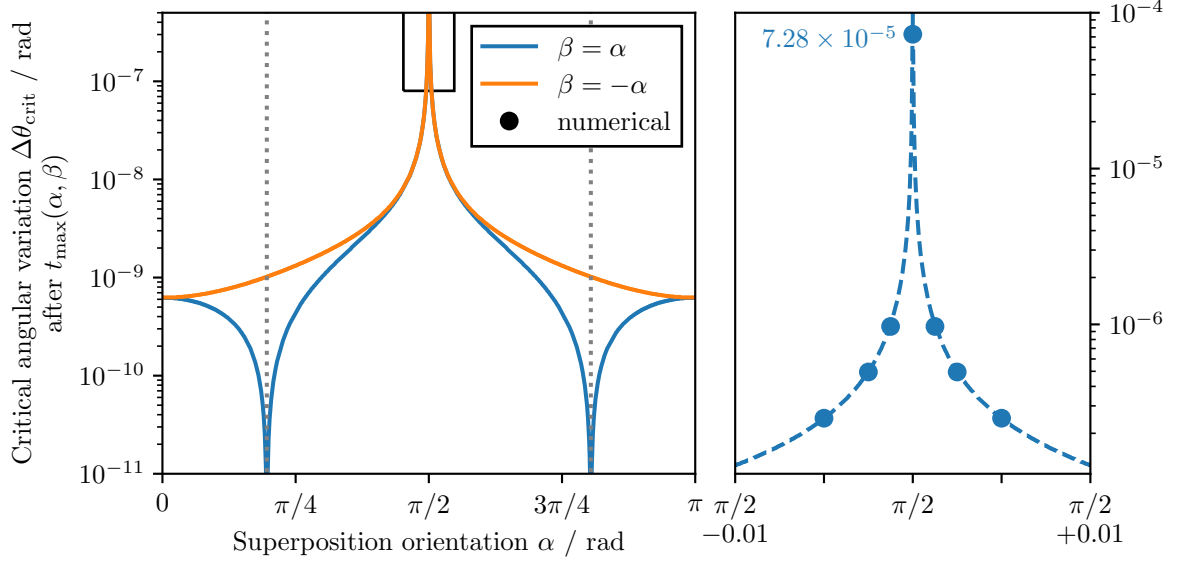
Figure 4.6: Critical angular variation $\Delta\theta_{\mathrm{crit}}$ for different orientations after the time $t_{\max}(\alpha, \beta)$ for which maximum entanglement is reached. The ***orthogonal orientation*** magnified on the right is very stable against angular variations and only numerical methods show a finite stability value. The singularities in the left figure for $\alpha = \beta$ arise from the fact, that these orientations need infinite time to entangle as already seen in fig. 4.4.
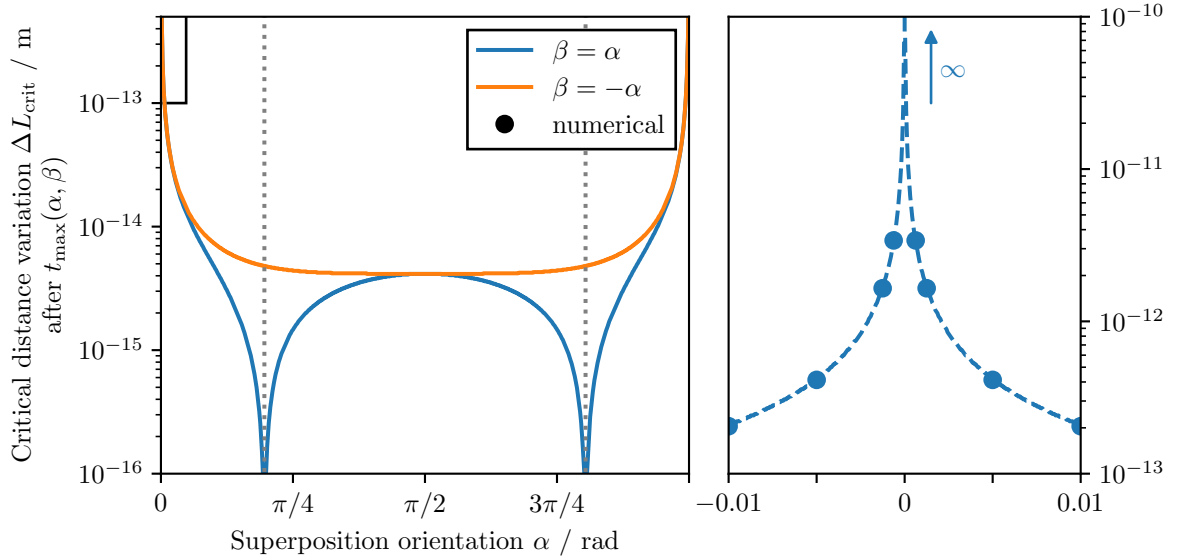

Figure 4.7: Critical distance variation ΔL_{crit} for different orientations after a time $t_{\max}(\alpha, \beta)$. Here, the ***parallel orientation*** (magnified on the left) is infinitely stable against placement variations.

the uncertainties in the angular placement have to be zero. As could be seen in fig. 4.6, these variations are at most around $\sim 5 \times 10^{-5}$ rad and thus a realistic upper bound for the minimum required distance variations is given by $\Delta L_{\text{crit,parallel}} = \Delta L_{\text{crit}}(\alpha \approx 5 \times 10^{-5}\,\text{rad}) \simeq 4 \times 10^{-11}\,\text{m}$. It is important to keep in mind, that these bounds can be improved substantially by e.g. increasing the separation distance L, the particle size R or the superposition size Δx.

Considering these results, the parallel orientation seems to be the more stable and therefore favorable option, even if the requires coherence times t_{max} are twice as long. Keeping particle-shield separation variations below $0.01\,\text{pm}$ in the orthogonal orientation - even smaller than size of a single atom - is extremely challenging, especially under the additional consideration of the thermal vibrations of the shield and the particles, which are in the same order of magnitude as seen later in chapter 5. With this framework on hand, it is possible to generate the stability diagram in fig. 4.8, showing the optimal orientation in which the most entanglement can be measured. For most combinations of ΔL and $\Delta \theta$, entanglement is exclusively given in either the parallel or orthogonal orientation.
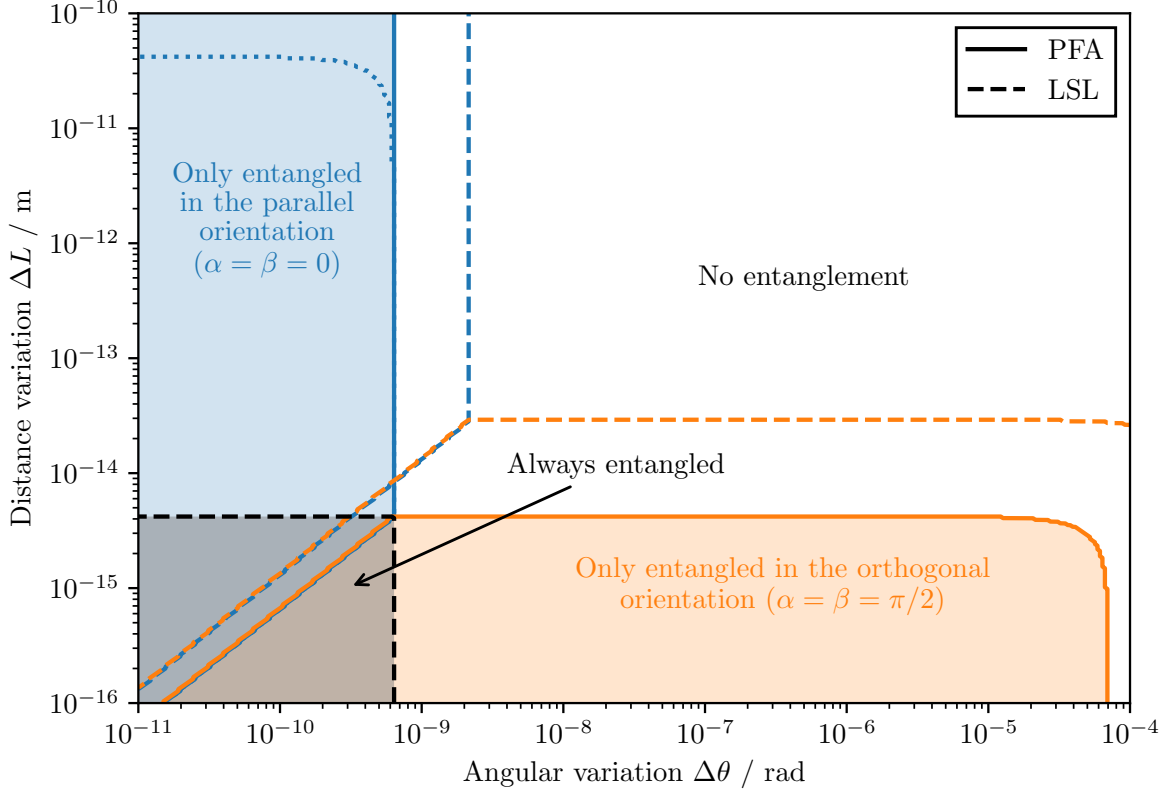
Figure 4.8: Optimal orientation for the experimental setup dependent on the variations
in angle $\Delta\theta$ and distance ΔL for a initial separation distance of $L = 2R =$
2×10^{-5} m at time t_{max}. The different predictions for the proximity-force-
approximation (PFA) and the large-separation-limit (LSL) are shown. At
a distance of $L = 20\,\mu$m the actual casimir interaction is somewhere in the
middle between both approximations. In the region where entanglement is
given regardless of the orientation (the bottom left), the orientation with
more entanglement is still colored. The dotted line corresponds to the
realistic upper bound discussed in the text.

4.2.2 Separation, mass and superposition size

It is possible to improve the placement accuracies required in the initial placement of the particles by changing the parameters in table 4.1. The particle-shield separation L in particular can be adjusted easily over a wide range and one is only limited in the ability of trapping close to the shield discussed in section 4.3 and the size of the experimental setup. The critical angular variation $\Delta\theta_{crit}$ for different L is shown in fig. 4.9. A similar

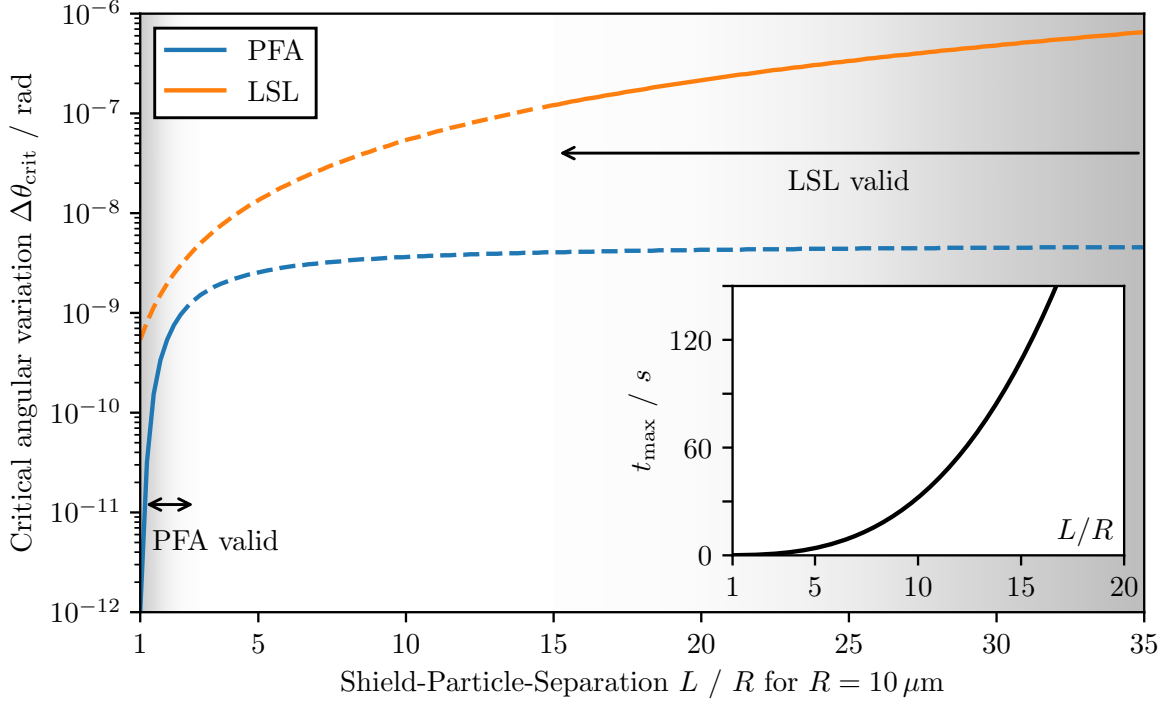**Figure 4.9:** Stability against angular variations for increasing separation distances L in units of $R = 10\,\mu m$ after a time $t_{max}(L)$. The dependence on the radius can be seen in fig. 4.10. Two models for the casimir-interaction are shown: The proximity-force-approximation (PFA) and the large-separation-limit (LSL). The regions outside the models validity are indicated with dashed lines. In the bottom right the time $t_{max}(L) \propto L^3$ is shown.

figure can be created for the change of ΔL_{crit}, but as already discussed previously, the setup in the parallel orientation is very stable against variations in the separation distance, so only angular variations have to be considered.

It is intuitively clear, that a larger separation improves the stability as the relative effect of the variations $\sim \Delta x \sin\theta \ll L$ decreases and the Casimir potential tends towards zero. However, a larger separation also slows down the entanglement generation, as $t_{max} \propto L^3$. The combination of both effects leads to the results shown in fig. 4.9. Both models for the Casimir interaction for either small separations $L \sim R$ (PFA) or large separations $L \gg R$ (LSL) have been considered and the regions of validity are shaded

in gray. Looking at the dependence of the critical point eq. (4.13) on the separation, it becomes evident that

$$\Delta\theta_{\text{crit}} \sim 1/(\xi t) \sim \frac{(L - R - d/2)^3}{t_{\text{max}}} \sim \frac{(L - R - d/2)^3}{L^3} \tag{4.19}$$

for small separations (ξ is given by eq. (B.15)) and similarly $\Delta\theta_{\text{crit}} \sim L^2$. For these first order approximations, it was used that the Casimir force is much larger than the gravitational interaction for all $L \lesssim 40\,\text{m}$ (in fig. 4.9, the match of this approximation is $R^2 = 0.99$).

Contrary to L, the size of the particle R and thus the mass M cannot be changed easily over a wide range of possible values. Estimations suggest, that masses of around $10^{-11}\,\text{kg} \approx 10^{-3}m_p$ could be possible to use for the detection of gravitationally induced entanglement [29, Timestamp 51:00]. Nevertheless, the effect of a larger particle on angular variations is observed and shown in fig. 4.10. The particles are most likely made
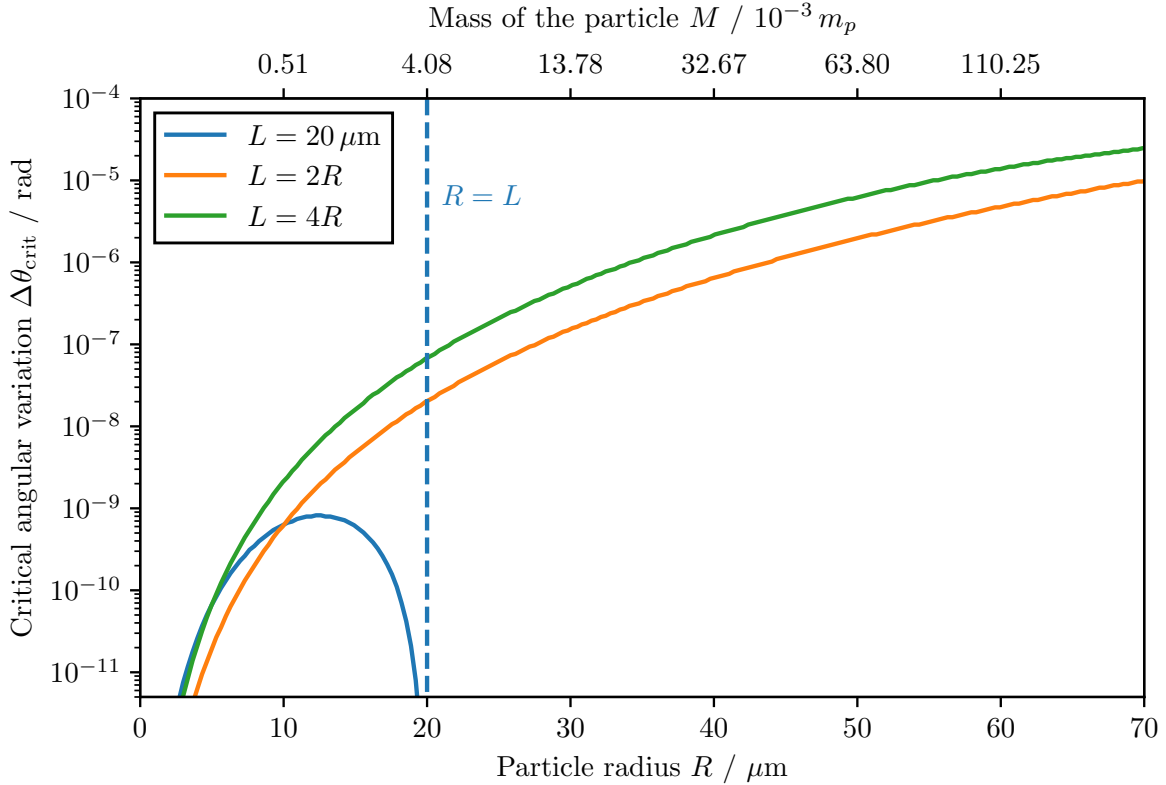

Figure 4.10: Critical angular variation $\Delta\theta_{\text{crit}}$ for different sized particles after a time $t_{\text{max}}(M)$. The mass of the corresponding particle in units of the Planck mass $m_p = \sqrt{\hbar c/G} \approx 2.176 \times 10^{-8}\,\text{kg}$ is given on the top axis. For particles as large as the separation $R = L$, the surface-to-surface separation is almost zero, resulting in large casimir forces and thus no entanglement.

out of silica (SiO_2) with density $\rho_{\text{Silica}} = 2648\,\text{kg/m}^3$, as this material has been widely

used in experiments on levitated nanoparticles [54, 55]. Denser materials like lead or osmium [3] in magnetic traps could potentially be considered as the required particle radius and the number of atoms in a single particle are reduced. The entanglement generation fastens substantially for larger particles as $t_{\max}$ scales with M^{-2} and thus effectively with R^{-6}. The dependence of $\Delta\theta_{\mathrm{crit}}$ on R can be determined in first order to

$$\Delta\theta_{\mathrm{crit}} \sim \frac{(L-R-d/2)^3}{Rt_{\max}} \sim \frac{(L-R-d/2)^3 R^6}{RL^3} \tag{4.20}$$

for small separations and in the special case where $L \propto R$, a scaling of $\Delta\theta_{\mathrm{crit}} \sim (R - d/2)^3 R^2$ is expected. Both cases are shown in fig. 4.10.

Similarly to the particles size, the spatial extension of the coherent superposition of the center-of-mass motion Δx can most likely not be changed substantially. The delocalizations are, considering the current record in matter-wave experiments of $500\,\mathrm{nm}$ for $4 \times 10^{-23}\,\mathrm{kg}$ [18], smaller than the particles radius. In fig. 4.11 the effect of the superposition size on the critical angular variation is shown. A larger superposition would
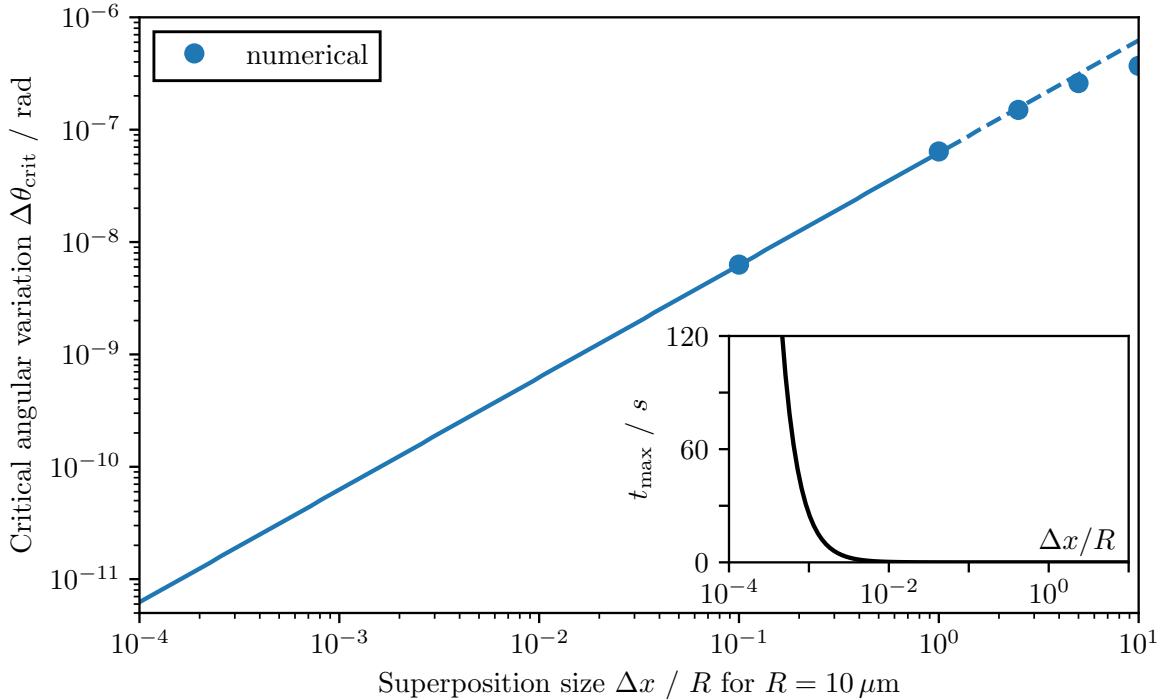
Figure 4.11: Effect of the superposition size Δx on the critical angular stability $\Delta\theta_{\mathrm{crit}}$ after a time $t_{\max}(\Delta x)$. For $\Delta x \gtrsim R$, numerical results are used. In the lower left, the time till maximum entanglement $t_{\max} \propto (\Delta x)^{-2}$ is shown. For $\Delta x \ll R$, the resulting relation between Δx and $\Delta\theta_{\mathrm{crit}}$ is linear.

increase the entanglement generation as the relative phase differences between the states increase, leading to $t_{\max} \propto 1/(\Delta x)^2$. Simultaneously, a larger superposition size increases

the effect of angular variations, as they depend on $\sim \Delta x \sin(\theta)$. The effective scaling of the angular variations is therefore linear $\Delta\theta_{\text{crit}} \sim \Delta x$, as seen in fig. 4.11 [8].

4.3 Trapping the particle

The presence of a shield introduces potential challenges to the stability of the particle trap. Levitated particles are typically trapped and cooled in ultra-high vacuum using magnetic, optical, or electrical radiofrequency Paul traps [30]. These traps differ in the trapping mechanism, but if the particle is cooled close to the ground state, all trapping potentials can be considered "harmonic" with trapping frequency $\omega_{\text{trap}} = 2\pi \times f$. The strength of the trapping potential $V \propto f^2$ varies across trap types, with frequencies typically ranging from $1\,\text{Hz} - 1\,\text{kHz}$ for magnetic traps [55] up to $10\,\text{kHz} - 300\,\text{kHz}$ for optical traps [30].

If the particle is positioned close to the shield, the Casimir interaction may destabilize the trap or pull the particle onto the shield. The total potential $V_{\text{tot}} = V_{\text{trap}} + V_{\text{Casimir}}$ is shown in fig. 4.12 for stable and unstable configurations. The attractive Casimir force shifts the equilibrium trap position closer to the shield by Δx given by

$$\Delta x = \frac{|-\nabla V_{\text{Casimir}}|}{m(2\pi f)^2} = \frac{2\hbar c \pi^3}{720} \left(\frac{\varepsilon_r - 1}{\varepsilon_r + 1}\right) \varphi(\varepsilon_r) \frac{R}{\mathscr{L}^3} \frac{1}{m(2\pi f)^2} \tag{4.21}$$

For $f = 1\,\text{kHz}$ and $L = 2R = 20\,\mu\text{m}$, this shift is negligibly small, as it is in the order of $\Delta x \approx 10^{-13}\,\text{m}$.

To determine the stability of a trapped particle with mass $M \propto R^3$ in a trap with frequency f placed at a distance $L_0 > R$ in front of the shield, the number of bound energy-eigenstates in the potential V_{tot} is considered. From fig. 4.12 it becomes clear, that as long as the particles thermal energy is well below E_0, the trap is stable and the particle is bound. Here, E_0 is defined as the local maximum of the potential

$$E_0 = \max_{L \in (R, L_0)} (V_{\text{trap}} + V_{\text{Casimir}}) \tag{4.22}$$

where L_0 is the position where the particle is trapped. If no local maximum exists, i.e.

$$\frac{\partial}{\partial L} (V_{\text{trap}} + V_{\text{Casimir}}) > 0 \tag{4.23}$$

for all $L \in (R, L_0)$, the trap is unstable. Regions of instability are shown in white in the stability diagram fig. 4.13. In the general case, the stability can be measured by computing the number of bound eigenstates $n(E \leq E_0)$ and comparing them with the number of thermally excited states $\bar{n}$. At a temperature T on average

$$\bar{n} = \frac{1}{e^{\beta\hbar\omega} - 1} \tag{4.24}$$

---

[8] Here it is shown in a double-logarithmic plot. The relation between Δx and $\Delta\theta_{\text{crit}}$ is nevertheless linear, which can be seen with similar arguments as used previously.
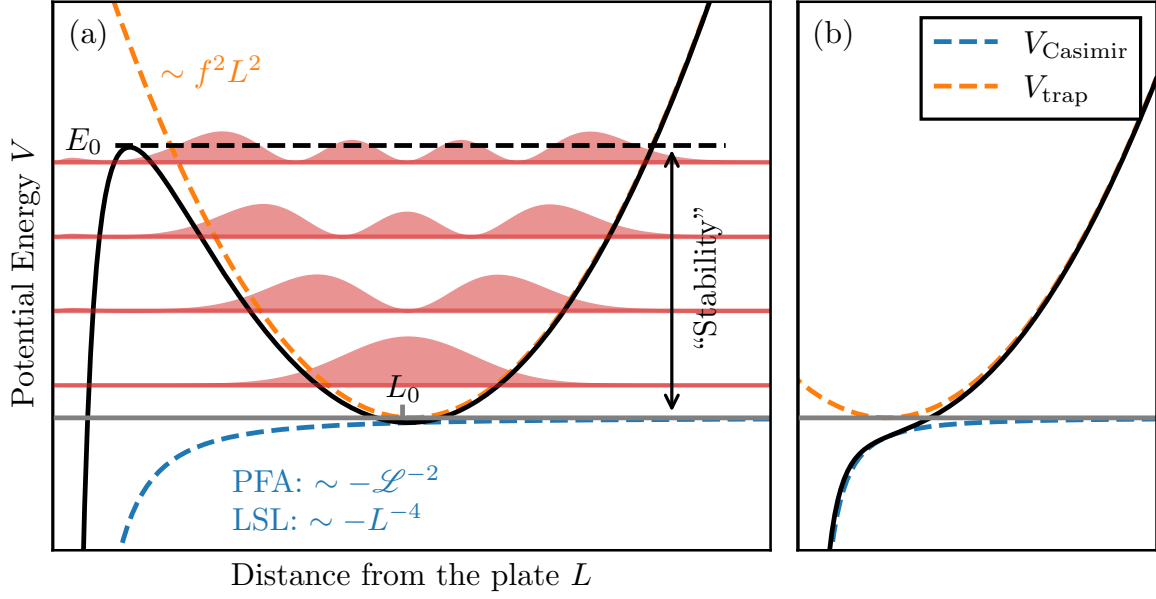
Figure 4.12: Visualization of the potential as an overlay of the harmonic trapping potential $V_{\text{trap}} = m(2\pi f)^2 L^2/2$ and the casimir potential V_{Casimir}. f is the trapping frequency and L_0 the position of the trap. In red, eigenstates of the potential are visualized offset by the eigen-energies. **(a)** Almost harmonic bounded potential which can hold the particle, if its energy is less than E_0. **(b)** Potential with no bounded states. Here, trapping is not possible.

states are occupied, where $\beta = 1/k_B T$ and $\omega = 2\pi f$. This is true, as long as the potential is assumed to be harmonic, which is, as seen shortly, a good approximation. To find the number of possible bound energy-eigenstates in the potential, the **WKB-approximation** is used. In this approximation, the energy of the n-th eigenstate of a smooth and appropriately slow varying potential $V(x)$ can be calculated using [56, p. 163]

$$\int_{x_1}^{x_2} \mathrm{d}x \sqrt{2m(E - V(x))} = \left(n + \frac{1}{2}\right) \pi \hbar, \tag{4.25}$$

where $V(x_1) = V(x_2) = E$ are two turning points corresponding to energy E. Conversely, it is possible to use this approximation to numerically estimate the total number of bound states in the potential $V = V_{\text{trap}} + V_{\text{Casimir}}$ using

$$n(E_0) \approx \frac{1}{\hbar \pi} \int_{x_1}^{x_2} \mathrm{d}x \sqrt{2m(E_0 - V(x))}, \tag{4.26}$$

which is closely given (highest deviation around 40%; averaged relative error $\sim 0.9\%$) by the harmonic approximation $n(E_0) \sim E_0/\hbar\omega$. The resulting number of bound states is shown in fig. 4.13 as well as the stability boundaries at specific temperatures where $\bar{n} = n(E_0)$. In these calculations, tunneling effects between through the potential boundary at E_0 are neglected which should not influence the results much considering the large number of bound eigenstates. It turns out, that regardless the type of the trap, a successful trapping even at room temperature should be possible as long as the particle is placed appropriately far away from the trap. The ability to trap and levitate the masses is therefore not significantly impaired by the presence of the Faraday shield.

4.4 Discussions

The preceding results highlight, that the proposed Faraday shield in experiments on measuring gravitationally induced entanglement entail significant engineering challenges, particularly due to the strict accuracy requirements for particle placement. Variations must be minimized to a precision of approximately $\Delta L \simeq 10^{-10}\,\mathrm{m}$ and $\Delta\theta \simeq 10^{-9}\,\mathrm{rad}$, which are extremely stringent. Adjustments to the experimental parameters in table 4.1 have to be made, where especially the separation distance L or the orientation are easy to change.

The parallel configuration is very stable against variations in the distance and might therefore be favorable (see in fig. 4.8). The separation L can be freely chosen and larger distances reduces the effect of placement variations as seen in fig. 4.9 but substantially increases the required coherence time $t_{\text{max}} \propto L^3$.

It could also be argued that at a distance of $L \geq 100\,\mu\mathrm{m} = 10R$ (compare to section 2.3), the Faraday shield would no longer be required because the Casimir forces are approximately ten times weaker than gravitational interactions. However, the loss
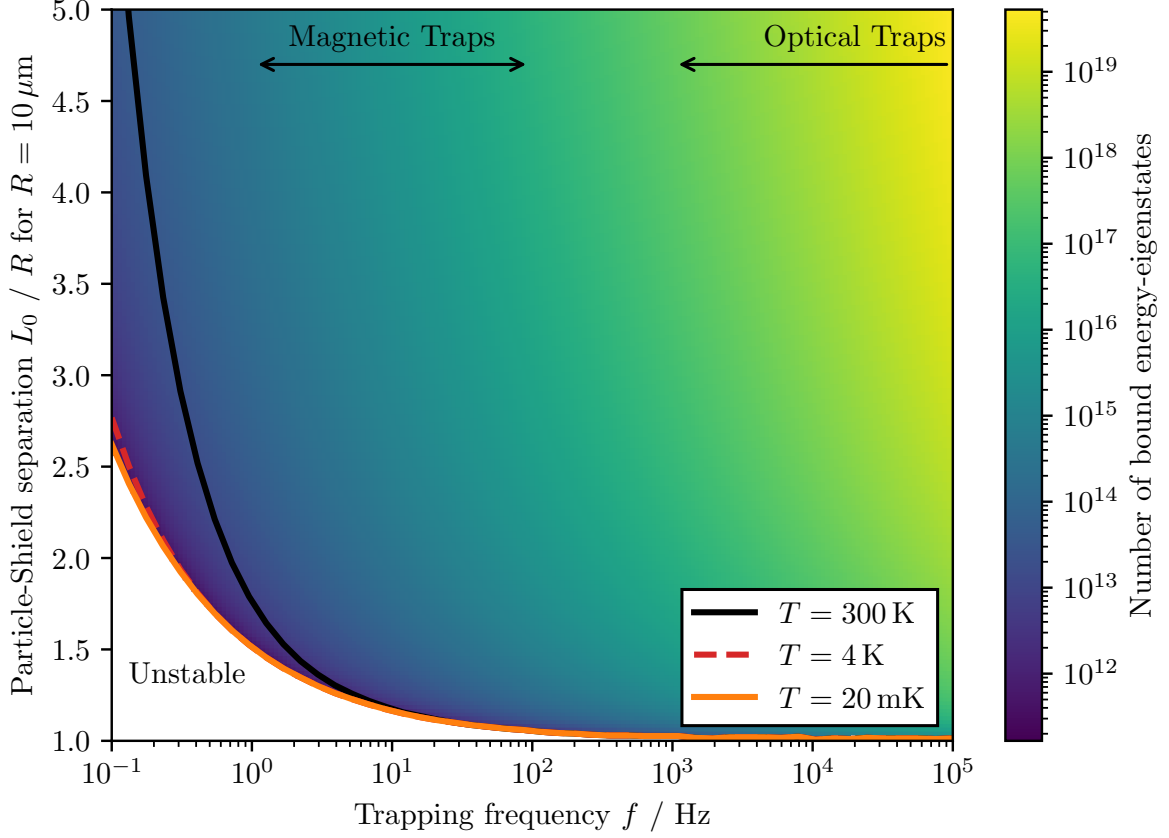
Figure 4.13: Stability diagram for different trapping frequencies $f = \omega/2\pi$ and particle-shield separations L_0. The number of bound energy-eigenstates for each combination of f and L_0 are calculated using the WKB-approximation. The number of thermally occupied states $\bar{n}$ at different Temperatures is overlaid. As an example, for $f = 1\,\mathrm{Hz}$, $\bar{n}(T = 300\,\mathrm{K}) \approx 10^{13}$ states are thermally occupied. All regions below these boundaries are unstable. A increase in the radius R and thus the mass M improves the regions of stability massively.

of entanglement due to angular and distance variations is not purely due to the Casimir forces between the particle and the shield. The gravitational coupling also depends on the placement, so that a complete removal of the shield does not fully eliminate the placement accuracy. Without the shield and by gravitational interaction alone, the critical variations are given by $\Delta\theta_{\text{crit, ideal}} = 1.1 \times 10^{-3}\,\text{rad}$ and $\Delta L_{\text{crit, ideal}} = 7 \times 10^{-4}\,\text{m}$, which should not pose an engineering problem.

Other parameters, such as particle size and superposition size, may not be easily adjustable without increasing the complexity of quantum control. Furthermore, particle trapping and levitation is not a limiting factor, as stable trapping is achievable for various configurations (section 4.3).

A primary aim of this thesis is to assess whether the Faraday shield allows particles to be brought closer together to enhance gravitational entanglement and reduce coherence times. Using the previous results, a optimal experimental parameter space can be determined. The optimization-goal can be expressed as the following:

One wants to get *as much entanglement as possible* in the *shortest time possible* while allowing for the *largest uncertainties* in thestate preparation and considering the limitations in the particles mass as well as in the superposition size.

Without specific constraints, a general optimization is impossible because (if the mass M and the superposition size Δx is fixed) coherence time $t \propto L^3$ (eq. (4.16)) and critical angular variation $\Delta\theta_{\text{crit}} \propto (L - R)^3/L^3$ (for small separations) or $\Delta\theta_{\text{crit}} \propto L^2$ (for $L \gg R$) cannot be optimized simultaneously. With constraints such as target coherence time t_{target} and/or a minimum placement accuracy, the required sphere-plate separation L as well as maximum measurable entanglement can be determined using the following steps:

1. Lets assume that the size of the particle R and consequently the mass $M = 4/3\pi R^3 \rho_{\text{Silica}}$ as well as the superposition size Δx are fixed. An increase in either of them would have a positive effect of the optimization goal stated above, as the time t_{max} decreases and the stability against placement variations increases simultaneously.

2. The following ratio given by the entanglement rate eq. (4.16)

$$\frac{M^2(\Delta x)^2}{L^3}t_{\text{max}} = \frac{8\pi\hbar}{G} \approx 4 \times 10^{-23}\,\text{kg}^2\text{s/m} \tag{4.27}$$

   is fixed [29]. In orthogonal configurations, this constant would reduce by a factor of $1/2$.

3. In general it is possible to measure at a earlier time $t_{\text{target}} = \tau t_{\text{max}}$ (i.e. the coherence time) with $\tau \leq 1$, where less entanglement has been generated but a larger stability against placement variations can be tolerated (see fig. 4.3). Putting all assumptions together, the ratio

$$\frac{t_{\text{target}}}{\tau L^3} = \frac{8\pi\hbar}{G}\frac{1}{M^2(\Delta x)^2} = \text{const.} \tag{4.28}$$

of measurement time and particle-shield separation is constant.

4. In the parallel orientation, the distance variations don't matter as the system is very stable against variations in the particle-shield separation. The critical angular variation however scales like $\Delta\theta_{\mathrm{crit}} \sim (L - R)^3/L^3$ for small distances and like $\Delta\theta_{\mathrm{crit}} \sim L^2$ at larger distances as shown in fig. 4.9. It is therefore possible to determine the minimum separation $L_{\min} > R$ for a given placement accuracy.

5. Using the required separation, one can calculate $\tau \in (0, 1]$ using eq. (4.28) and look up the maximal possible entanglement in fig. 4.3 after an evolution time $\tau t_{\max}$.

As an example, the radius is fixed as $R = 10\,\mu\mathrm{m}$ and the superposition size is $\Delta x = 100\,\mathrm{nm}$. Let's say that such a particle can be placed with an accuracy of $\Delta\theta = 5 \times 10^{-8}\,\mathrm{rad}$ and a coherence time of $1\,\mathrm{s}$ is reachable. Using the steps outlined above, the required minimum particle-shield separation is around $L \approx 8R$ and the maximal amount of measurable entanglement is given by $E_N \approx 6.0 \times 10^{-2}$. For more entanglement, either a heavier particle, a larger superposition size, a higher placement accuracy or larger coherence times are required. It is therefore possible, to bring the particles closer together than without the Faraday shield and still measure entanglement. One is only limited by the placement accuracy and repeatability.

5 The consequences of a thermal shield

The primary goal of the Faraday shield is to enable closer particle separations than would be possible without it, thereby enhancing gravitational interaction and reducing the required coherence times. This limit of $L \lesssim 100\,\mu$m has been discussed in section 2.3. Until now, the shield's dynamics and properties have been neglected. However, at non-zero temperatures, thermal vibrations of the shield could significantly affect entanglement generation. In this chapter, first an estimates of the required shield size is given followed by examining the impact of thermal vibrations for both large and small shields on entanglement generation. In the experiment, the trapped particles are cooled to their motional ground state to enable effective quantum control and the generation of spatial superpositions. Liquid helium at $T \approx 4\,$K is commonly used for cooling but cryogenic dilution refrigerators can cool small setups down to temperatures as low as $T \approx 20\,$mK [57]. These temperatures serve as reference points for the relevant calculations.

5.1 Thickness and size of the shield

The thickness d and the radius r_s of the spherical shield can be estimated by considering the properties of a real conductive material with high electrical conductivity σ. Even a superconducting shield could be considered for an almost perfect shielding of electromagnetic fields. For a shield, the transmission T of electromagnetic waves is given by [58]

$$T = \left| \frac{\mathbf{E}_{\text{after}}}{\mathbf{E}_{\text{before}}} \right| = \frac{2}{Z_0 \sigma d} \tag{5.1}$$

where $Z_0 = 377\,\Omega$ is the impedance of free space (assuming the shield is placed in a vacuum or in air). The electric conductivity σ is highly dependent on the temperature [59, p. 284-286], decreasing approximately as $1/T^5$ at low temperatures [9]. Copper offers a strong electric conductivity of $\sigma = 59.6 \times 10^6\,$S/m but this value increases significantly at cryogenic temperatures, with measured data showing $\sigma(T = 10) \approx 1.5 \times 10^{10}\,$S/m [60].

---

[9]This behavior is valid for temperatures below the Debye temperature ($\Theta_D = 343\,$K for copper). At the low temperatures used in the experiment, this model accurately describes the conductivity of metals [60].

To determine the shield's thickness, the primary criterion is that gravitational interactions should dominate the entanglement generation. Other mutual interactions between the particles, such as Coulomb or Casimir forces, must be sufficiently suppressed by the shield. The ***entanglement rate*** Γ quantifies the build-up of entanglement over time

$$\Gamma = \frac{\mathrm{d}}{\mathrm{d}t} E_N(\rho)\Big|_{t=0} \tag{5.2}$$

where E_N is an appropriate entanglement measure - in this case the logarithmic negativity [25] introduced in section 2.2. For gravitational interactions, the entanglement rate in the parallel orientation is given by using eq. (2.17) as

$$\Gamma_{\text{Gravity}} = \frac{G M_A M_B \Delta x_A \Delta x_B}{16 \hbar L^3 \log 2} = \frac{G \pi^2 R^6 \rho_{\text{Silica}}^2 (\Delta x)^2}{9 \hbar L^3 \log 2}. \tag{5.3}$$

where in the last step $M_A = M_B = 4/3 \pi R^3 \rho_{\text{Silica}}$ and $\Delta x_A = \Delta x_B \equiv \Delta x$ was used. The entanglement rate for non-gravitational interactions, such as Coulomb or Casimir forces, must be significantly smaller than the gravitational entanglement rate, ideally by a factor $\chi > 1$. This ensures that the measured entanglement is primarily due to gravitational interactions. In the following sections, estimations about the thickness and size of the shield are made, to effectively screen Coulomb and Casimir forces.

5.1.1 Shielding Coulomb-Interactions

The primary role of the Faraday shield is to block electromagnetic interactions between particles. Experimentally, it may be beneficial for the particles to carry a small amount of charge enabling the use of electrostatic traps with high trapping strength and large controllability [30]. The Coulomb interaction potential between the particles is given by

$$V = \frac{1}{4\pi\varepsilon_0} \frac{q_A q_B}{2L} \tag{5.4}$$

where $\varepsilon_0 = 8.8542 \times 10^{-12}\,\mathrm{A^2 s^4 m^{-3} kg^{-1}}$ is the permittivity of free space and $\left| q_{A(B)} \right| = e = 1.6022 \times 10^{-19}\,\mathrm{C}$ the charge of particle A and B respectively. This interaction mimics the form of the gravitational potential and can similarly induce entanglement with a entanglement rate identical as in eq. (5.3)

$$\Gamma_{\text{Coulomb}} = \frac{T \left| q_A q_B \right| (\Delta x)^2}{64\pi\varepsilon_0 \hbar L^3 \log 2}. \tag{5.5}$$

The shield suppresses the coupling by a factor of T. Requiring $\Gamma_{\text{Gravity}} > \chi \Gamma_{\text{Coulomb}}$, the minimum thickness of the shield can be calculated as

$$T \frac{\left| q_A q_B \right|}{64\pi\varepsilon_0} \times \chi < \frac{G \pi^2 R^6 \rho_{\text{Silica}}^2}{9} \tag{5.6}$$

$$\Longleftrightarrow \qquad d > \frac{9}{32} \frac{1}{Z_0 \sigma} \frac{1}{\pi^3 \varepsilon_0 G \rho_{\text{Silica}}^2} \frac{e^2}{R^6} \times \chi. \tag{5.7}$$

The thickness strongly depends on the particles size R, as large particles with large mass will favors gravitational entanglement generation. Assuming the particles are silica nano-spheres with parameters given in table 4.1, a minimum shield-thickness of $d \approx 10\,\text{nm} \times \chi$ at $4\,\text{K}$ and of $d \approx 2.5\,\mu\text{m} \times \chi$ at room temperature is required. At low temperatures, a realistic shield thickness could therefore be $d = 100\,\text{nm}$, balancing engineering practicality and electromagnetic suppression. Exact estimations however depend on the realization of the experiment as well as the precision in which the evolved state is measurable.

Electrostatic fields can still propagate around the finite-sized Faraday shield and potentially still induce entanglement. It is however possible to estimate the required shield radius r_s to block a specific amount η of the electric field (see appendix A.4):

$$\frac{r_s}{L} = \sqrt{\frac{1 - (1 - \eta)^2}{(1 - \eta)^2}} \tag{5.8}$$

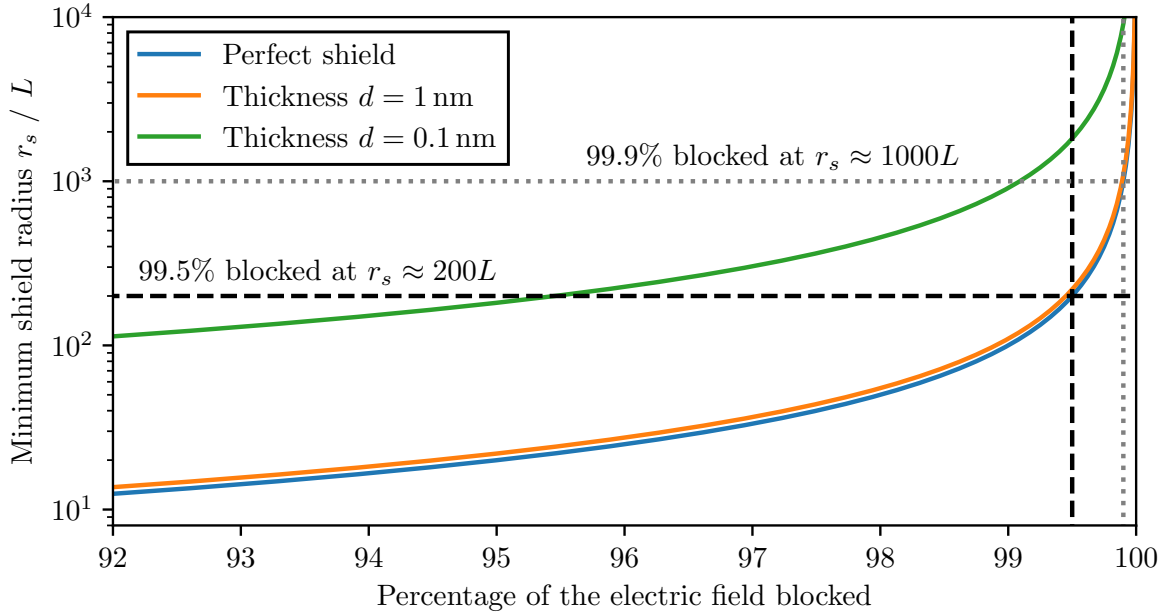The results are visualized in fig. 5.1. The shield's transmission T should therefore be

Figure 5.1: Shield radius as a function of the shielding effectiveness η for an ideal shield. Additionally, a real shield with varying thicknesses d is considered at $T = 300\,\text{K}$. To achieve shielding of $99.5 - 99.9\%$ ($\eta = 0.995 - 0.999$), a radius of $r_s = 200 - 1000L$ is needed.

modified to $\tilde{T} = T\eta + (1 - \eta)$, where the shield effectiveness η depends on r_s as given by eq. (5.8). Eq. (5.6) is modified, requiring a minimum effectiveness η_{min} for sufficient shielding:

$$\eta_{\text{min}} \approx 1 - \frac{64\pi^3 \varepsilon_0 G R^6 \rho_{\text{Silica}}^2}{9e^2}. \tag{5.9}$$

Using again the parameters from table 4.1, a minimum effectiveness of $\eta_{\min} \gtrsim 0.99997$ and thus a radius of $r_s \gtrsim 28000L \approx 60\,\mathrm{cm}$ is required. This shield is too large for all practical purposes and it might be beneficial to choose heavier masses ($\tilde{M} \sim 4M$) to reduce the shield size to the orders of $\sim 1\,\mathrm{cm}$. Due to practicality, a shield of $r_s = 1\,\mathrm{cm}$ is used in the following calculations. Using uncharged particles eliminates Coulomb interactions, and therefore reducing the shield's size to only shield Casimir interactions.

5.1.2 Shielding Casimir-Interactions

Similarly to Coulomb interactions, it is possible to to estimate the required thickness for a shield to sufficiently block Casimir interactions. The Casimir potential between the spheres with radius R separated by $2L$ is given by [44]

$$V = -\frac{23\hbar c}{4\pi \cdot 128L^7} \left(\frac{\varepsilon_r - 1}{\varepsilon_r + 2}\right)^2 R^6. \tag{5.10}$$

The corresponding entanglement rate is calculated similar to before by expanding the potential in small Δx and computing the logarithmic negativity:

$$\Gamma_{\mathrm{Casimir}} = T^2 \frac{161}{4096} \frac{cR^6(\Delta x)^2}{\pi L^9 \log 2} \left(\frac{\varepsilon_r - 1}{\varepsilon_r + 2}\right)^2. \tag{5.11}$$

The dependence on T^2 is only a systematic guess but should be sufficient for a basic estimation as Casimir and van der Waals forces are second order effects in the dipole-dipole interaction [34]. Requiring gravitational entanglement to dominate, $\Gamma_{\mathrm{Gravity}} > \chi\Gamma_{\mathrm{Casimir}}$, leads to

$$T^2 \frac{161cR^6}{4096\pi L^6} \left(\frac{\varepsilon_r - 1}{\varepsilon_r + 2}\right)^2 \times \chi < \frac{G\pi^2 \rho_{\mathrm{Silica}}^2 R^6}{9\hbar} \tag{5.12}$$

$$\Longleftrightarrow \qquad d > \sqrt{\frac{1449}{4096} \frac{c\hbar}{G\pi^3}} \frac{2}{Z_0 \sigma \rho L^3} \frac{\varepsilon_r - 1}{\varepsilon_r + 2} \times \sqrt{\chi}. \tag{5.13}$$

For large separations, the shield thickness can go arbitrarily low, as Casimir forces vanish. At separations $L \gtrsim 100\,\mu\mathrm{m}$, the shield might not be required at all (compare section 2.3). Assuming two identical silica nano-spheres with parameters given by table 4.1, the required minimum thickness is between $4 \times 10^{-11}\,\mathrm{m} \times \sqrt{\chi}$ at $4\,\mathrm{K}$ and $10\,\mathrm{nm} \times \sqrt{\chi}$ at room temperature. This is much thinner than what is required for shielding Coulomb interactions. The factor ε_r modifies the thickness by up to a factor of 1 and is therefore negligible in these calculations.

However, very thin shields lose mechanical rigidity, leading to enhanced vibrational excitations and potential instabilities. Vibrational frequency and thus the vibrational energy depends linearly on the shield's thickness, making thinner shields prone to large thermal vibrations. A detailed analysis of these effects is provided in the subsequent section.

5.1.3 Gravitational effects of the shield

The gravitational interaction between the masses and the shield is generally neglected because it has no significant impact on the entanglement generation between the particles. The only potential effect is indirect entanglement mediated by the thermal oscillations of the shield, as both masses couple gravitationally to it. However, as shown in section 5.3, this second-order effect is very weak and does not pose a problem, since it still represents gravitationally mediated entanglement - which is the focus of the experiment anyway. The gravitational force between a sphere with mass M and a infinitesimal mass segment $dm = rd\rho_{Cu}drd\varphi$ of the shield made of copper with density $\rho_{Cu} = 8960\,\mathrm{kg/m^3}$ at a distance r from the shield's center is given by

$$d\mathbf{F} = \frac{GMdm}{\ell}\hat{\boldsymbol{\ell}} \quad \Rightarrow \quad dF_z = \frac{GMr\rho_{Cu}d}{\ell^2}drd\varphi\cos\theta, \tag{5.14}$$

where $\ell^2 = r^2 + L^2$ denotes the distance between the sphere and the mass segment and $\theta = \arccos L/\ell$ is the angle between them. The total attractive force between the mass and the shield with radius r_s is therefore

$$F_z = GM\rho_{Cu}dL\int_0^{r_s}dr\int_0^{2\pi}d\varphi\,\frac{r}{(r^2 + L^2)^{3/2}} = 2\pi GM\rho_{Cu}d\left(1 - \frac{L}{\sqrt{L^2 + r_s^2}}\right). \tag{5.15}$$

For large shields $r_s \gg L$ this is independent of the particle-shield separation L. For a shield with thickness $d = 100\,\mathrm{nm}$ and the usual silica particle, the attraction force is around $F_{\mathrm{particle-shield}} \approx 4.1 \times 10^{-24}\,\mathrm{N}$ which is comparable with the attraction gravitational attraction force between the two particles themselves at $F_{\mathrm{particle-particle}} \approx 5.0 \times 10^{-24}\,\mathrm{N}$ but is much weaker than the Casimir attraction between the particle and the shield with $F_{\mathrm{Casimir}} \approx 1.4 \times 10^{-17}\,\mathrm{N}$. Therefore, the gravitational effect of the shield can be neglected in all practical calculations.

5.2 Thermal shield vibrations

A spherical plate of radius r_s clamped at its edge, can vibrate in distinct modes characterized by indices (k, l), where $k \in [1, \infty)$ and $l \in [0, \infty)$. The exact vibrational frequencies ω_{kl} and mode shapes u_{kl} are described by Bessel functions. In fact, one of the first occurrences of these functions is linked to Euler's study of vibrating perfectly flexible and infinitely thin membranes [61]. For a plate of a real material with density ρ and thickness d, vibrations are described the differential equation [62, p. 490]

$$D\nabla^2\nabla^2 u = -\rho d\ddot{u} \tag{5.16}$$

where D, a flexural rigidity constant, is dependent on material properties of the plate like Youngs module E and the Poisson ratio ν as

$$D = \frac{d^3 E}{12(1 - \nu^2)}. \tag{5.17}$$

The general solution of this differential equation is expressed terms of Bessel functions as (derived in Ref. [62, p. 490-495])

$$u_{kl}(r, \theta, t) = \left[J_l(\beta_k r) - \frac{J_l(\beta_k r_s)}{I_l(\beta_k r_s)} I_l(\beta_k r) \right] \cos(l\theta + \phi_1) \sin(\omega_{kl} t + \phi_2) \tag{5.18}$$

with

$$\beta_k = \frac{\tilde{r}_k}{r_s} \quad \text{and} \quad \omega_{kl} = \frac{\tilde{r}_k^2}{r_s^2} \sqrt{\frac{D}{\rho d}} = \tilde{r}_k^2 \frac{d}{r_s^2} \sqrt{\frac{E}{12\rho(1 - \nu^2)}}. \tag{5.19}$$

Here, $\tilde{r}_k$ is the k-th root of the equation

$$J_l(\tilde{r}_k) I_{l+1}(\tilde{r}_k) + I_l(\tilde{r}_k) J_{l+1}(\tilde{r}_k) = 0. \tag{5.20}$$

The phases ϕ_1 and ϕ_2 are determined by initial conditions and represent rotational and temporal offsets. The shape of the first 12 modes (k, l) are shown in fig. 5.2. In general, any possible vibration of the plates can be decomposed into a sum of these modes u_{kl}. The amplitude $\hat{z}$ depends on temperature T and is treated as a quantum harmonic oscillator with frequency ω_{kl}. The expectation value of the amplitude $\langle z\hat{z} \rangle$ is obviously zero and the variance $(\Delta \hat{z})^2 = \langle \hat{z}^2 \rangle - \langle \hat{z} \rangle^2$ at temperature T is given by (derivation in appendix A.5)

$$(\Delta \hat{z}_{kl})_T^2 = \frac{\hbar}{2\tilde{m}\omega_{kl}} \coth\left(\frac{\hbar\omega_{kl}}{2k_B T} \right) \approx \frac{k_B T}{\tilde{m}\omega_{kl}^2} \tag{5.21}$$

where $\hbar\omega \ll k_B T$ was used in the last step and $k_B = 1.3806 \times 10^{-23}$ J/K is the Boltzmann constant. The *effective mass* $\tilde{m}$ of the mode, considering the mode's shape, can intuitively be estimated by the average amplitude of the mode

$$\tilde{m} = m \frac{1}{\pi r_s^2} \int\limits_0^{r_s} \mathrm{d}r \int\limits_0^{2\pi} r\mathrm{d}\theta \, u_{kl}(r, \theta, t) \tag{5.22}$$

with $m = \rho\pi r_s^2 d$ being the total mass of the plate. The amplitude scales therefore as $\Delta z_{kl} \propto \omega^{-1}$ at high temperatures or for low frequencies.

The effect of infinite modes

For a shield with radius $r_s = 1$ cm $\gg R$ (referred to as the "large shield") and thickness $d = 100$ nmm made out of Copper with $E = 110$ GPa and $\nu = 1/3$, the vibrational frequencies for the first few modes are between 11.0 s^{-1} for $(1, 0)$ up to 1018 s^{-1} for $(7, 6)$. These low frequencies result in vibrational energies $\hbar\omega$ that are much smaller than the thermal energy $k_B T$ at any reasonable temperature. Consequently many vibrational modes are highly populated and even for temperatures of 10^{-6} K, the first 600 modes are equally populated with probabilities close to $1/Z$, where Z is the partition function

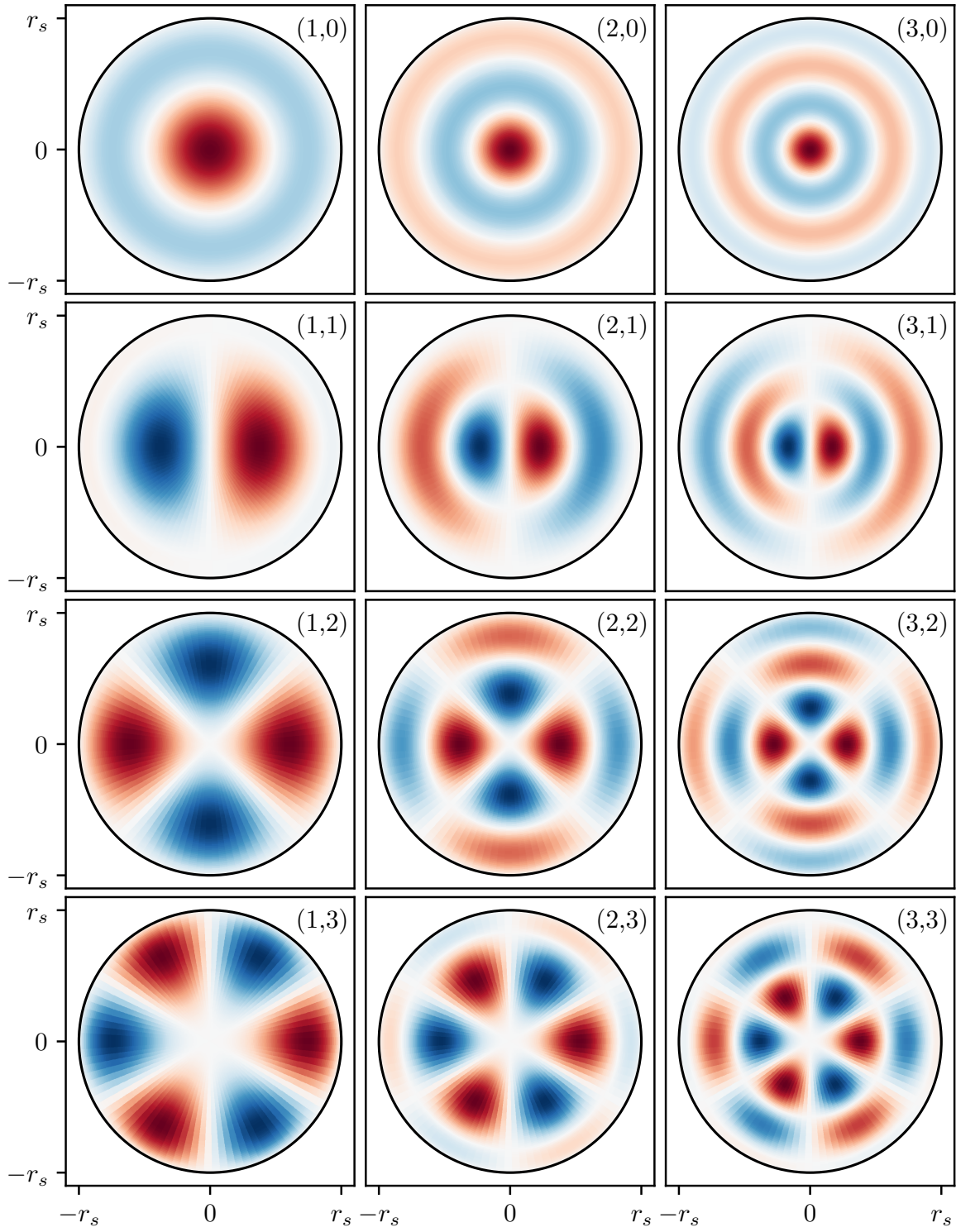$$Z = \sum_{m \in \{(k,l)\}} e^{-\beta\hbar\omega_m}. \tag{5.23}$$

Figure 5.2: Shape of the first 12 modes (k, l) ($k \geq 1$ and $l \geq 0$) of a vibrating spherical plate fixed at the edge with $r_s/d = 1000$.

It is possible to determine the asymptotic increase of frequencies ω_{kl} for high modes $k, l \to \infty$. Using the expansion of the Bessel functions for large arguments [63, eq. 10.17.3]

$$J_l(x) \sim \cos\left(x - \frac{l\pi}{2} - \frac{\pi}{4}\right) \quad \text{for } x \to \infty \tag{5.24}$$

and of the modified Bessel functions for $x \to \infty$ [63, eq. 10.40.1]

$$I_l(x) \sim \frac{e^x}{\sqrt{2\pi x}} \quad \text{for } x \to \infty \tag{5.25}$$

the asymptotic expansion of eq. (5.20) can be expressed as

$$\sim \frac{e^x}{\sqrt{2\pi x}} \left[\cos\left(x - \frac{l\pi}{2} - \frac{\pi}{4}\right) + \cos\left(x - \frac{l\pi}{2} - \frac{3\pi}{4}\right)\right] = 0. \tag{5.26}$$

For large $k \to \infty$, the zeros $\tilde{r}_k$ occur periodically. For large orders $l \to \infty$, the Bessel functions J_l scale like [63, eq. 10.19.1]

$$J_l(x) \sim \frac{1}{\sqrt{l}} \left(\frac{ex}{2l}\right)^l \quad \text{for } l \to \infty \tag{5.27}$$

implying that the first zero shift outwards with $\tilde{r}_1 \gtrsim 2l/e$. For high modes k and l this results in an linear asymptotic distribution of zeros and thus, the frequencies ω_{kl} scale in the order of $\mathcal{O}((k+l)^2)$.

Since the amplitude scales inversely with frequency $\Delta z_{kl} \propto 1/\omega_{kl}$, higher modes exhibit a quadratic decrease in amplitude. Additionally, the shape function u_{kl} of higher modes has more bulges, limiting the amplitude further as the available shield-material is distributed over smaller segments of the plate. These effects combine to ensure that higher-order modes have minimal contributions, allowing numerical calculations to focus on the first few modes. Nevertheless, the influence of infinitely many modes can still be approximated asymptotically using the scaling behavior of ω_{kl}.

It is also interesting to consider the scaling of the amplitudes Δz for shields with varying sizes r_s. According to eq. (5.19), the frequency ω increases quadratically as the shield radius r_s decreases. Simultaneously, the effective mass $\tilde{m}$ in eq. (5.22) scales also quadratically with the shield's size, consequently resulting in linear dependence of $\Delta z \sim r_s$ for large temperatures and/or low modes.

5.3 Entanglement in front of a thermal shield

The generation of entanglement between two particles depends heavily on variations in the placement of the particles and the shield, as seen in chapter 4. Shield vibrations can effectively be understood to alter the separation and angle of the cat-state relative to shield, as depicted in fig. 5.3. This approximation is only valid for shields significantly
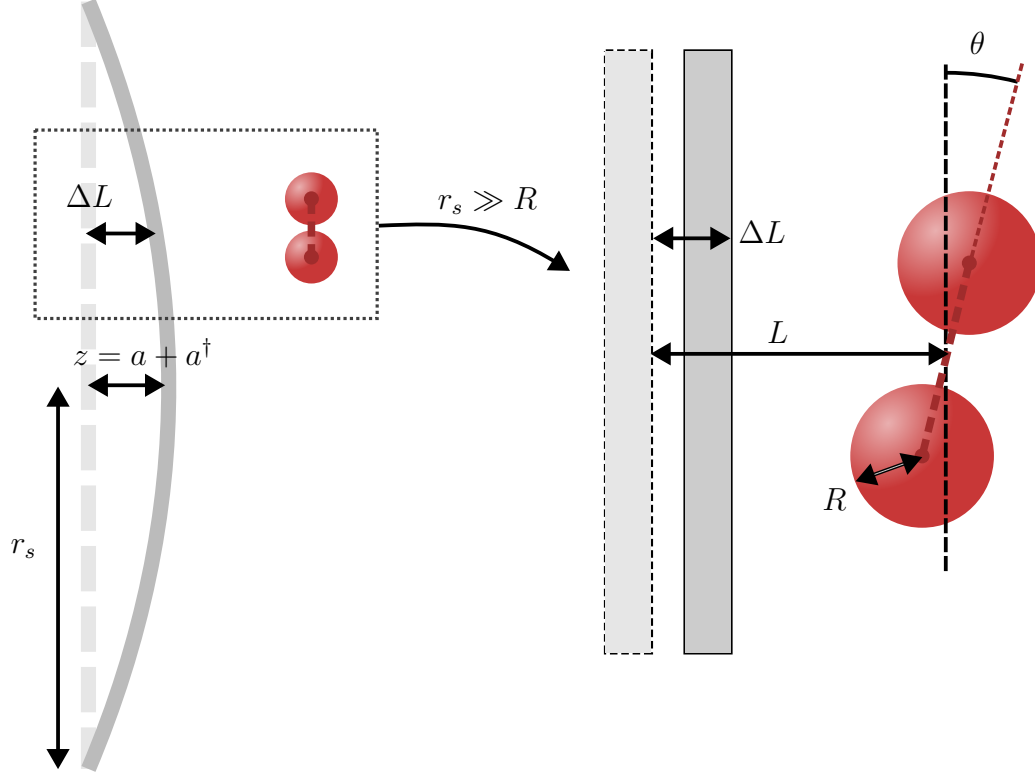
Figure 5.3: For a large ($r_s \gg R$) and locally linearizable shield, thermal vibrations with amplitude z can be interpreted as a static shield where particle A (shown in the figure) is positioned at $L + \Delta L$ with angle θ and particle B at $L - \Delta L$ with angle $-\theta$. Both variations depend solely on the vibrational amplitude. At low vibrational frequencies ($1/\omega \approx t_{\max}$), the amplitude remains nearly static during an experimental run, with thermal fluctuations distributed around $\langle z \rangle = 0$ and variance Δz given by eq. (5.21).

larger than the particle radius ($r_s \gg R$) and for low vibrational frequencies ($1/\omega \approx t_{\max}$), effectively capturing the impact of the first vibrational modes for small l and k. Especially the effect of the first mode $(1,0)$ can be put into the same framework from chapter 4. The interpretation is further supported by findings in section 3.3, showing that the Casimir interaction between a sphere and a tilted plane closely resembles that between a sphere and a flat plane. Contrary to the problem considered in chapter 4, here only the thermal amplitude z_{kl} is an independent random variable distributed around $\langle z_{kl} \rangle = 0$ with a standard deviation Δz_{kl} given by eq. (5.21). Variations in the particle-shield separation (ΔL) and angle (θ) are correlated to the vibration amplitude z. For a large and linearizable shield, this can be understood as

$$\theta = \arctan(z \, |\nabla u|) \approx z \, |\nabla u| \quad \text{and} \quad \Delta L = z \, |u| \tag{5.28}$$

where ∇u is the gradient of the vibrational mode's shape. Performing similar calculations to those in chapter 4, the averaged density matrix $\langle \rho \rangle$, dependent on Δz_{kl}, can be derived (see appendix B.3). The resulting entanglement, quantified by logarithmic negativity as a function of temperature T and particle-shield separation L, is given by eq. (B.28) and illustrated in fig. 5.4. At typical experimental temperatures, entanglement in the
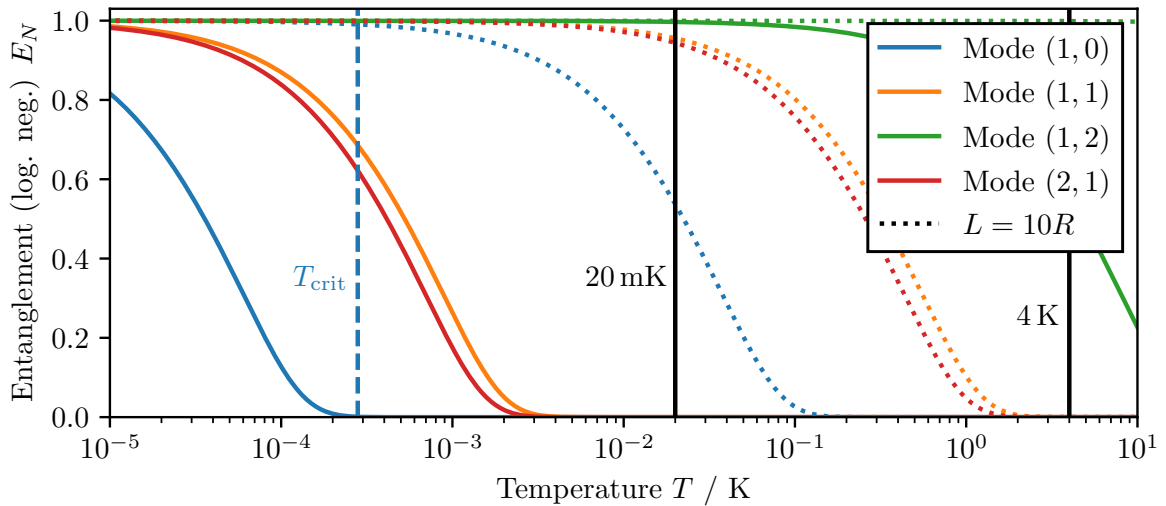

Figure 5.4: Entanglement between the particles (parallel orientation) near a thermal shield at different temperatures T for selected vibrational modes. At a critical temperature $T_{\mathrm{crit,kl}}$, entanglement is lost if mode (k, l) is present. This critical point shifts with greater particle-shield separations, following $T_{\mathrm{crit}} \propto L^4$.

presence of the mode $(1,0)$ is observable only at large particle-shield separations. In fact, the critical temperature T_{crit} scales with the separation L in the large-separation-limit (LSL) as:

$$T_{\mathrm{crit}} \sim (\Delta z_{\mathrm{crit}})^2 \sim \left(\frac{L^5}{t_{\max}} \right)^2 \sim L^4. \tag{5.29}$$

The large separations required are consistent with previous findings, considering that the thermal amplitudes $\Delta z_{1,0} \approx 9 \times 10^{-11}$ m at 20 mK are comparable with the critical values the variation in the shield-particle separation ΔL_{crit} in chapter 4. Interestingly, these results are unaffected by the shield radius r_s, as long as $r_s \gg R$ and the vibrational mode can be locally linearized. This invariance arises because the gradient $|\nabla u| \propto 1/r_s$ and $z \propto r_s$ perfectly cancel, leaving θ independent of r_s. When the cat state orientation is parallel to the shield, dependence on ΔL is negligible, leaving the entanglement independent of r_s. However, as seen in fig. 5.4, he mode number (k, l) significantly impacts entanglement generation. Higher modes correspond to higher vibrational frequencies and smaller amplitudes Δz, with T_{crit} asymptotically scaling as $\mathcal{O}((k + l)^2)$. This behavior is presented in fig. 5.5, where two positions of the particles in front of the plate is considered. If the particle is positioned exactly at the center of
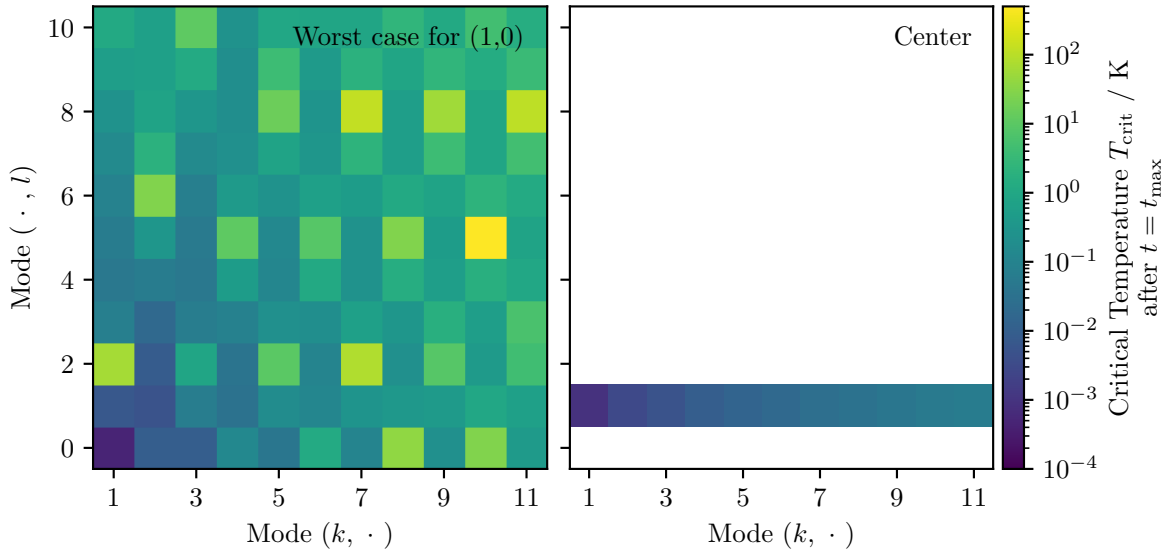

Figure 5.5: Critical temperature T_{crit}, at which no entanglement is measurable anymore for different modes at a separation of $L = 2R = 2\,\mu$m. The shape of the vibrational modes is considered. The particle is either placed at the position of the highest gradient of mode $(1, 0)$ (**left**) or in the center of the shield (**right**).

the shield, only specific mode shapes with $l = 2k + 1$, $k \in \mathbb{Z}$ can induce decoherence. For $l \neq 1$, this effect becomes however numerically negligible. If the particle is placed in the worst-case position for the first mode $(1, 0)$, which corresponds to the point of maximum gradient and thus the largest decoherence (approximately at $r \approx 0.0.527 r_s$), all modes are relevant. It becomes clear that only the first few modes significantly affect entanglement, as higher modes do not disrupt entanglement even at temperatures much higher than those required for entanglement loss.

This method on calculating the decoherence induced due to the thermal shield is only accurate in the specific cases of a large and slow vibrating shield ....

5.3.1 Analytic dynamics

The effect of the thermal shield on entanglement generation between the two delocalized particles can be calculated analytically. The Hamiltonian governing the interactions between the two particles with each other and with the thermal shield is given by

$$
\begin{aligned}
\hat{H} = \sum_{\substack{m\in\{(k,l)\} \\ k\geq 1,\ l\geq 0}} &\left\{ \hbar\omega_m \left(\hat{a}_m^\dagger \hat{a}_m + \frac{1}{2} \right) \right. \\
&+ g_{\text{A,m,Cas}}^{(1)}(\hat{a}_m + \hat{a}_m^\dagger)\left(\left| \psi_A^{(1)} \middle\rangle\!\middle\langle \psi_A^{(1)} \right| \otimes \mathbb{1} \right) + g_{\text{A,m,Cas}}^{(2)}(\hat{a}_m + \hat{a}_m^\dagger)\left(\left| \psi_A^{(2)} \middle\rangle\!\middle\langle \psi_A^{(2)} \right| \otimes \mathbb{1} \right) \\
&\left. + g_{\text{B,m,Cas}}^{(1)}(\hat{a}_m + \hat{a}_m^\dagger)\left(\mathbb{1} \otimes \left| \psi_B^{(1)} \middle\rangle\!\middle\langle \psi_B^{(1)} \right| \right) + g_{\text{B,m,Cas}}^{(2)}(\hat{a}_m + \hat{a}_m^\dagger)\left(\mathbb{1} \otimes \left| \psi_B^{(2)} \middle\rangle\!\middle\langle \psi_B^{(2)} \right| \right) \right\} \\
&+ g_{\text{Grav}}^{(1,1)} \left| \psi_A^{(1)}\psi_B^{(1)} \middle\rangle\!\middle\langle \psi_A^{(1)}\psi_B^{(1)} \right| + g_{\text{Grav}}^{(1,2)} \left| \psi_A^{(1)}\psi_B^{(2)} \middle\rangle\!\middle\langle \psi_A^{(1)}\psi_B^{(2)} \right| \\
&+ g_{\text{Grav}}^{(2,1)} \left| \psi_A^{(2)}\psi_B^{(1)} \middle\rangle\!\middle\langle \psi_A^{(2)}\psi_B^{(1)} \right| + g_{\text{Grav}}^{(2,2)} \left| \psi_A^{(2)}\psi_B^{(2)} \middle\rangle\!\middle\langle \psi_A^{(2)}\psi_B^{(2)} \right|
\end{aligned}
\tag{5.30}
$$

where the gravitational coupling

$$
g_{\text{Grav}}^{(ij)} = \frac{GM^2}{L^{(ij)}} \tag{5.31}
$$

between the states $\left| \psi_A^{(i)} \right\rangle$ and $\left| \psi_B^{(j)} \right\rangle$ $(i,j = 1,2)$ is determined by their separation $L^{(ij)}$ from eq. (4.10). The shield's thermal vibrations have no influence on this coupling, hence the solely gravitational interaction is the same as already discussed in chapter 4. Gravitational effects arising from the mass of the shield are omitted in these calculations because they are weaker by a factor of 10^7 compared to the Casimir interactions, as detailed in section 5.1.3.

The interaction between the state $\left| \psi_{A(B)}^{(i)} \right\rangle$ and the shield is described by

$$
\frac{\hbar c \pi^3}{720} \left(\frac{\varepsilon_r - 1}{\varepsilon_r + 1} \right) \varphi(\varepsilon_r) \frac{R}{(\mathscr{L} + \hat{z}_m u_m(r_{A(B)}^{(i)}))^2} \tag{5.32}
$$

which is dependent on the mode m and the mode shape $\hat{z}u_m$ at the position $r_{A(B)}^{(i)}$ where the cat-state is positioned in front of, where $\hat{z} = \sqrt{\hbar/2\tilde{m}\omega_m}(\hat{a}_m + \hat{a}_m^\dagger)$ is the amplitude of the vibration. Expanding the term in first order in $\hat{z}$ and ignoring the zeroth-order term which is constant and thus equal to a global phase at the end of the calculations, the Casimir coupling in the Hamiltonian eq. (5.30) is given by

$$
g_{\text{A(B),m,Cas}}^{(i)} = g_{\text{PFA}} \frac{2u_m(r_{A(B)}^{(i)})}{\mathscr{L}^3} \sqrt{\frac{\hbar}{2\tilde{m}\omega_m}} \quad \text{with} \quad g_{\text{PFA}} = \frac{\hbar c \pi^3 R}{720} \left(\frac{\varepsilon_r - 1}{\varepsilon_r + 1} \right) \varphi(\varepsilon_r). \tag{5.33}
$$

The combined system of the two particles $\rho_{\text{sys.}} \in \mathcal{H}_{\text{sys.}}$ and the thermal modes $\rho_{\text{th}} = \bigotimes_m \rho_{\text{th,m}} \in \mathcal{H}_{\text{th}}$ evolves under those interactions from the initial state $\rho_0 = \rho_{\text{th}} \otimes \rho_{\text{sys.}}$.

The initial state of the two particles $\rho_{\text{sys.}}$ is given by eq. (2.2) and $\rho_{\text{th,m}}$ is the thermal state of vibrational mode m, which can be represented either in the number basis $\{|n\rangle\}$ or in the coherent state basis $\{|\alpha\rangle\}$ as [64]

$$\rho_{\text{th,m}} = \frac{1}{Z} \sum_{n=1}^{\infty} e^{-\beta\hbar\omega_m(n+1/2)} |n\rangle\langle n| = \int d\alpha^2 \frac{1}{\pi\bar{n}} e^{-\frac{|\alpha|^2}{\bar{n}}} |\alpha\rangle\langle\alpha|. \tag{5.34}$$

Here, $Z = \text{tr}\, e^{-\beta\hbar\omega_m(\hat{n}+1/2)} = e^{-\beta\hbar\omega_m/2}/(1 - e^{-\beta\hbar\omega_m})$ is the partition function and $\bar{n} = 1/(e^{\beta\hbar\omega_m} - 1)$ is the average thermal occupation number of mode m at temperature T.

After time t, tracing out the thermal shield yields the evolved two-particle system

$$\rho_{\text{sys.}}(t) = \text{tr}_{\text{th}} \left(\hat{U}(t)\, \rho_0\, \hat{U}^\dagger(t) \right). \tag{5.35}$$

The time evolution is computed in appendix B.4 and is given by

$$\rho_{\text{system}}(t) = \frac{1}{4} \begin{pmatrix} 1 & e^{i\phi_{11,12}}e^{-\gamma_{11,12}} & e^{i\phi_{11,21}}e^{-\gamma_{11,21}} & e^{i\phi_{11,22}}e^{-\gamma_{11,22}} \\ & 1 & e^{i\phi_{12,21}}e^{-\gamma_{12,21}} & e^{i\phi_{12,22}}e^{-\gamma_{12,22}} \\ & & 1 & e^{i\phi_{21,22}}e^{-\gamma_{21,22}} \\ & & & 1 \end{pmatrix} \tag{5.36}$$

with the decoherence terms

$$\gamma_{ii',jj'} = \sum_m \frac{4}{\hbar^2\omega_m^2} \left| (g_{\text{A,m,Cas}}^{(i)} + g_{\text{B,m,Cas}}^{(i')}) - (g_{\text{A,m,Cas}}^{(j)} + g_{\text{B,m,Cas}}^{(j')}) \right|^2 \sin^2\left(\frac{\omega_m t}{2}\right) \left[\bar{n} + \frac{1}{2}\right] \tag{5.37}$$

and the phases (where the gravitational part is already given by eq. (2.7))

$$\phi_{ii',jj'} = \sum_m \frac{1}{\hbar} \left(g_{\text{Grav}}^{(ii')} - g_{\text{Grav}}^{(jj')} \right) t$$
$$+ \frac{\sin(\omega_m t) + \omega_m t}{\hbar^2\omega_m^2} \left[(g_{\text{A,m,Cas}}^{(i)} + g_{\text{B,m,Cas}}^{(i')})^2 - (g_{\text{A,m,Cas}}^{(j)} + g_{\text{B,m,Cas}}^{(j')})^2 \right]. \tag{5.38}$$

At $T = 0$, decoherence terms persist, but their effect is significant only for strong Casimir interactions (e.g., small separations $L \sim R$) The decoherence scales as $\gamma \propto \omega_m^{-4}$ from which the asymptotic dependence on the modes $\mathcal{O}((k+l)^{-8})$ follows. It is therefore possible to estimate the combined effect of the first N modes as

$$\sim \frac{1}{\zeta(8)} \sum_{n=1}^{N} \frac{1}{n^8} \tag{5.39}$$

where ζ is the Riemann zeta function, which converges very fast to 1, even for small N. At specific times $t = 2\pi k/\omega_m$, $k \in \mathbb{N}$ the decoherence from mode m vanishes, leading to entanglement values close to the ideal case, aligning with the findings in Ref. [65]. This periodic behavior is confirmed in fig. 5.6, showing a measurable amount of entanglement only close to these specific times. The full width at half maximum (FWHM) of these
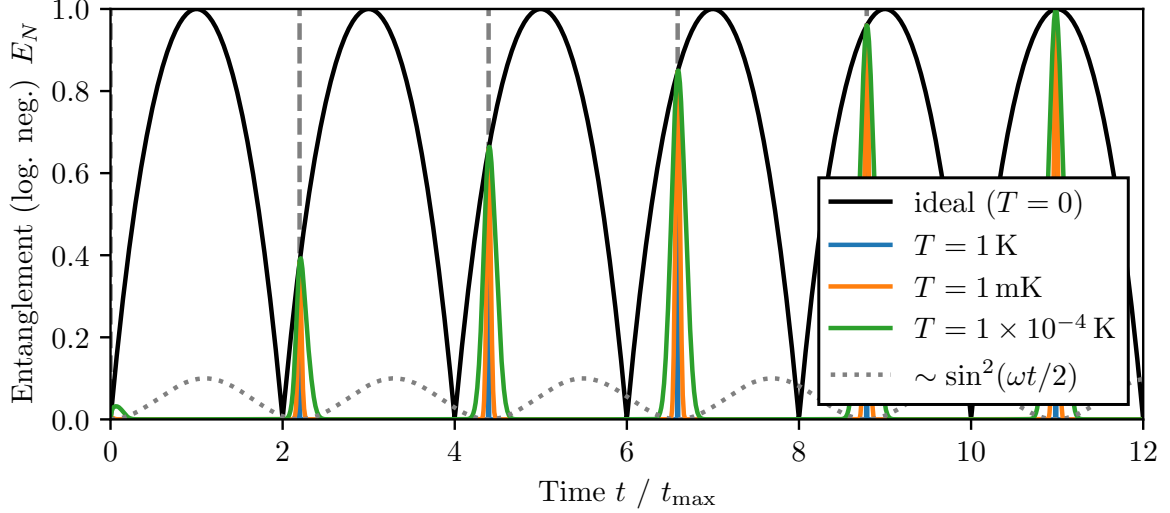
Figure 5.6: Entanglement dynamics in front of a thermal shield in mode $(1,0)$ at different temperatures. Only at specific times $2\pi k/\omega_{1,0} \approx k \times 576\,\text{ms}$, $k \in \mathbb{N}$, entanglement is observable. This aligns with the findings in Ref. [65]. The particle and shield parameters are taken from table 4.1.

observed peaks is approximated by

$$\text{FWHM} \approx \frac{4}{\omega}\sqrt{\frac{\log 2}{\gamma}} \propto \frac{1}{\sqrt{\bar{n}}}. \tag{5.40}$$

For high temperatures, entanglement is only measurable in a very short window around time $2\pi/\omega_m$.

The resulting decoherence of multiple modes is given by the sum of all individual modes, decaying rapidly with the mode number as seen in eq. (5.39). Ideal entanglement as without the shield is never achieved due to the quasi-periodicity of the system; the frequency ratios $\omega_i/\omega_j \notin \mathbb{Q}$ for $i \neq j$ [10] prevent exact repetition of the resulting sinusoidal summation. The entanglement dynamics of the first combined 50 vibrational modes numerically are shown in fig. 5.7 . This figure highlights the dominant contribution of the first mode $(1,0)$, with realistically measurable entanglement primarily occurring at $t = 2\pi/\omega_{1,0}$. Even for temperatures as low as $20\,\text{mK}$, entanglement remains minimal due to rapid decoherence - at least for small separations. Increasing the particle-shield separation reduces Casimir coupling $g_{\text{Cas}} \propto \mathscr{L}^{-3}$ and hence delaying decoherence but simultaneously slowing gravitational entanglement generation down ($t_{\max} \propto L^3$). The combined effect is therefore qualitatively given by $\gamma \propto g_{\text{Cas}}^2 \sin^2(t) \propto L^{-6} \sin^2(L^3) \xrightarrow{L \gg R} 0$. The dependence of the entanglement on the particle-shield separation at two specific points in time is shown in fig. 5.8.

---

[10]While not rigorously proven, this conclusion is supported by the transcendental nature of the zeros of the Bessel functions [66] and the non-integer frequency ratio $\omega_{1,0}/\omega_{1,1} \notin \mathbb{Z}$, which on its own should already ensure quasi-periodic behavior.
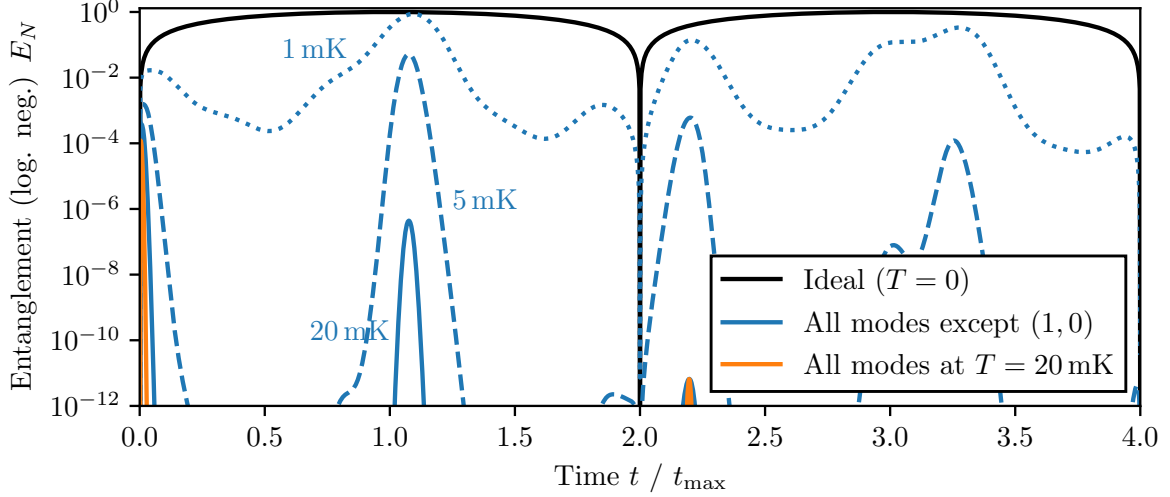
Figure 5.7: Entanglement dynamics in front of a thermal shield. **Orange**: The first 50 modes have been used in the numeric calculation. The effect of all remaining modes is around $1.7 \times 10^{-11}\,\%$. **Blue**: Results excluding the $(1,0)$ mode at varying temperatures ranging from $1\,\mathrm{mK}$ up to $20\,\mathrm{mK}$. The parameters for the particle and the shield are taken from table 4.1.

By measuring after time $t_{\max} \approx 259\,\mathrm{ms}$, in the ideal scenario without the shield, a maximally entangled state with $E_N = 1$ is observed. Although $2\pi/\omega_{1,0} = \mathrm{const.}$ is constant, $t_{\max}$ increases with L, creating specific separations (e.g. for $L \approx 2.6R$) where the two times align, enhancing observability. For even larger L, decoherence effects eq. (5.37) diminish, making entanglement measurable even at higher temperatures.

By measuring at the time $2\pi/\omega_{1,0} \approx 576\,\mathrm{ms}$ where the decoherence of the first mode (with the larges effect on total decoherence) almost vanishes, entanglement can be observed by increasing the particle-shield separation. However, measuring at a constant time independent of L limits the maximum of possibly reachable entanglement as the gravitational entanglement rate slows down and increasing $t_{\max}$.

The radius of the shield also has a large impact on entanglement generation. Smaller shields with larger mode frequencies result in a decreased and faster oscillating decoherence term $\gamma \propto \sin^2(\omega)1/\omega_m^2$. The time between the points, where the decoherence effect of the first mode almost vanishes (i.e. every $\Delta t = 2\pi/\omega_{1,0} \propto r_s^2$), decreases for smaller shields and thus making entanglement measurable more frequently at almost any point in time. Numeric calculations show, that even for shields as large as $r_s = 5\,\mathrm{mm}$, entanglement of around $E_N \lesssim 1$ can be measured at $T = 20\,\mathrm{mK}$ and even at close separations (see fig. C.1).

Examining the phases $\phi_{ii',jj'}$ in eq. (5.38) reveals that, similar to the gravitational force, the Casimir interaction between the particle and the shield can induce entanglement between the particles. This occurs as both particles couple to the shield via Casimir in-
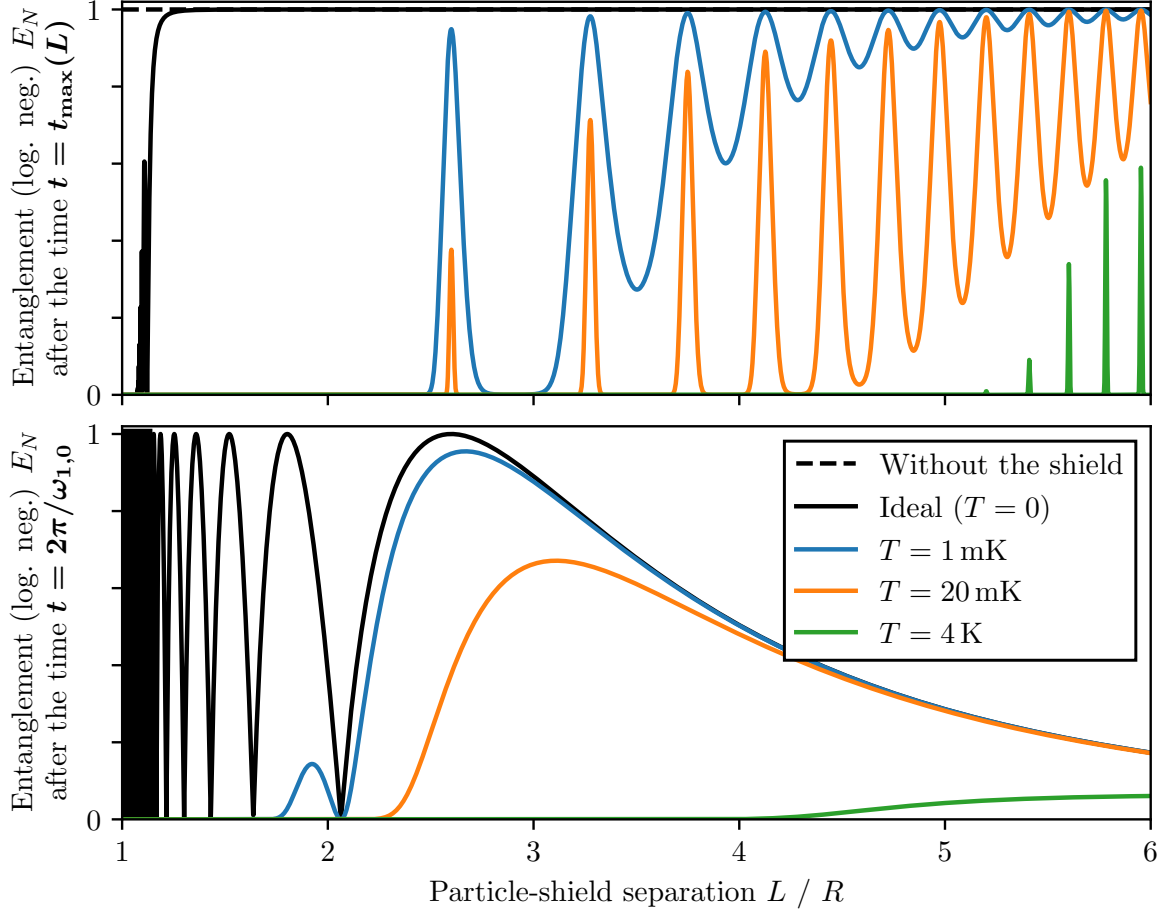
Figure 5.8: Entanglement at various particle-shield separations $L > R$ at time $t_{\max}(L)$ (eq. (4.16)) (**top**) and $t_2\pi/\omega_{1,0} \approx 576\,\text{ms}$ (**bottom**). Calculations use parameters from table 4.1 and are performed at different temperatures.

teractions, enabling indirect interaction between them. However, the resulting amount of entanglement is very small, as evident from the dependence on $1/\hbar^2$ in eq. (5.38). While negligible at larger separations, Casimir-induced indirect entanglement could become significant at very small distances where the Casimir forces are much stronger than the gravitational interaction. This is particularly relevant if the entanglement generated via Casimir interactions approaches that due to gravity. The relative strength can be estimated by comparing the term corresponding to the gravitational interaction with the Casimir terms in eq. (5.38):

$$g_{\text{Grav}} t \gtrsim \frac{\sin(\omega_m t) + \omega_m t}{\hbar \omega_m^2} g_{\text{Cas}}^2 \tag{5.41}$$

$$\implies \quad \frac{GM^2}{2L} \gtrsim g_{\text{PFA}} \frac{1}{\mathscr{L}^3} \sqrt{\frac{\hbar}{2\tilde{m}\omega_m}} \tag{5.42}$$

where $\langle \sin(\omega t) \rangle = 0$ was averaged. Using the parameters for the particles and the shield from table 4.1, the lower bound for the separation is given by $L > 1.29 \times 10^{-5}\,\text{m} \approx 1.3R$. For separations $L \gtrsim 2.7R$, gravitational entanglement becomes 100 times stronger than that due to Casimir interactions. These separations are most likely fulfilled either way considering the results from the previous chapters. Thus, indirect entanglement from Casimir forces can be neglected for larger separations.

5.3.2 Small shields

A small shield only can block the direct Casimir interactions between the particles A and B, hence it can only be used if no other forms of electromagnetic interactions between the particles such as Coulomb coupling are present. For very small shields in the size of the particles $r_s \sim R + \Delta x/2$, the above considerations are not fully applicable, as they assume the linearization of the vibrational mode at the particle scale. The vibrations of the shield and the resulting vibrational modes substantially alter the Casimir potential, which is no longer determined solely by the interaction between a perfectly flat shield and a spherical particle. For a small shield, deformations can no longer be approximated locally as a flat, tilted plate; instead, the precise shape of the vibrational mode must be accounted for. As discussed in section 3.3, deformations, such as those resembling the first vibrational mode, significantly impact the resulting Casimir potential which is, in the proximity-force approximation, upper bounded by an interaction equivalent to that between a sphere and a plate with separation $\mathscr{L} \pm \Delta z$.

In the temporal domain, vibrational frequencies scale quadratically with the shield size, $\omega \propto 1/r_s^2$, which results in the measuring process being multiple times longer than a single vibrational period. Consequently, Casimir interactions are effectively averaged, leading to an effectively planar and flat shield. This agrees with the findings in the previous section and the results shown in fig. C.1, where smaller shields exhibit drastically reduced decoherence effects.

Similar reasoning applies to higher vibrational modes in arbitrarily large shields. These modes, characterized by high frequencies and a roughly uniform distribution of deformations, effectively average out the Casimir interactions in the temporal domain as well as because of the findings in section 3.3, preserving entanglement.

5.4 Discussions of the effects of the thermal shield

In this chapter, two different strategies to calculate the effect of a thermal shield at temperature T on the entanglement generation have been considered.

The naive approach described in section 5.3 assumes the shield to be locally flat and static over the measurement time. Vibrational amplitudes z_{kl} are treated statically and normally distributed over multiple measurements with each mode inducing random phase shifts, similar to the placement variations considered in chapter 4. This approach greatly overestimates the dynamics by assuming maximal effects from all vibrational modes occur simultaneously. In reality however, different modes might cancel themselves partially out reducing the overall total deformation. Furthermore this approximation is only valid for large and thus linearizbale shields ($r_s \gg R$) and low vibrating frequencies $\omega_{kl} \approx t_{\max}$.

The second method calculates analytically the particles entanglement by solving the Hamiltonian dynamics for small amplitude $\Delta z \ll L$. This method provides a more accurate depiction of the time-dependent system and reveals that entanglement can partially recover even for small separations and large shields at specific times, notably at $2\pi/\omega_{1,0}$.

The effects of the thermal shield can be mitigated by reducing the decoherence effects via the following methods:

Lowering the shield's temperature Reducing the temperature of the setup and the shield decreases vibrational amplitudes and the associated decoherence. Temperatures around $4\,\mathrm{K}$ are desirable as they are experimentally accessible using liquid helium cooling. Temperatures as low as $20\,\mathrm{mK}$ are theoretically reachable by $^3\mathrm{He}/^4\mathrm{He}$ dilution refrigerators [57, 67]. All cooling mechanisms however induce additional vibrational noise due to their mechanical components and additional studies about the effect of such noise has to be considered.

Increasing the particle-shield separation Larger separations reduce the relative effect of the vibrations as $\Delta z/L \to 0$. In the naive approach section 5.3, separations of at least $L \gtrsim 10R$ are required making the shield almost unnecessary, as for similar separations, the Casimir interactions between both particles are smaller than the gravitational interaction (see discussion in section 2.3). The presence of the shield could even potentially worsen the entanglement generation. In the more detailed and analytical method in section 5.3.1, separations of around $5R$ are possible, but requiring measurement at very precise points in time.

Reducing the shield's radius Decreasing r_s does increase the vibrational frequencies quadratically ($\omega_{kl} \propto 1/r_s^2$) and simultaneously decreases the amplitudes $\Delta z_{kl} \sim r_s$. The results in the naive approach are independent of the shields radius. However, for small shields with large frequencies, this method is applicable. The analytical approach on the other hand shows a strong dependence on the shield's radius r_s where halving the radius nearly restores entanglement for small separations (see fig. C.1). A reduction in r_s is however only possible for uncharged, neutral particles that do not interact via a direct Coulomb interaction, necessitating magnetic or optical trapping methods.

By combining these approaches, the thermal shield's impact can be mitigated, creating better conditions for entanglement generation. Measurements might be possible only at specific and precise points in time, particularly at $2\pi/\omega_{kl}$ with fluctuations limited to approximately $\Delta t \sim 1/\sqrt{\bar{n}} \approx \sqrt{\omega_{1,0}/T}$. Achieving accurate measurements at arbitrary times would require either lower temperatures or larger particle-shield separations, as suggested by the results of the naive method in section 5.3.

For very small shields, which are only considerable for uncharged particles that can solely couple through mutual Casimir interactions, the Casimir forces cannot be simplified to a sphere interacting with a perfectly flat plate. Instead, mode shapes must be taken into account, slightly modifying the interaction. Although challenging to estimate, the rapid frequency increase to $2\pi/\omega \ll t_{\max}$ during the measurement period suggests that shield vibrations would average out over time. Thus, uncharged particles and therefore small shields are greatly preferable.

Improvements on the rigidity of the shield can also be considered. Reinforcing the shield, for instance with a cross structure of thicker material, could reduce vibration frequencies of the shield by effectively reducing the size and increasing the overall thickness. Alternative shield designs, such as a star shape, might also be beneficial by potentially offering more uniformly distributed and higher-frequency vibrations. For rectangular plates, frequency increases are marginal, scaling by $\omega_{kl} = (k^2 + l^2)/(2r_s)^2 \sqrt{D\pi^4/\rho d}$ [62, p. 471-474] and thus improving entanglement generation only at most up to a constant.

6 Discussion and outlook

Testing the quantum nature of gravity is notoriously difficult due to its relative weakness compared to the other fundamental forces. The concept of gravitationally induced entanglement as evidence for the non-classicality of gravity was first proposed by Feynman at the 1957 Chapel Hill Conference. Since then, several experimental proposals have emerged [3, 6], all aiming on measuring entanglement between macroscopic delocalized masses after direct gravitational coupling. A common approach to prevent electromagnetic interactions such as Coulomb or Casimir forces, involves placing a conductive Faraday shield between the particles [31].

In this work, it was shown by calculating the relative dynamical phase build-up, that Casimir interactions between two macroscopic Schrödinger-cat states and a conducting Faraday shield can destroy all measurable entanglement if small stochastic variations in the initial setup or thermal motion of the shield are present. Placement accuracies in the initialization of the cat-states should stay below a threshold, depending on the achievable magnitudes in superposition size and particle masses, usually well below $\Delta\theta \lesssim 10^{-8}\,\text{rad}$ and $\Delta L \lesssim 10^{-9}\,\text{m}$. To mitigate the decoherence effects of the thermal shield, measurements at very precise points in time are required, where the particular effects of the first vibrational mode minimize.

The calculated bounds for the placement parameters and the measurement accuracy appears to be very difficult or even practically impossible to implement experimentally in near future. In general, the entanglement generation can be improved by increasing either the particles superposition size, its mass or by choosing lager particle-shield separations, which reduces the relative effect of the variations in the placement as well as decoherence effects of the thermal shield. The primary goal of the Faraday shield is to allow for tighter particle separations as the gravitational coupling is no longer dominated by the inter-particle Casimir forces. This is however only partially possible under specific circumstances, as established in this work, as certain setups would perform better without the shield. In section 4.4 a schema for choosing the optimal parameters is presented, given known experimental constraints in the preparation of the delocalized Schrödinger-cat states and in the placement accuracy. By choosing the shield as small as possible and temperatures as low as physically reachable, thermal decoherence weakens, improving entanglement generation. Uncharged particles - requiring a much smaller shield in the size of the silica-nanospheres - are therefore preferable over charged particles.

For a more precise characterization of the experimental challenges, squeezed gaussian states [68, p. 33-64] should be considered in addition to Schrödinger-cat-like states.

Most experimental realizations of spatial superpositions of massive objects, especially in the world of high mass levitated particles, are going to be ideally close to squeezed gaussian states [29, Timestamp: 23:00] as they can be naturally prepared by ground state cooling in a harmonic trap [69]. However, the findings in Ref. [14] suggest that the results derived from cat-states should remain largely applicable.

Other forms of decoherence, such as undamped vibrations of the setup - potentially due to complex cooling mechanisms like dilution refrigerators - and black-body radiation of the particles can also be considered. It is possible to estimate the decoherence due to thermal radiation [70, p. 127-136] between the cat-states as well as with the thermal environment at temperature T as [71]

$$\Gamma_{\text{decoh., black-body}} \propto 1 - \exp\left\{-\frac{(\Delta x)^2}{\lambda_{\text{th}}^2}\right\} \sim (\Delta x)^2 \tag{6.1}$$

where $\lambda_{\text{th}} = \pi^{2/3}\hbar c/k_B T$ is the thermal wavelength with values of $\lambda_{\text{th}} \approx 1\,\text{mm}$ at $4\,\text{K}$. For $\Delta x \ll \lambda_{\text{th}}$, the decoherence scales quadratically in Δx, resulting in a similar increase as the gravitational entanglement rate Γ_{Gravity} from eq. (5.3). For very large superposition sizes, decoherence stays constant resulting in a domination of gravitational entanglement generation. Other forms of decoherence like collisions with air molecules can similarly be considered and thus a maximal vacuum pressure can be estimated.

Analogous to variations in the initial particle placement for each run, variations in other parameters, such as the measurement time (i.e. the time of gravitational interaction between the states) can be examined. A brief investigation of this effect was presented in Ref. [47], showing results consistent with those obtained in this thesis.

Another avenue worth looking into with potentially large experimental improvements lies in the enhancement of the results by knowing the exact initial placement of each separate run - or at least a skewed probability distribution of the parameters. The decoherence effects in the average measurement can then be corrected for during the data analysis step. This would allow for greater tolerance of variations in the initial setup.

The findings in this thesis have broader implications beyond gravitationally induced entanglement, as a new method for the precise measurement of Casimir forces can be developed utilizing spatial delocalizations. The idea of using levitated particles for observing Casimir interactions is a current research topic [72]. By positioning a single Schrödinger-cat superposition state close to a large thermally vibrating plate, dephasing effects similar to the ones discussed in section 5.3.1 are expected due to the slightly different interactions of each superposition component with the plate. Measuring this dephasing offers a way to determine the Casimir coupling strength between arbitrarily shaped objects and a flat plane with high precision. Moreover, this approach could be extended to measure Casimir-Polder interactions between atoms or molecules and a plane. Current technologies, as demonstrated in matter-wave experiments [18], could be sufficient even today. Experimental setups designated for gravitational entanglement sensing can be adapted for these measurements, providing a new and precise tool for

testing modern theories of Casimir interactions.

In essence, this thesis offers an overview and an estimation of previously overlooked experimental issues with proposed experiments on quantum gravity. By addressing these problems, this work partially paves the way for the possible experimental realization of measuring gravitationally induced entanglement, which ultimately advances the quest for a grand unifying theory of quantum gravity.

Bibliography

[1] N. Maskelyne, "A proposal for measuring the attraction of some hill in this kingdom by astronomical observations", Philosophical Transactions of the Royal Society of London **65**, 495–499 (1775) `10.1098/rstl.1775.0049`.

[2] R. D. Davies, "A Commemoration of Maskelyne at Schiehallion", Quarterly Journal of the Royal Astronomical Society **26**, 289–294 (1985).

[3] T. Krisnanda, G. Y. Tham, M. Paternostro, and T. Paterek, "Observable quantum entanglement due to gravity", npj Quantum Information **6**, `10.1038/s41534-020-0243-y` (2019) `10.1038/s41534-020-0243-y`, arXiv:1906.08808.

[4] H. Chevalier, A. J. Paige, and M. S. Kim, "Witnessing the nonclassical nature of gravity in the presence of unknown interactions", Physical Review A **102**, 022428 (2020) `10.1103/physreva.102.022428`, arXiv:2005.13922.

[5] J. S. Pedernales, G. W. Morley, and M. B. Plenio, "Motional Dynamical Decoupling for Matter-Wave Interferometry", Phy. Rev. Lett. **125**, 023602 (2019) `10.1103/physrevlett.125.023602`, arXiv:1906.00835.

[6] S. Bose, A. Mazumdar, G. W. Morley, H. Ulbricht, M. Toroš, M. Paternostro, A. Geraci, P. Barker, M. S. Kim, and G. Milburn, "A Spin Entanglement Witness for Quantum Gravity", Phys. Rev. Lett. **119**, 240401 (2017) `10.1103/physrevlett.119.240401`, arXiv:1707.06050.

[7] C. Overstreet, P. Asenbaum, J. Curti, M. Kim, and M. A. Kasevich, "Observation of a gravitational Aharonov-Bohm effect", Science **375**, 226–229 (2022) `10.1126/science.abl7152`.

[8] R. Colella, A. W. Overhauser, and S. A. Werner, "Observation of Gravitationally Induced Quantum Interference", Physical Review Letters **34**, 1472–1474 (1975) `10.1103/physrevlett.34.1472`.

[9] L. Lami, J. S. Pedernales, and M. B. Plenio, "Testing the quantum nature of gravity without entanglement", Phys. Rev. X **14**, 021022 (2023) `10.1103/physrevx.14.021022`, arXiv:2302.03075.

[10] R. Horodecki, P. Horodecki, M. Horodecki, and K. Horodecki, "Quantum entanglement", Rev. Mod. Phys. **81**, 865–942 (2007) `10.1103/revmodphys.81.865`, arXiv:`quant-ph/0702225`.

[11] M. B. Plenio and S. Virmani, "An introduction to entanglement measures", Quantum Information & Computation **7**, 1–51 (2005), arXiv:`quant-ph/0504163`.

[12] M. J. W. Hall and M. Reginatto, "On two recent proposals for witnessing non-classical gravity", Journal of Physics A: Mathematical and Theoretical **51**, 085303 (2017) `10.1088/1751-8121/aaa734`, arXiv:1707.07974.

[13] D. Rickles and C. M. DeWitt, ***The Role of Gravitation in Physics: Report from the 1957 Chapel Hill Conference***, en (Max-Planck-Gesellschaft zur Förderung der Wissenschaften, Berlin, Feb. 2011), `10.34663/9783945561294-00`.

[14] J. S. Pedernales and M. B. Plenio, "On the origin of force sensitivity in tests of quantum gravity with delocalised mechanical systems", Contemporary Physics **64**, 147–163 (2023) `10.1080/00107514.2023.2286074`, arXiv:2311.04745.

[15] M. Reginatto and M. J. W. Hall, "Entangling quantum fields via a classical gravitational interaction", Journal of Physics: Conference Series **1275**, 012039 (2019) `10.1088/1742-6596/1275/1/012039`, arXiv:1809.04989 [gr-qc].

[16] D. Carney, P. C. E. Stamp, and J. M. Taylor, "Tabletop experiments for quantum gravity: a user's manual", Classical and Quantum Gravity **36**, 034001 (2018) `10.1088/1361-6382/aaf9ca`, arXiv:1807.11494.

[17] M. Christodoulou, A. Di Biagio, M. Aspelmeyer, Č. Brukner, C. Rovelli, and R. Howl, "Locally mediated entanglement in linearised quantum gravity", Physical Review Letters **130**, 100202 (2022) `10.1103/physrevlett.130.100202`, arXiv:2202.03368.

[18] Y. Y. Fein, P. Geyer, P. Zwick, F. Kiałka, S. Pedalino, M. Mayor, S. Gerlich, and M. Arndt, "Quantum superposition of molecules beyond 25 kDa", Nature Physics **15**, 1242–1245 (2019) `10.1038/s41567-019-0663-9`.

[19] T. Westphal, H. Hepach, J. Pfaff, and M. Aspelmeyer, "Measurement of Gravitational Coupling between Millimeter-Sized Masses", Nature **591**, 225–228 (2021) `10.1038/s41586-021-03250-7`, arXiv:2009.09546.

[20] C. Marletto and V. Vedral, "Gravitationally Induced Entanglement between Two Massive Particles is Sufficient Evidence of Quantum Effects in Gravity", Physical Review Letters **119**, 240402 (2017) `10.1103/physrevlett.119.240402`, arXiv:1707.06036.

[21] H. B. G. Casimir, "On the attraction between two perfectly conducting plates", Proc. Kon. Ned. Akad. Wet. **51**, 793 (1948).

[22] H. B. G. Casimir and D. Polder, "The Influence of Retardation on the London-van der Waals Forces", Physical Review **73**, 360–372 (1948) `10.1103/physrev.73.360`.

[23] L. Gurvits, "Classical deterministic complexity of Edmonds' problem and Quantum Entanglement", in Proceedings of the thirty-fifth annual acm symposium on theory of computing, Vol. 4, STOC03 (June 2003), pages 10–19, `10.1145/780542.780545`, arXiv:quant-ph/0303055.

[24] G. Vidal and R. F. Werner, "A computable measure of entanglement", Phys. Rev. A **65**, 032314 (2001) `10.1103/physreva.65.032314`, arXiv:quant-ph/0102117.

[25] M. Plenio, "Logarithmic negativity: a full entanglement monotone that is not convex.", Physical Review Letters **95**, 090503 (2005) `10.1103/PhysRevLett.95.090503`, arXiv:`quant-ph/0505071`.

[26] A. D. O'Connell, M. Hofheinz, M. Ansmann, R. C. Bialczak, M. Lenander, E. Lucero, M. Neeley, D. Sank, H. Wang, M. Weides, J. Wenner, J. M. Martinis, and A. N. Cleland, "Quantum ground state and single-phonon control of a mechanical resonator", Nature **464**, 697–703 (2010) `10.1038/nature08967`.

[27] R. L. DeBiase, "Are Casimir Forces Conservative?", Physics Procedia **38**, 18–33 (2012) `10.1016/j.phpro.2012.08.008`.

[28] B. Yi, U. Sinha, D. Home, A. Mazumdar, and S. Bose, "Massive spatial qubits: Testing macroscopic nonclassicality and Casimir entanglement", Physical Review Research **5**, 033202 (2023) `10.1103/physrevresearch.5.033202`, arXiv:`2106.11906`.

[29] M. Aspelmeyer, ***Quantum sources of gravity: the next frontier of macrosopic quantum physics***, `https://www.youtube.com/watch?v=0AVDrVY-rTw`, Timestamp: 51:00, May 2024.

[30] C. Gonzalez-Ballestero, M. Aspelmeyer, L. Novotny, R. Quidant, and O. Romero-Isart, "Levitodynamics: levitation and control of microscopic objects in vacuum", Science **374**, `10.1126/science.abg3027` (2021) `10.1126/science.abg3027`, arXiv:`2111.05215`.

[31] T. W. van de Kamp, R. J. Marshman, S. Bose, and A. Mazumdar, "Quantum Gravity Witness via Entanglement of Masses: Casimir Screening", Phys. Rev. A **102**, 062807 (2020) `10.1103/physreva.102.062807`, arXiv:`2006.06931`.

[32] H. Rudolph, U. Delić, M. Aspelmeyer, K. Hornberger, and B. A. Stickler, "Force-Gradient Sensing and Entanglement via Feedback Cooling of Interacting Nanoparticles", Physical Review Letters **129**, 193602 (2022) `10.1103/physrevlett.129.193602`, arXiv:`2204.13684 [quant-ph]`.

[33] F. London, "Zur Theorie und Systematik der Molekularkräfte", Zeitschrift für Physik **63**, 245–279 (1930) `10.1007/bf01421741`.

[34] M. Bordag, U. Mohideen, and V. M. Mostepanenko, "New developments in the Casimir effect", Physics Reports **353**, 1–205 (2001) `10.1016/s0370-1573(01)00015-1`, arXiv:`quant-ph/0106045 [quant-ph]`.

[35] G. L. Klimchitskaya, U. Mohideen, and V. M. Mostepanenko, "The Casimir force between real materials: Experiment and theory", Reviews of Modern Physics **81**, 1827–1885 (2009) `10.1103/revmodphys.81.1827`, arXiv:`0902.4022`.

[36] S. K. Lamoreaux, "The Casimir force: background, experiments, and applications", Reports on Progress in Physics **68**, 201–236 (2004) `10.1088/0034-4885/68/1/r04`.

[37] M. Bordag, "Proceedings of the Fourth Workshop on Quantum Field Theory under the Influence of External Conditions", in The Casimir Effect 50 Years Later (June 1999), pages 1–410, `10.1142/9789814527576`.

[38] T. H. Boyer, "Quantum Electromagnetic Zero-Point Energy of a Conducting Spherical Shell and the Casimir Model for a Charged Particle", Physical Review **174**, 1764–1776 (1968) `10.1103/physrev.174.1764`.

[39] L. H. Ford, "Casimir Force between a Dielectric Sphere and a Wall: A Model for Amplification of Vacuum Fluctuations", Phys. Rev. A **58**, 4279–4286 (1998) `10.1103/physreva.58.4279`, arXiv:`quant-ph/9804055`.

[40] E. M. Lifshitz, "The theory of molecular attractive forces between solids", Sov. Phys. JETP **2**, 73–83 (1956) `10.1016/b978-0-08-036364-6.50031-4`.

[41] M. Hartmann, "Casimir effect in the plane-spheregeometry: Beyond the proximityforce approximation", PhD thesis (Universität Augsburg, July 2018).

[42] T. Emig, "Fluctuation induced quantum interactions between compact objects and a plane mirror", Journal of Statistical Mechanics: Theory and Experiment **2008**, P04007 (2007) `10.1088/1742-5468/2008/04/p04007`, arXiv:`0712.2199`.

[43] A. Bulgac, P. Magierski, and A. Wirzba, "Scalar Casimir effect between Dirichlet spheres or a plate and a sphere", Physical Review D **73**, 025007 (2006) `10.1103/physrevd.73.025007`.

[44] T. Emig, N. Graham, R. L. Jaffe, and M. Kardar, "Casimir forces between arbitrary compact objects", Phys. Rev. Lett. **99**, 170403 (2007) `10.1103/physrevlett.99.170403`, arXiv:`0707.1862`.

[45] I. G. Pirozhenko and M. Bordag, "On the Casimir repulsion in sphere-plate geometry", Physical Review D **87**, 085031 (2013) `10.1103/physrevd.87.085031`, arXiv:`1302.5290`.

[46] K. Perlin, "An image synthesizer", SIGGRAPH Comput. Graph. **19**, 287–296 (1985) `10.1145/325165.325247`.

[47] H. C. Nguyen and F. Bernards, "Entanglement dynamics of two mesoscopic objects with gravitational interaction", The European Physical Journal D **74**, `10.1140/epjd/e2020-10077-8` (2020) `10.1140/epjd/e2020-10077-8`, arXiv:`1906.11184`.

[48] K. F. Riley, ***Mathematical methods for physics and engineering***, edited by M. P. Hobson and S. J. Bence, Third edition, Hier auch später erschienene, unveränderte Nachdrucke (Cambridge University Press, Cambridge, 2018), 1333 pages.

[49] A. C. Berry, "The accuracy of the Gaussian approximation to the sum of independent variates", Transactions of the American Mathematical Society **49**, 122–136 (1941) `10.1090/s0002-9947-1941-0003498-3`.

[50] S. Rijavec, M. Carlesso, A. Bassi, V. Vedral, and C. Marletto, "Decoherence effects in non-classicality tests of gravity", New Journal of Physics **23**, 043040 (2020) `10.1088/1367-2630/abf3eb`, arXiv:`2012.06230`.

[51] M. Bild, M. Fadel, Y. Yang, U. von Lüpke, P. Martin, A. Bruno, and Y. Chu, "Schrödinger cat states of a 16-microgram mechanical oscillator", Science **380**, 274–278 (2022) `10.1126/science.adf7553`, arXiv:2211.00449.

[52] K. C. Lee, M. R. Sprague, B. J. Sussman, J. Nunn, N. K. Langford, X.-M. Jin, T. Champion, P. Michelberger, K. F. Reim, D. England, D. Jaksch, and I. A. Walmsley, "Entangling Macroscopic Diamonds at Room Temperature", Science **334**, 1253–1256 (2011) `10.1126/science.1211914`.

[53] C. Whittle, E. D. Hall, S. Dwyer, and et al., "Approaching the motional ground state of a 10-kg object", Science **372**, 1333–1336 (2021) `10.1126/science.abh2634`, arXiv:2102.12665.

[54] D. Grass, J. Fesel, S. G. Hofer, N. Kiesel, and M. Aspelmeyer, "Optical trapping and control of nanoparticles inside evacuated hollow core photonic crystal fibers", Applied Physics Letters **108**, `10.1063/1.4953025` (2016) `10.1063/1.4953025`, arXiv:1603.09393.

[55] B. R. Slezak, C. W. Lewandowski, J.-F. Hsu, and B. D'Urso, "Cooling the motion of a silica microsphere in a magneto-gravitational trap in ultra-high vacuum", New Journal of Physics **20**, 063028 (2018) `10.1088/1367-2630/aacac1`, arXiv:1802.03424 [quant-ph].

[56] W. P. Schleich, "Waves à la WKB", in **Quantum Optics in Phase Space** (John Wiley & Sons, Ltd, Berlin, Feb. 2001) Chap. 5, pages 153–169.

[57] H. Zu, W. Dai, and A. T. A. M. de Waele, "Development of dilution refrigerators - A review", Cryogenics **121**, 103390 (2022) `10.1016/j.cryogenics.2021.103390`.

[58] G. A. E. Vandenbosch, "The basic concepts determining electromagnetic shielding", American Journal of Physics **90**, 672–681 (2022) `10.1119/5.0087295`.

[59] R. Gross and A. Marx, **Festkörperphysik**, 3., akt. Aufl, De Gruyter Studium (De Gruyter, Berlin, 2018), 11066 pages.

[60] R. Berman, D. K. C. Macdonald, and F. E. Simon, "The thermal and electrical conductivity of copper at low temperatures", Proceedings of the Royal Society of London. Series A. Mathematical and Physical Sciences **211**, 122–128 (1952) `10.1098/rspa.1952.0029`.

[61] J. Dutka, "On the Early History of Bessel Functions", Archive for History of Exact Sciences **49**, 105–134 (1995).

[62] S. S. Rao, **Vibration of Continuous Systems**, 2nd Edition (Wiley, Jan. 2019), `10.1002/9781119424284`.

[63] F. W. J. Olver, A. B. Olde Daalhuis, D. W. Lozier, B. I. Schneider, R. F. Boisvert, C. W. Clark, B. R. Miller, B. V. Saunders, H. S. Cohl, M. A. McClain, and eds., **NIST Digital Library of Mathematical Functions**, `https://dlmf.nist.gov/`, Release 1.2.2 of 2024-09-15, 2024.

[64] M. O. E. Steiner, J. S. Pedernales, and M. B. Plenio, "Pentacene-Doped Naphthalene for Levitated Optomechanics", `10.48550/ARXIV.2405.13869` (2024) `10.48550/ARXIV.2405.13869`, arXiv:2405.13869 [`quant-ph`].

[65] J. S. Pedernales, K. Streltsov, and M. B. Plenio, "Enhancing Gravitational Interaction between Quantum Systems by a Massive Mediator", Physical Review Letters **128**, 110401 (2021) `10.1103/physrevlett.128.110401`, arXiv:2104.14524.

[66] L. Lorch and M. E. Muldoon, "Transcendentality of zeros of higher dereivatives of functions involving Bessel functions", International Journal of Mathematics and Mathematical Sciences **18**, 551–560 (1995) `10.1155/s0161171295000706`.

[67] P. Das, R. B. de Ouboter, and K. W. Taconis, "A Realization of a London-Clarke-Mendoza Type Refrigerator", in Ninth international conference on low-temperature physics (1965), pages 1253–1255, `10.1007/978-1-4899-6443-4_133`.

[68] A. Serafini, ***Quantum Continuous Variables: A Primer of Theoretical Methods***, 1st ed. (CRC Press, July 2017), `10.1201/9781315118727`.

[69] T. Weiss, M. Roda-Llordes, E. Torrontegui, M. Aspelmeyer, and O. Romero-Isart, "Large Quantum Delocalization of a Levitated Nanoparticle Using Optimal Control: Applications for Force Sensing and Entangling via Weak Forces", Physical Review Letters **127**, 023601 (2020) `10.1103/physrevlett.127.023601`, arXiv:2012.12260.

[70] M. Schlosshauer, ***Decoherence and the Quantum-To-Classical Transition***, 1st edition (Springer, Berlin, Heidelberg, July 2007), `10.1007/978-3-540-35775-9`.

[71] O. Romero-Isart, "Quantum superposition of massive objects and collapse models", Physical Review A **84**, 052121 (2011) `10.1103/physreva.84.052121`, arXiv:1110.4495.

[72] Z. Xu, P. Ju, K. Shen, Y. Jin, Z. Jacob, and T. Li, "Observation of non-contact Casimir friction", `10.48550/ARXIV.2403.06051` (2024) `10.48550/ARXIV.2403.06051`, arXiv:2403.06051.

[73] M. A. Nielsen and I. L. Chuang, ***Quantum computation and quantum information***, 10th anniversary ed. (Cambridge University Press, Cambridge, 2010), 1676 pages.

[74] D. J. Griffiths, ***Elektrodynamik, Eine Einführung***, edited by U. Schollwöck, 4th edition (Pearson, Hallbergmoos, 2018), 1711 pages.

[75] S. Blanes, F. Casas, J. A. Oteo, and J. Ros, "The Magnus expansion and some of its applications", Physics Reports **470**, 151–238 (2008) `10.1016/j.physrep.2008.11.001`, arXiv:0810.5488 [`math-ph`].

A Ancillary calculations

A.1 Evolution under a gravitational Hamiltonian

In this section the time evolution of a system under Hamiltonian eq. (2.1) is calculated for two particles A and B (mass m) separated by L in a harmonic trap (frequency ω). A example from Ref. [16] is followed. The total Hamiltonian describing the dynamics is given by

$$\hat{H} = \sum_{i=A,B} \frac{\hat{p}_i}{2m} + \frac{1}{2}m\omega^2\hat{x}_i^2 + \hat{H}_G \tag{A.1}$$

where $\hat{x}$ and $\hat{p}$ are the position and momentum operators of the particle satisfying the canonical commutator relation $[\hat{x}_i, \hat{p}_j] = i\hbar\delta_{ij}$. Introducing ladder operators $\hat{x}_i = \sqrt{\hbar/2m\omega}\left(\hat{a}_i^\dagger + \hat{a}_i\right)$, $\hat{p}_i = \sqrt{\hbar m\omega/2}\left(\hat{a}_i^\dagger - \hat{a}_i\right)$, the Hamiltonian can be rewritten:

$$\hat{H} = \sum_{i=A,B} \hbar\omega\hat{a}_i^\dagger\hat{a}_i - \frac{Gm^2}{L^3}\left(\sqrt{\frac{\hbar}{2m\omega}}\right)^2 \left(\hat{a}_A\hat{a}_B + \hat{a}_A\hat{a}_B^\dagger + \hat{a}_A^\dagger\hat{a}_B + \hat{a}_A^\dagger\hat{a}_B^\dagger\right). \tag{A.2}$$

Applying the rotating wave approximation, the term $\hat{a}_A\hat{a}_B + \hat{a}_A^\dagger\hat{a}_B^\dagger$ can be dropped. The effective Hamiltonian is therefore in the form

$$\hat{H}_{\text{eff}} = \sum_{i=A,B} \hbar\omega\hat{a}_i^\dagger\hat{a}_i - \hbar g\left(\hat{a}_A\hat{a}_B^\dagger + \hat{a}_A^\dagger\hat{a}_B\right) \tag{A.3}$$

with coupling strength $g = Gm/\omega L^3$. A general biparty Fock state $|\psi_0\rangle = |kl\rangle$ with $k, l \in \mathbb{N}_0$ can be evolved in time under this hamiltonian, treating the gravitational interaction $H_G = -\hbar g(\hat{a}_1\hat{a}_2^\dagger + \hat{a}_1^\dagger\hat{a}_2)$ as a perturbation. The resulting state $|\psi(t)\rangle$ after some time t is in the most general form given as

$$|\psi(t)\rangle = \sum_{i,j\geq 0} c_{i,j}(t)\,|i,j\rangle \tag{A.4}$$

where the coefficients $c_{i,j}(t)$ are given by first order perturbation theory as

$$c_{i,j}(t) = c_{i,j}(t=0) - \frac{i}{\hbar}\int_0^t \mathrm{d}t'\,\langle ij|\,\hat{H}_G\,|kl\rangle\,e^{-i(E_{kl}-E_{ij})t'/\hbar}. \tag{A.5}$$

The exponent is given by the energy of the appropriate Fock states $E_{kl} - E_{ij} = \hbar\omega(k + l - (i + j))$ and the matrix element in the integrand can be calculated to

$$\langle ij|\,\hat{H}_G\,|kl\rangle = \begin{cases} -\hbar g & \text{if } i = k \pm 1 \text{ and } j = l \mp 1 \\ 0 & \text{otherwise} \end{cases}. \tag{A.6}$$

The coefficients for $t = 0$ are trivially given from the initial state as

$$c_{i,j}(t = 0) = \begin{cases} 1 & \text{for } i,j = k,l \\ 0 & \text{otherwise} \end{cases}. \tag{A.7}$$

For the non-zero states the energies in the exponent equate to zero and the evolved state is given by (up to a normalization)

$$|\psi(t)\rangle = |kl\rangle - igt\,|k-1,l+1\rangle - igt\,|k+1,l-1\rangle + \mathcal{O}(g^2). \tag{A.8}$$

For $k = 1$ and $l = 0$, the evolved state is in the form (with normalization $\mathcal{N}$)

$$|\psi(t)\rangle = \mathcal{N}\left(|10\rangle - igt\,\big|01 + \mathcal{O}(g^2)\big\rangle\right) \tag{A.9}$$

which is entangled with logarithmic negativity $E_N(|\psi(t)\rangle\langle\psi(t)|) \simeq 2tg/\log 2 + \mathcal{O}(g^2) \geq 0$.

A.2 Exemplary calculation of E_N

In this section, the logarithmic negativity E_N eq. (2.15) is exemplary calculated for the state eq. (2.7). The density matrix of this system is given by

$$\rho(t) = |\psi(t)\rangle\langle\psi(t)| = \frac{1}{4}\begin{pmatrix} 1 & e^{i\Delta\phi} & e^{i\Delta\phi} & 1 \\ e^{-i\Delta\phi} & 1 & 1 & e^{-i\Delta\phi} \\ e^{-i\Delta\phi} & 1 & 1 & e^{-i\Delta\phi} \\ 1 & e^{i\Delta\phi} & e^{i\Delta\phi} & 1 \end{pmatrix}. \tag{A.10}$$

Consequently, the partially transposed density ρ^{Γ_B} is given by

$$\rho^{\Gamma_B}(t) = \frac{1}{4}\begin{pmatrix} 1 & e^{-i\Delta\phi} & e^{i\Delta\phi} & 1 \\ e^{i\Delta\phi} & 1 & 1 & e^{-i\Delta\phi} \\ e^{-i\Delta\phi} & 1 & 1 & e^{i\Delta\phi} \\ 1 & e^{i\Delta\phi} & e^{-i\Delta\phi} & 1 \end{pmatrix}. \tag{A.11}$$

The eigenvalues where calculated using `Mathematica` and equate to

$$\left\{ \sin^2\left(\frac{\Delta\phi}{2}\right), \cos^2\left(\frac{\Delta\phi}{2}\right), \frac{\sin\Delta\phi}{2}, -\frac{\sin\Delta\phi}{2} \right\}$$

According to lemma 2.1, $\left\|\rho^{\Gamma_B}\right\|_1$ is given by the sum of the absolute eigenvalues, which is equal to $1 + |\sin\Delta\phi|$. The negativity as the absolute sum of all negative eigenvalues (demonstrated in proposition 2.2) equates to $\mathcal{N} = |\sin\Delta\phi|\,/2$. Both methods result in a logarithmic negativity of $E_N = \log_2(1 + |\sin\Delta\phi|)$.

A.3 Polarizability of a dielectric sphere

The polarizability α is defined via

$$\mathbf{E}_\infty \alpha = \mathbf{p}, \tag{A.12}$$

where $\mathbf{p}$ is the induced dipole moment and $\mathbf{E}_\infty$ is the external electric field that induces the dipole moment. For a linear and uniform dielectric, it is given as $\mathbf{p} = \mathcal{V}\varepsilon_0(\varepsilon_r - 1)\mathbf{E}_{\text{in}}$ [74, p. 220-226]. Here, $\mathcal{V}$ is the volume of the object and $\mathbf{E}_{\text{in}}$ is the electric field inside the dielectric. The electrostatic boundary conditions for the problem are given by

$$V_{\text{in}}\Big|_{r=R} = V_{\text{out}}\Big|_{r=R} \quad \text{and} \quad \varepsilon_r \varepsilon_0 \frac{\partial V_{\text{in}}}{\partial r}\bigg|_{r=R} = \varepsilon_0 \frac{\partial V_{\text{out}}}{\partial r}\bigg|_{r=R} \tag{A.13}$$

and the electric potential outside of the sphere at $r \to \infty$ should be equal to the external dipole-inducing field $V_{\text{out}}|_{r \to \infty} = -\mathbf{E}_\infty \cdot \mathbf{r} = -E_\infty r \cos\theta$. The electric potential inside and outside the sphere can be calculated using the spherical decomposition of the general electric potential $V \propto 1/|\mathbf{r} - \mathbf{r}'|$ into Legendre Polynomials P_l [74, p. 188-190]:

$$V_{\text{in}}(r, \theta) = -E_\infty r \cos\theta + \sum_{l=0}^{\infty} A_l r^l P_l(\cos\theta), \tag{A.14}$$

$$V_{\text{out}}(r, \theta) = -E_\infty r \cos\theta + \sum_{l=0}^{\infty} \frac{B_l}{r^{l+1}} P_l(\cos\theta). \tag{A.15}$$

Applying both boundary conditions, it follows that [74, p. 249-251]

$$\begin{cases} A_l = B_l = 0 & \text{for } l \neq 1, \\ A_1 = -\frac{3}{\varepsilon_r + 2} E_\infty, \quad B_1 = \frac{\varepsilon_r - 1}{\varepsilon_r + 2} R^3 E_\infty \end{cases} \tag{A.16}$$

and the resulting homogenous electric field $\mathbf{E}_{\text{in}} = -\nabla V_{\text{in}}$ inside the sphere is given as

$$\mathbf{E}_{\text{in}} = \frac{3}{\varepsilon_r + 2} \mathbf{E}_\infty. \tag{A.17}$$

The field is shown on the right in **??**.The polarizability α of the sphere can be now be determined to

$$\alpha_{\text{sphere}} = 4\pi\varepsilon_0 R^3 \left(\frac{\varepsilon_r - 1}{\varepsilon_r + 2} \right). \tag{A.18}$$

Depending on the definition, sometimes the factor $4\pi\varepsilon_r$ is dropped.

A.4 Blocking of the shield

Assume two spheres A and B with charge q_A and q_B separated by a distance $2L$ on the x-axis. A circular shield is placed perfectly in the center of the spheres orthogonal to
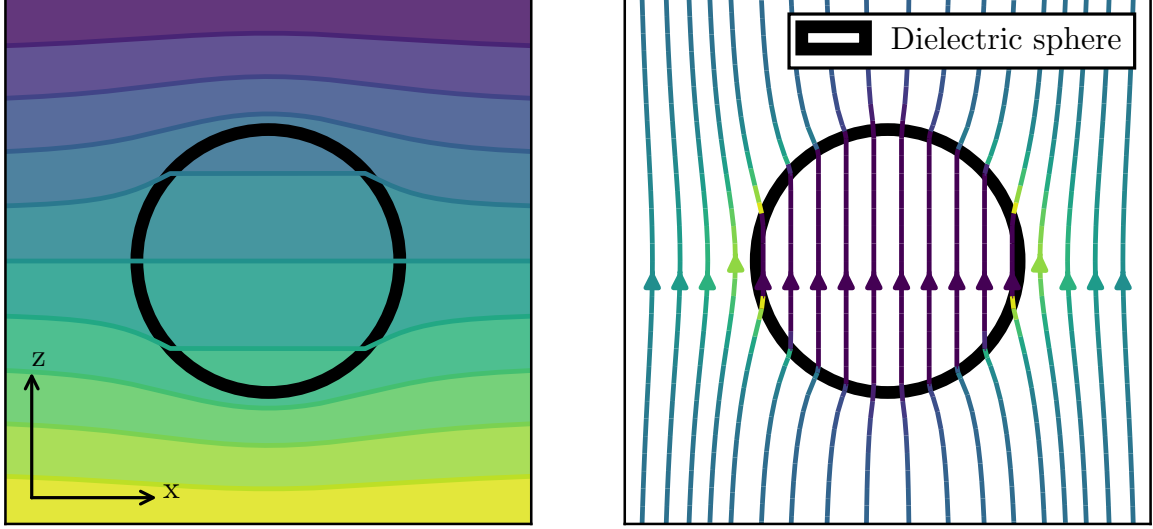
Figure A.1: left: Electric potential V of a dielectric sphere in a external electric field $\mathbf{E}_\infty \parallel \mathbf{e_z}$. **right:** The corresponding electric field lines inside and outside the dielectric sphere.

the direct connection between them. The magnitude of the field at a distance z in the direction $\mathbf{e}_x$ from this connection line is given by

$$E_x(z) = \frac{L(q_A - q_B)}{4\pi\varepsilon_0(L^2 + z^2)^{3/2}} \tag{A.19}$$

The total flux the circular shield with radius r_s is given by

$$\Phi = \int_0^{r_s} \mathrm{d}z \int_0^{2\pi} z\mathrm{d}\varphi\, E_x(z) = \frac{(q_A - q_B)}{2\varepsilon_0}\left[1 - \frac{L}{\sqrt{L^2 + r_s^2}}\right]. \tag{A.20}$$

Comparing the total flux for $r_s \to \infty$ with the flux through the shield, one can arrive at the charge-independent **_effectiveness_** η of the shield as

$$\eta = \frac{\Phi}{\Phi_\infty} = 1 - \frac{L}{\sqrt{L^2 + r_s^2}} \tag{A.21}$$

and thus a shield with radius

$$r_s = L\sqrt{\frac{1 - (1 - \eta)^2}{(1 - \eta)^2}} \tag{A.22}$$

will block a fraction η of the total field.

A.5 Thermal harmonic oscillator

The amplitude z of a single vibrational shield-mode (k, l) with frequency $\omega_{kl} \equiv \omega$ behaves like a quantum harmonic oscillator. The average amplitude $\langle z \rangle_n = 0$. The variance $(\Delta z)^2 = \langle z^2 \rangle - \langle z \rangle^2$ however is given by

$$(\Delta z)_n^2 = \left\langle z^2 \right\rangle_n = \frac{\hbar}{2m\omega}(1 + 2n). \tag{A.23}$$

At a temperature T, the occupation of the modes is described by the boltzmann distribution:

$$\left\langle z^2 \right\rangle_T = \sum_{n=0}^{\infty} \frac{1}{Z} e^{-\beta E_n} \left\langle z^2 \right\rangle_n, \tag{A.24}$$

where $\beta = 1/k_B T$, $E_n = \hbar\omega(n + 1/2)$ is the energy of mode n and

$$Z = \sum_{n=0}^{\infty} e^{-\beta E_n} = \frac{e^{-\beta \frac{\hbar\omega}{2}}}{1 - e^{-\beta\hbar\omega}} \tag{A.25}$$

is the partition function. Using known series, the expression eq. (A.24) can be evaluated to

$$(\Delta z)_T^2 = \left\langle z^2 \right\rangle_T = \frac{\hbar}{2m\omega} \sum_{n=0}^{\infty} \frac{1}{Z} \left[e^{-\beta E_n} + 2n e^{-\beta E_n} \right] \tag{A.26}$$

$$= \frac{\hbar}{2m\omega} \left[1 + \frac{2}{Z} \sum_{n=0}^{\infty} n e^{-\beta E_n} \right] \tag{A.27}$$

$$= \frac{\hbar}{2m\omega} \left[1 + \frac{2e^{-\beta\hbar\omega}}{1 - e^{-\beta\hbar\omega}} \right] = \frac{\hbar}{2m\omega} \coth\left(\frac{\hbar\omega}{2k_B T} \right) \tag{A.28}$$

B Primary calculations

B.1 Entanglement in different orientations

Expanding the separations $1/L^{(ij)}$ between the states $\left|\psi_A^{(i)}\right\rangle$ and $\left|\psi_B^{(j)}\right\rangle$ in second order in Δx and calculating the dynamic phases, the following represents the time-evolved state:

$$
\rho_{\text{Phase}} = \frac{1}{4}
\begin{pmatrix}
1 & e^{i(\phi_B + \phi_{AB})} & e^{-i(\phi_A - \phi_{AB})} & e^{-i(\phi_A - \phi_B)} \\
 & 1 & e^{-i(\phi_A + \phi_B)} & e^{-i(\phi_A + \phi_{AB})} \\
 & & 1 & e^{i(\phi_B - \phi_{AB})} \\
 & & & 1
\end{pmatrix}
\tag{B.1}
$$

with the substitutions

$$
\phi_A = g_{\text{Grav}} \frac{\Delta x_A \sin \alpha}{4L^2}, \quad \phi_B = g_{\text{Grav}} \frac{\Delta x_B \sin \beta}{4L^2},
\tag{B.2}
$$

$$
\phi_{AB} = g_{\text{Grav}} \frac{\Delta x_A \Delta x_B}{8L^3} \left(\frac{1}{2} \cos \alpha \cos \beta - \sin \alpha \sin \beta \right)
\tag{B.3}
$$

and the gravitational coupling strength

$$
g_{\text{Grav}} = \frac{G M_A M_B t}{\hbar}.
\tag{B.4}
$$

Eigenvalues of ρ^Γ are

$$
\left\{ \sin^2 \left(\frac{\phi_{AB}}{2} \right), \cos^2 \left(\frac{\phi_{AB}}{2} \right), \frac{\sin(\phi_{AB})}{2}, -\frac{\sin(\phi_{AB})}{2} \right\}
\tag{B.5}
$$

and thus the logarithmic negativity is given by the sum of negative eigenvalues as

$$
E_N = \log_2 \left\{ 1 + \left| \sin \left(\frac{G M_A M_B \Delta x_A \Delta x_B t}{8 \hbar L^3} \left[\sin \alpha \sin \beta - \frac{1}{2} \cos \alpha \cos \beta \right] \right) \right| \right\}.
\tag{B.6}
$$

Due to Casimir interactions between the particles and the shield, in first order only the additional term $(\delta = \alpha, \beta)$

$$
\phi_{\text{Cas., A(B)}} = \frac{c \pi^3}{720} \left(\frac{\varepsilon_r - 1}{\varepsilon_r + 1} \right) \varphi(\varepsilon_r) R \frac{2 \Delta x_{A(B)} \sin \delta}{(L - R - d/2)^3} t
\tag{B.7}
$$

is added to the phase $\phi_{A(B)}$, leaving the resulting logarithmic negativity unchanged.

B.2 Density matrix with stochastic placement variations

Expanding the separations $1/(\mathscr{L}_{A(B)}^{(i)})^2$ for the PFA from eq. (4.7) in first order in $\theta_{A(B)}$ and $L_{A(B)}$ (here exemplary for mass $A^{(1)}$):

$$\frac{1}{\left(\mathscr{L}_A^{(1)}\right)^2} \approx \frac{4}{(d-2L+2R)^2} + \frac{8\Delta x_{A(B)}\sin\delta}{(d-2L+2R)^3} + \theta_{A(B)}\left(\frac{8\Delta x_{A(B)}\cos\delta}{(d-2L+2R)^3}\right)$$

$$+ L_{A(B)}\left(\frac{16}{(d-2L+2R)^3} + \frac{48\Delta x_{A(B)}\sin\delta}{(d-2L+2R)^4}\right) + \theta_{A(B)}L_{A(B)}\frac{48\Delta x_{A(B)}\cos\delta}{(d-2L+2R)^4} \quad \text{(B.8)}$$

Similar results can be obtained for expanding the gravitational couplings $1/L^{(ij)}$ from eq. (4.10):

$$\frac{1}{L^{(11)}} \approx \frac{1}{2L} + \frac{\Delta x_B\sin\beta - \Delta x_A\sin\alpha}{8L^2} - \theta_A\frac{\Delta x_A\cos\alpha}{8L^2} + \theta_B\frac{\Delta x_B\cos\beta}{8L^2}$$

$$+ L_A\left(-\frac{1}{4L^2} + \frac{\Delta x_A\sin\alpha - \Delta x_B\sin\beta}{8L^3}\right) + L_B\left(-\frac{1}{4L^2} + \frac{\Delta x_A\sin\alpha - \Delta x_B\sin\beta}{8L^3}\right)$$

$$+ L_A\theta_A\frac{\Delta x_A\cos\alpha}{8L^3} - L_A\theta_B\frac{\Delta x_B\cos\beta}{8L^3} + L_B\theta_A\frac{\Delta x_A\cos\alpha}{8L^3} - L_B\theta_B\frac{\Delta x_B\cos\beta}{8L^3}$$

$$+ L_A L_B\left(\frac{2}{4L^3} + \frac{3\Delta x_B\sin\beta - 3\Delta x_A\sin\alpha}{16L^4}\right)$$

$$- L_A L_B\theta_A\frac{3\Delta x_A\cos\alpha}{16L^4} + L_A L_B\theta_B\frac{3\Delta x_B\cos\beta}{16L^4} \quad \text{(B.9)}$$

The resulting average over $\theta_{A(B)}$ and $L_{A(B)}$ can be computed by

$$\int_{-\infty}^{\infty} \mathrm{d}\theta_A \mathrm{d}\theta_B \mathrm{d}L_A \mathrm{d}L_B\, p(\theta_A)p(\theta_B)p(L_A)p(L_B)e^{i\phi} \quad \text{(B.10)}$$

where $p(\,\cdot\,)$ is a gaussian probability distribution in the form of

$$p(x) = \frac{1}{\sqrt{2\pi}\Delta x}e^{-\frac{x^2}{2(\Delta x)^2}} \quad \text{(B.11)}$$

and ϕ is the accumulated dynamic phase dependent on the two series expansions above. The mixed terms consisting of combinations of θ and L can be neglected in first order because in the final result, they appear in the form of (notation: $\Delta A, \Delta B$ for either $\Delta\theta$ or ΔL; a, b are constants)

$$\sim \exp\left\{-\frac{a^2(\Delta A)^2}{2b^2(\Delta A)^2(\Delta B)^2 + 2}\right\} \xrightarrow{\Delta A, \Delta B \ll 1} 1. \quad \text{(B.12)}$$

Each averaged element of the density matrix can therefore be analytically calculated using

$$\prod_{\Delta A=\{\Delta\theta_{A(B)}, \Delta L_{A(B)}\}} \int_{-\infty}^{\infty} \mathrm{d}A\, \frac{1}{\sqrt{2\pi}\Delta A}e^{-\frac{A^2}{2(\Delta A)^2}}e^{i\xi A}e^{i\phi} = \prod_{\Delta A} e^{-\frac{\xi^2(\Delta A)^2}{2}}e^{i\phi}. \quad \text{(B.13)}$$

The resulting averaged density matrices are given by the following for variations in the angle:

$$
\langle \rho_\theta \rangle = \frac{1}{4}
\begin{pmatrix}
1 & e^{-\xi_B^2 \frac{(\Delta\theta_B)^2}{2}t^2} & e^{-\xi_A^2 \frac{(\Delta\theta_A)^2}{2}t^2} & e^{-\xi_A^2 \frac{(\Delta\theta_A)^2}{2}t^2} e^{-\xi_B^2 \frac{(\Delta\theta_B)^2}{2}t^2} \\
 & 1 & e^{-\xi_A^2 \frac{(\Delta\theta_A)^2}{2}t^2} e^{-\xi_B^2 \frac{(\Delta\theta_B)^2}{2}t^2} & e^{-\xi_A^2 \frac{(\Delta\theta_A)^2}{2}t^2} \\
 & & 1 & e^{-\xi_B^2 \frac{(\Delta\theta_B)^2}{2}t^2} \\
 & & & 1
\end{pmatrix}
\tag{B.14}
$$

with the abbreviations $(\delta = \alpha, \beta)$

$$
\xi_{A(B)} = \left(\frac{c\pi^3}{720} \left(\frac{\varepsilon_r - 1}{\varepsilon_r + 1} \right) \varphi(\varepsilon_r) R \frac{2\Delta x_{A(B)} \cos\delta}{(L - R - d/2)^3} + \frac{GM_A M_B}{\hbar} \frac{\Delta x_{A(B)} \cos\delta}{4L^2} \right)
\tag{B.15}
$$

Similar results for variations in the particle-shield separation L can be obtained:

$$
\langle \rho_L \rangle = \frac{1}{4}
\begin{pmatrix}
1 & e^{-\chi_B^2 \frac{(\Delta L_A)^2}{2}t^2} e^{-(\zeta_B+\chi_B)^2 \frac{(\Delta L_B)^2}{2}t^2} & e^{-(\zeta_A+\chi_A)^2 \frac{(\Delta L_A)^2}{2}t^2} e^{-\chi_A^2 \frac{(\Delta L_B)^2}{2}t^2} & \cdots \\
 & 1 & e^{-(\chi_A+\zeta_A)^2 \frac{(\Delta L_A)^2}{2}t^2} e^{-(\chi_B+\zeta_B)^2 \frac{(\Delta L_B)^2}{2}t^2} & \cdots \\
 & & 1 & \cdots \\
 & & & \cdots
\end{pmatrix}
$$

$$
\begin{pmatrix}
\cdots & e^{-(\chi_A+\zeta_A)^2 \frac{(\Delta L_A)^2}{2}t^2} e^{-(\chi_B+\zeta_B)^2 \frac{(\Delta L_B)^2}{2}t^2} \\
\cdots & e^{-(\zeta_A+\chi_A)^2 \frac{(\Delta L_A)^2}{2}t^2} e^{-\chi_A^2 \frac{(\Delta L_B)^2}{2}t^2} \\
\cdots & e^{-\chi_B^2 \frac{(\Delta L_A)^2}{2}t^2} e^{-(\zeta_B+\chi_B)^2 \frac{(\Delta L_B)^2}{2}t^2} \\
\cdots & 1
\end{pmatrix}
\tag{B.16}
$$

with

$$
\chi_{A(B)} = \frac{GM_A M_B}{\hbar} \frac{\Delta x_{A(B)} \sin\delta}{4L^3}
\tag{B.17}
$$

$$
\zeta_{A(B)} = \frac{c\pi^3}{720} \left(\frac{\varepsilon_r - 1}{\varepsilon_r + 1} \right) \varphi(\varepsilon_r) R \frac{6\Delta x_{A(B)} \sin\delta}{(L - R - d/s)^4}
\tag{B.18}
$$

The combined mean density matrix is therefore given by

$$
\langle \rho \rangle = \rho_{\text{Phase}} \odot \langle \rho_\theta \rangle \odot \langle \rho_L \rangle
\tag{B.19}
$$

where the symbol $\odot$ represents the element-wise matrix product (Hadamard product). In the special case where $\Delta\theta_A = \Delta\theta_B$ and $\Delta L_A = \Delta L_B$ as well as where both particles are identical, i.e. $\Delta x_A = \Delta x_B$ and $M_A = M_B$ and $\alpha = \pm\beta$, the logarithmic negativity can be obtained analytically. Using the approximation $\chi_{A(B)} \ll \zeta_{A(B)}$, which is justified for all separations $R < L \lesssim 40\,\text{m}$.

$$
\langle \rho \rangle = \rho_{\text{Phases}} \odot \frac{1}{4}
\begin{pmatrix}
1 & e^{-\gamma} & e^{-\gamma} & e^{-2\gamma} \\
 & 1 & e^{-2\gamma} & e^{-\gamma} \\
 & & 1 & e^{-\gamma} \\
 & & & 1
\end{pmatrix}
\tag{B.20}
$$

with

$$\gamma = \left(\xi^2 \frac{(\Delta\theta)^2}{2} + \zeta^2 \frac{(\Delta L)^2}{2} \right) t^2 \tag{B.21}$$

The logarithmic negativity is given by (ϕ_{AB} from eq. (B.3))

$$E_N = \max\left\{ 0, \ \log_2\left(e^{-\gamma} \left(\cosh\gamma + |\sin\phi_{AB}| \right) \right) \right\} \tag{B.22}$$

$$= \log_2\left\{ \frac{1}{2} e^{-\gamma} \left(|\sin\phi_{AB} - \sinh\gamma| + |\sin\phi_{AB} + \sinh\gamma| + 2\cosh\gamma \right) \right\}. \tag{B.23}$$

For general combinations of $\Delta L_A, \Delta L_B, \Delta\theta_A, \Delta\theta_B$ and for results without any approximations, the logarithmic negativity was computed numerically.

B.3 Density matrix for particles in front a vibrating plate

The separations between the shield and the Particle state $A(B)_i$ in the parallel configuration are given by

$$d_{A(B)}^i = L \pm_{A(B)} z \left(|u| \mp_i |\nabla u| \frac{\Delta x}{2} \right) \tag{B.24}$$

where the first $\pm$ distinguishes between particle A and B and the second one between $i = 1$ and $i = 2$. The gravitational interaction is given as before in chapter 2. After averaging over z (normally distributed around $\langle z \rangle = 0$ and std. Δz) the resulting density matrix is now given by

$$\langle \rho \rangle = \frac{1}{4} \begin{pmatrix} 1 & e^{i\Delta\phi} e^{-\frac{1}{2}(\xi_{\mathrm{Cas}})^2(\Delta z)^2} & e^{i\Delta\phi} e^{-\frac{1}{2}(\xi_{\mathrm{Cas}})^2(\Delta z)^2} & 1 \\ & 1 & e^{-\frac{1}{2}(2\xi_{\mathrm{Cas}})^2(\Delta z)^2} & e^{-i\Delta\phi} e^{-\frac{1}{2}(\xi_{\mathrm{Cas}})^2(\Delta z)^2} \\ & & 1 & e^{-i\Delta\phi} e^{-\frac{1}{2}(\xi_{\mathrm{Cas}})^2(\Delta z)^2} \\ & & & 1 \end{pmatrix} \tag{B.25}$$

with

$$\Delta\phi = \frac{GM_A M_B}{\hbar} \left(\frac{1}{4L^2} - \frac{1}{\sqrt{2L + (\Delta x)^2}} \right) t \tag{B.26}$$

$$\xi_{\mathrm{Cas}} = \frac{c\pi^3 R}{720} \left(\frac{\varepsilon_r - 1}{\varepsilon_r + 1} \right) \varphi(\varepsilon_r) \cdot \frac{2|\nabla u| \Delta x}{\mathscr{L}^3} t \tag{B.27}$$

which is only dependent on the gradient of the shape $|\nabla u|$. The logarithmic negativity is given by

$$E_N(\langle \rho \rangle) = \log_2\left\{ \frac{1}{4} \left(3 + e^{-4\gamma} + \sqrt{(1 - e^{-4\gamma})^2 + 16e^{-2\gamma}\sin^2\Delta\phi} \right) \right\} \tag{B.28}$$

where

$$\gamma = \frac{1}{2}(\xi_{\mathrm{Cas}})^2(\Delta z)^2. \tag{B.29}$$

B.4 Time evolution of two particles in front of a thermal plate

The time evolution operator $\hat{U} = e^{-i\hat{H}t/\hbar}$ of the hamiltonian eq. (5.30) can be calculated in the interaction picture using the "Magnus expansion" [75]. In the following calculations, the direct gravitational interactions between the two particles are ignored as they don't depend on the shield vibrations at all. The final evolution due to these couplings were already studied in chapter 4 and can just be added in the end. The interaction picture hamiltonian in the $\{|\psi_A^1\psi_B^1\rangle, |\psi_A^1\psi_B^2\rangle, |\psi_A^2\psi_B^1\rangle, |\psi_A^2\psi_B^2\rangle\}$-basis is given by

$$\hat{H}_{\text{int}} = \sum_{m \in \{(k,l)\}} \begin{pmatrix} g_{A,m}^1 + g_{B,m}^1 & & & \\ & g_{A,m}^1 + g_{B,m}^2 & & \\ & & g_{A,m}^2 + g_{B,m}^1 & \\ & & & g_{A,m}^2 + g_{B,m}^2 \end{pmatrix} (\hat{a}e^{-i\omega_m t} + \hat{a}^\dagger e^{i\omega_m t}) \tag{B.30}$$

The operator at the beginning is referred to as $\hat{G}$ in the following. The time evolution in the Magnus expansion here given by [75]

$$\hat{U}(t) = \exp\left\{ -\frac{i}{\hbar} \int_0^t dt_1 \hat{H}_{\text{int}}(t) - \frac{1}{2\hbar^2} \int_0^t dt_1 \int_0^{t_1} dt_2 [\hat{H}_{\text{int}}(t_1), \hat{H}_{\text{int}}(t_2)] \right\}. \tag{B.31}$$

All higher order terms vanish, so this is an exact result. After substitution, the result is given by

$$\hat{U}(t) = \exp\left\{ \hat{G}(f_1 \hat{a}^\dagger - f_1^* \hat{a}) + i\hat{G}^2 f_2 \right\} \tag{B.32}$$

$$= \hat{D}\left(f_1(g_{A,m}^1 + g_{B,m}^1) \right) \exp\left\{ i f_2 (g_{A,m}^1 + g_{B,m}^1)^2 \right\} \left| \psi_A^1 \psi_B^1 \right\rangle\!\!\left\langle \psi_A^1 \psi_B^1 \right| + \ldots \tag{B.33}$$

with

$$f_1 = \frac{(1 - e^{i\omega_m t})}{\hbar \omega_m} \quad \text{and} \quad f_2 = \frac{t\omega_m - \sin(t\omega_m)}{\hbar^2 \omega_m^2} \tag{B.34}$$

and the displacement operator $\hat{D}(\alpha) = \exp\left\{ \alpha \hat{a}^\dagger - \alpha^* \hat{a} \right\}$. The evolved state $\rho(t) = \hat{U}(t)\rho_0 \hat{U}^\dagger(t)$ is now given by

$$\rho(t) = \bigotimes_{m \in \{(k,l)\}} \hat{D}\left(f_1(g_A^1 + g_B^1) \right) \rho_{\text{th,m}} \hat{D}^\dagger \left(f_1(g_A^1 + g_B^1) \right) \otimes \frac{1}{4} \left| \psi_A^1 \psi_B^1 \right\rangle\!\!\left\langle \psi_A^1 \psi_B^1 \right|$$

$$+ \hat{D}\left(f_1(g_A^1 + g_B^1) \right) \rho_{\text{th,m}} \hat{D}^\dagger \left(f_1(g_A^1 + g_B^2) \right) \otimes \frac{1}{4} e^{if_2(g_A^1 + g_B^1)^2} \left| \psi_A^1 \psi_B^1 \right\rangle\!\!\left\langle \psi_A^1 \psi_B^2 \right| e^{-if_2(g_A^1 + g_B^2)^2}$$

$$+ \ldots$$

$$+ \hat{D}\left(f_1(g_A^2 + g_B^2) \right) \rho_{\text{th,m}} \hat{D}^\dagger \left(f_1(g_A^2 + g_B^1) \right) \otimes \frac{1}{4} e^{if_2(g_A^2 + g_B^2)^2} \left| \psi_A^2 \psi_B^2 \right\rangle\!\!\left\langle \psi_A^2 \psi_B^1 \right| e^{-if_2(g_A^2 + g_B^1)^2}$$

$$+ \hat{D}\left(f_1(g_A^2 + g_B^2) \right) \rho_{\text{th,m}} \hat{D}^\dagger \left(f_1(g_A^2 + g_B^2) \right) \otimes \frac{1}{4} \left| \psi_A^2 \psi_B^2 \right\rangle\!\!\left\langle \psi_A^2 \psi_B^2 \right| \tag{B.35}$$

B Primary calculations

We are interested in the evolution of the two-particle system. This is given by tracing out the thermal shield $\rho_{\text{sys.}} = \text{tr}_{th}\{\rho(t)\}$. Using $\text{tr}\{A \otimes B\} = \text{tr}\{A\}\,\text{tr}\{B\}$, it follows:

$$\rho_{\text{sys.}} = \frac{1}{4}\begin{pmatrix} 1 & \prod_m \text{tr}\left\{\hat{D}\left(f_1(g_A^1 + g_B^1)\right)\rho_{\text{th,m}}\hat{D}^\dagger\left(f_1(g_A^1 + g_B^2)\right)\right\}e^{if_2((g_A^1+g_B^1)^2-(g_A^1+g_B^2)^2)} & \cdots \\ \vdots & \ddots & \\ & & \end{pmatrix}$$

$$\tag{B.36}$$

To calculate $\text{tr}\left\{\hat{D}(\zeta_i)\rho_{\text{th}}\hat{D}^\dagger(\zeta_j)\right\}$, we expand ρ_{th} into coherent states [64]

$$\rho_{\text{th}} = \int \mathrm{d}\alpha^2\, \frac{1}{\bar{n}\pi}e^{-\frac{|\alpha|^2}{\bar{n}}}|\alpha\rangle\langle\alpha| \tag{B.37}$$

and calculate the required trace [64]:

$$\text{tr}\left\{\hat{D}(\zeta_i)\rho_{\text{th}}\hat{D}^\dagger(\zeta_j)\right\} = \exp\left\{\phi - |\Delta\zeta|^2\left(\frac{1}{2}+\bar{n}\right)\right\} \tag{B.38}$$

where $\Delta\zeta = \zeta_i - \zeta_j$ and $\phi = (\zeta_j^*\zeta_i - \zeta_j\zeta_i^*)/2 = 0$. The final decoherence elements of the evolved state therefore all have the form

$$e^{-\gamma_{1,2}} = \exp\left\{-\sum_m \left|(g_{A,m}^1 + g_{B,m}^1) - (g_{A,m}^1 + g_{B,m}^2)\right|^2 f_1 f_1^*(\frac{1}{2}+\bar{n}_m)\right\} \tag{B.39}$$

C Additional figures

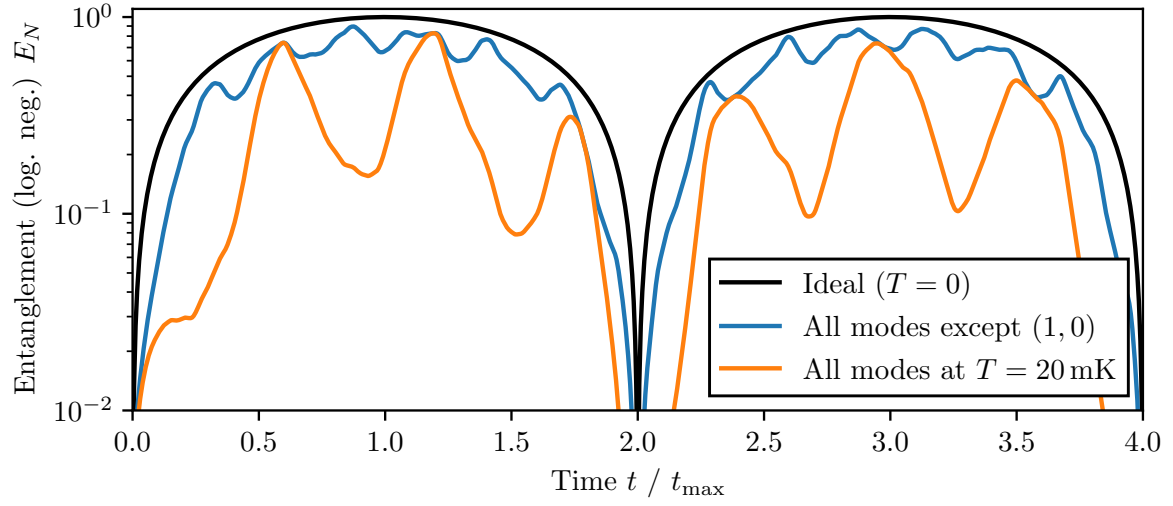**Figure C.1:** Similar to fig. 5.7 at $T = 20\,\mathrm{mK}$ for a slightly smaller shied with $r_s = 5\,\mathrm{mm}$.